



UNIVERSIDADE ESTADUAL DE CAMPINAS
Faculdade de Engenharia Mecânica

Andrés Felipe Galvis Rodríguez

***Multiscale Modeling of Dynamic Failure
in 3D Polycrystalline Materials
using BEM and MD***

***Modelagem Multiescala de Falha Dinâmica
em Materiais Policristalinos 3D
usando BEM e MD***

CAMPINAS
2019

Andrés Felipe Galvis Rodríguez

***Multiscale Modeling of Dynamic Failure
in 3D Polycrystalline Materials
using BEM and MD***

***Modelagem Multiescala de Falha Dinâmica
em Materiais Policristalinos 3D
usando BEM e MD***

Thesis presented to the School of Mechanical Engineering of the University of Campinas in partial fulfillment of the requirements for the degree of Doctor in Mechanical Engineering, in the area of Solid Mechanics and Design.

Tese apresentada à Faculdade de Engenharia Mecânica da Universidade Estadual de Campinas como parte dos requisitos exigidos para a obtenção do título de Doutor em Engenharia Mecânica na área de Mecânica dos Sólidos e Projeto Mecânico

Orientador: Prof. Dr. Paulo Sollero

ESTE EXEMPLAR CORRESPONDE À VERSÃO
FINAL DA TESE DEFENDIDA PELO ALUNO
ANDRÉS FELIPE GALVIS RODRÍGUEZ, E ORI-
ENTADO PELO PROF. DR. PAULO SOLLERO.

.....
ASSINATURA DO ORIENTADOR

CAMPINAS
2019

Agência(s) de fomento e nº(s) de processo(s): CNPq, 154283/2014-2

ORCID: <https://orcid.org/0000-0002-2833-2328>

Ficha catalográfica
Universidade Estadual de Campinas
Biblioteca da Área de Engenharia e Arquitetura
Rose Meire da Silva - CRB 8/5974

G139m Galvis Rodríguez, Andrés Felipe, 1989-
Multiscale Modeling of Dynamic Failure in 3D Polycrystalline Materials
using BEM and MD / Andrés Felipe Galvis Rodríguez. – Campinas, SP:
[s.n.], 2019.

Orientador: Paulo Sollero.
Tese (doutorado) - Universidade Estadual de Campinas, Faculdade de
Engenharia Mecânica.

1. Multiescala. 2. Método de elementos de contorno. 3. Dinâmica molecular.
I. Sollero, Paulo, 1950-. II. Universidade Estadual de Campinas.
Faculdade de Engenharia Mecânica. III. Título.

Informações para Biblioteca Digital

Título em outro idioma: Modelagem multiescala de falha dinâmica em materiais policristalinos
3D usando BEM e MD

Palavras-chave em Inglês:

Multiscale

Boundary element method

Molecular dynamics

Área de concentração: Mecânica dos Sólidos e Projeto Mecânico

Titulação: Doutor em Engenharia Mecânica

Banca Examinadora:

Paulo Sollero [Orientador]

Luiz Carlos Wrobel

Euclides de Mesquita Neto

Ney Augusto Dumont

Renato Pavanello

Data da defesa: 25-01-2019

Programa de Pós Graduação: Engenharia Mecânica

UNIVERSIDADE ESTADUAL DE CAMPINAS
FACULDADE DE ENGENHARIA MECÂNICA
COMISSÃO DE PÓS-GRADUAÇÃO EM ENGENHARIA MECÂNICA
DEPARTAMENTO DE MECÂNICA COMPUTACIONAL

TESE DE DOUTORADO ACADÊMICO

*Multiscale Modeling of Dynamic Failure in
3D Polycrystalline Materials using BEM and MD*

*Modelagem Multiescala de Falha Dinâmica em
Materiais Policristalinos 3D usando BEM e MD*

Autor: Andrés Felipe Galvis Rodríguez

Orientador: Prof. Dr. Paulo Sollero

A Banca Examinadora composta pelos membros abaixo aprovou esta Tese:

Prof. Dr. Paulo Sollero, Presidente
DMC/FEM/UNICAMP

Prof. Dr. Luiz Carlos Wrobel
ED&PS/Brunel University London

Prof. Dr. Euclides de Mesquita Neto
DMC/FEM/UNICAMP

Prof. Dr. Ney Augusto Dumont
CIV/PUC - Rio de Janeiro

Prof. Dr. Renato Pavanello
DMC/FEM/UNICAMP

A Ata da defesa com as respectivas assinaturas dos membros encontra-se no processo de vida acadêmica do aluno.

Campinas, 25 de Janeiro de 2019.

*I dedicate this thesis to my parents Ruby and Julio Cesar,
also to my sister Maria Alejandra.*

*Dedico esta tesis a mis padres Ruby y Julio Cesar,
también a mi hermana Maria Alejandra.*

Acknowledgements

To my family for their love and affection, my mother Ruby, my father Julio, my sister Maria Alejandra.

To my PhD advisor: Professor Paulo Sollero for his unwavering support and friendship throughout this work.

To Professor Luiz Carlos Wrobel for all discussions, friendship and dedication in my period abroad.

To Prof. Vitor Coluci, Prof. Giulio Alfano and Professor Hamid Assabi for all discussions, collaboration and useful advice.

I would like to thank to René Quispe for his experienced advices during the first year of this project.

I would like to thank to Pedro Santos for his collaboration during the last year of this project.

To my old friend Andres Ramirez (el químico).

To my Lab friends Lucas, Daniel, Juan Esteban, Bruno and Ana.

I also thank to Edguitar, Carlos(el ebanista), Juan(ruim), Jhon(pams), Harold(tony) and Felipe(pitla).

To my friends in Barão Geraldo Jhon Jairo(popeye), Bruno, Cesar, Raimundo and Sergio.

To University of Campinas for the opportunity to carry out this work.

To Brunel University London for providing the academic environment and support during the last semester of the project.

To National Council for Scientific and Technological Development - CNPq for the financial support.

To Air Force Office of Scientific Research - AFOSR for the financial support.

To the Center for Computational Engineering and Science - CCES/UNICAMP for the support and use of the computational facilities.

To CENAPAD for the support of computational facilities.

Pola o q.

Resumo

Esta tese apresenta uma abordagem multiescala para analisar a falha dinâmica intergranular em materiais policristalinos 3D. O modelo compreende as escalas meso e atômica usando o método dos elementos de contorno (BEM) e a dinâmica molecular (MD), respectivamente. Na mesoescala, é considerada uma estrutura policristalina detalhada, onde grãos apresentam morfologia estocástica, orientações cristalinas aleatórias e defeitos iniciais que são incluídos no modelo físico. Devido ao caráter heterogêneo, os materiais policristalinos tendem a ser macroscopicamente isotrópicos quando o número de grãos é abundante. Este fato facilita avaliar a influência dos efeitos dinâmicos sobre o comportamento mecânico dos policristais. A ausência de modelos dinâmicos analíticos para esses materiais estocásticos tem sido um desafio na validação dos resultados numéricos. Portanto, um novo esquema computacional é proposto para mostrar a validade da formulação elastodinâmica do BEM para estes materiais. As ondas de tensão e de deformação propagam-se através do policristal, induzindo o material a ser mais suscetível a falhas. A falha intergranular é governada pela densidade de energia crítica, levando em consideração a dependência da densidade de energia com a estrutura atômica das interfaces de um conjunto de nano-contornos de grão analisados. Para vincular as escalas, e devido à elevada variação das propriedades mecânicas com respeito ao tamanho da escala, a metodologia de escalonamento assintótico da tensão de escoamento é aplicada como uma aproximação. Assim, os resultados numéricos da falha dinâmica intergranular são apresentados para várias condições dinâmicas de carga.

Palavras-chave: Multiescala; Falha dinâmica; Densidade de energia; Método dos elementos de contorno; Dinâmica molecular.

Abstract

This thesis presents a multiscale approach to analyze the dynamic intergranular failure in 3D polycrystalline materials. The model comprises the meso and atomistic scales using the boundary element method (BEM) and molecular dynamics (MD), respectively. A detailed polycrystalline structure is considered in the mesoscale, where stochastic grain morphologies, random crystalline orientations and initial defects are included in the physical model. Owing to its heterogeneous character, polycrystal aggregates tend to be macroscopically isotropic when the number of crystal grains is large. This fact facilitates the evaluation of the influence of the dynamic effects on the mechanical behavior. The absence of analytical dynamic models for these stochastic materials has been a challenge in validating the numerical results. Therefore, a computational framework is proposed to show the validation of the elastodynamic BEM formulation for these materials. Stress and strain waves propagate through the polycrystal, inducing the material to be more susceptible to fail. The intergranular failure is governed by the critical energy density, taking into account the energy density dependency on the interface lattice structures of a set of nano-grain boundaries. In order to connect the scales, and due to the high variation of the mechanical properties with respect to the scale size, the asymptotic scaling methodology applied to the yield strength is adopted as an approximation. Finally, numerical results of the dynamic intergranular failure are presented for various dynamic loads.

Keywords: Multiscale; Dynamic failure; Energy density; Boundary element method; Molecular dynamics.

List of Figures

1.1	Multiscale approach.	23
1.2	Polycrystalline cubic boron nitride tool inserts (GURAV ET AL., 2015).	26
1.3	Improvements in strength-toughness combinations of some newer aluminium alloys (WILLIAMS AND STARKE, 2003).	27
2.1	3D polycrystalline structure.	32
2.2	Mesh description.	33
2.3	Multi-compiler algorithm C++/C of the mesh generator.	34
2.4	Polycrystalline structure of 100 grains: (a) $\rho_d = 1$ and (b) $\rho_d = 2$	35
2.5	Polycrystalline structure of 150 grains using $\rho_d = 1$: (a) Elements of 100 generated structures and (b) normalized grain volumes V_{gr} of one Voronoi tessellation.	35
2.6	Parallel algorithm of interfaces.	36
2.7	Distribution of crystalline orientation of lattice HCP structure.	38
2.8	Integration scheme of Barnett-Lothe tensor.	39
2.9	Algorithm: database of Fourier coefficients $\lambda_{uv}^{(m,n)}$ for a specific material.	42
3.1	Linear three-node discontinuous element.	46
3.2	Parallel algorithm: matrices \mathbf{H}^g , \mathbf{G}^g and \mathbf{M}^g	49
3.3	Interfaces.	52
4.1	Kinematic boundary conditions: (a) ε_x , (b) ε_y , (c) ε_z , (d) ε_{xy} , (e) ε_{yz} and (f) ε_{xz}	56
4.2	Algorithm to evaluate \bar{E} and \bar{G}	61
4.3	Macroscopic properties: (a) Young's modulus of Cu, (b) shear modulus of Cu, (c) Young's modulus of Zn and (d) shear modulus of Zn.	63
4.4	Histogram and normal distribution: (a) Young's modulus of Cu, (b) shear modulus of Cu, (c) Young's modulus of Zn and (d) shear modulus of Zn. For a 210 grains specimen.	64
4.5	(a) Physical model of 180 grains, $L = 1$ mm and boundary conditions: (b) step, (c) ramp and (d) harmonic loads.	70
4.6	Algorithm to evaluate dynamic time-dependent $u_y(t)$ response.	71
4.7	Fe under step load. The analytical solution is given in (CLOUGH AND PENZIEN, 2003).	73
4.8	Cu under ramp load. The analytical solution is given by the Equation (4.20).	74
4.9	Zn under harmonic load. The analytical solution is given by the Equation (4.21).	75
4.10	(a) Physical model of 180 grains, $L = 0.5$ mm and (b) step load.	77
4.11	Number of elements: (a) mesh I: 4,775, (b) mesh II: 8,332, and (c) mesh III: 14,922.	78

4.12	Comparison among y -displacements of meshes I, II, and III with $\Delta\tau = 40$ ns. . . .	79
4.13	Comparison among y -displacements of meshes I, II, and III with $\Delta\tau = 30$ ns. . . .	79
4.14	Comparison among y -displacements of meshes I, II, and III with $\Delta\tau = 20$ ns. . . .	80
5.1	Periodic boundary conditions: (a) cell, (b) super cell and (c) simulation domain. . .	83
5.2	EAM Potential for Fe.	94
5.3	Bicrystal: (a) description, (b) mixed, (c) tilt and (d) twist GBs.	97
5.4	Bicrystal structure of a STGB $\Sigma 51\{1\bar{1}10\}$ in the $\langle 110 \rangle$ direction.	100
5.5	Detailed description of the STGB $\Sigma 51\{1\bar{1}10\}$ bicrystal.	101
5.6	Algorithm to evaluate the GB energy using LAMMPS.	103
5.7	GB energy of the tilt $\Sigma 99\{1\bar{1}14\}$ in terms the initial temperature and the overlap parameters.	105
5.8	GB energy of the twist $\Sigma 91\{10\bar{1}\bar{9}\}$ in terms the initial temperature and the overlap parameters.	105
5.9	GB energy of STGBs $\langle 110 \rangle$ in terms of the tilt angle θ	106
5.10	GB energy of STwGBs $\langle 111 \rangle$ in terms of the twist angle φ	107
6.1	Nanoscale specimen for failure simulations.	108
6.2	Algorithms for tensile and shear LAMMPS scripts.	110
6.3	Stress-strain constitutive behavior for different GB structures: (a) tensile and (b) shear.	111
6.4	Tensile failure of $\Sigma 37(2\bar{2}\bar{1})/(2\bar{2}1)$ structure: (a) $t = 50$ ps, $\sigma_n = 9.28$ GPa, $\varepsilon_n = 5\%$; (b) $t = 70$ ps, $\sigma_n = 10.26$ GPa, $\varepsilon_n = 7\%$; (c) $t = 80$ ps, $\sigma_n = 10.16$ GPa, $\varepsilon_n = 8\%$; (d) $t = 90$ ps, $\sigma_n = 9.39$ GPa, $\varepsilon_n = 9\%$	113
6.5	Shear failure of $\Sigma 37(2\bar{2}\bar{1})/(2\bar{2}1)$ structure: (a) $t = 50$ ps, $\sigma_{yz}^+ = 3.38$ GPa, $\varepsilon_{yz}^+ = 5\%$; (b) $t = 70$ ps, $\sigma_{yz}^+ = 2.61$ GPa, $\varepsilon_{yz}^+ = 7\%$; (c) $t = 80$ ps, $\sigma_{yz}^+ = 1.31$ GPa, $\varepsilon_{yz}^+ = 9\%$; (d) $t = 110$ ps, $\sigma_{yz}^+ = 0.45$ GPa, $\varepsilon_{yz}^+ = 11\%$	114
6.6	Critical tensile E_{nc} energy density depending on the GB structure.	117
6.7	Critical shear energy densities: (a) $E_{xz_c}^+$ and (b) $E_{xz_c}^-$, both depending on the GB structure.	118
6.8	Critical shear energy densities: (a) $E_{yz_c}^+$ and (b) $E_{yz_c}^-$, both depending on the GB structure.	119
6.9	Energy failure diagram: (a) <i>tensile-shear</i> (xz^+) and (b) <i>tensile-shear</i> (xz^-).	121
6.10	Energy failure diagram: (a) <i>tensile-shear</i> (yz^+) and (b) <i>tensile-shear</i> (yz^-).	121
6.11	Artificial 80 grains polycrystalline structure, discretized with 18,200 boundary elements.	123
6.12	Failure algorithm.	125

6.13	Initial cracked model.	126
6.14	Failure propagation and damage evolution.	127
6.15	Macroscopic behavior: (a) constitutive stress-strain relationship and (b) overall de- formation as a function of time.	128
6.16	Total displacement, units in [nm].	129
6.17	Different views of failure at 185 ns.	130
B.1.1	Linear three-node elements: (a) continuous and (b) discontinuous.	155

List of Tables

2.1 Performance: algorithm of interfaces.	37
3.1 Performance: algorithm of matrices.	50
4.1 Anisotropic elastic constants for Zn (TROMANS, 2011) and Cu (HUNTINGTON, 1958) in [GPa].	57
4.2 Number of DOF for different grain numbers.	57
4.3 Absolute measure of anisotropy of Cu and Zn.	60
4.4 Effective and confidence interval of Young's modulus in [GPa], based on different numbers of grains per aggregate.	65
4.5 Effective and confidence interval of shear modulus in [GPa], based on different numbers of grains per aggregate.	65
4.6 Comparison of elastic constants of Cu in [GPa].	67
4.7 Comparison of elastic constants of Zn in [GPa].	67
4.8 Comparison of Young's, shear moduli and deviation of Cu in [GPa].	68
4.9 Comparison of Young's, shear moduli and deviation of Zn in [GPa].	68
4.10 Simulations.	69
4.11 Effective Young's modulus in [GPa] evaluated in a 210 grain specimen.	69
4.12 Elements and DOF of 180 grains polycrystal aggregate.	70
4.13 Instants of sudden changes of for Fe simulation with step load.	76
4.14 Maximum and minimum values of $Er(\bar{u}_y)$ and 3σ in [μm].	76
4.15 Simulation times.	78
5.1 Velocity Verlet algorithm.	91
5.2 GB categories.	98
5.3 Variables to be fitted.	104
5.4 Number of atoms used to model the STGBs and STwGBs, from the structures pre- sented in Table C.3.1.	106
6.1 Details of the nanoscale specimens, GB energy expressed in [mJ/m^2] and length values in [\AA].	109
6.2 Dynamic boundary conditions for tensile and shear tests.	109
6.3 Critical stress values expressed in [GPa] and GB energy in [mJ/m^2].	112
6.4 Limit scaling values for tensile test, length expressed in [μm] and stress in [GPa].	117
6.5 Limit scaling values for shear tests, length expressed in [μm] and stress in [GPa].	118
6.6 Limits of φ ratio.	122
C.1.1 Parameters for the EAM potential energy functions.	158

C.1.2	The remaining coefficients of the EAM potential.	159
C.3.1	Grain boundaries, symmetric $\langle 110 \rangle$ tilt and $\langle 111 \rangle$ twist. (Continuation).	163
C.4.1	Set of GB structures for failure analysis. (Continuation).	165

List of Symbols and Acronyms

Symbols

\bar{L}_e	- Average length
L_e	- Current edge length
ρ_d	- Density parameter of discretization
n_s	- Number of segments
A_{max}	- Maximum triangle area constraint
$(x_{max}, y_{max}, z_{max})$	- Box size of polycrystalline structure
N_{gr}	- Number of grains
V_{gr}	- Grain volume
V_{gr}^{max}	- Grain volume
\mathbf{C}	- Stiffness tensor
$\bar{\mathbf{C}}$	- Effective homogenized stiffness tensor
$\hat{\mathbf{C}}$	- Apparent homogenized stiffness tensor
\hat{K}	- Apparent bulk modulus
\hat{G}	- Apparent shear modulus
\bar{E}	- Effective Young's modulus
$\bar{\nu}$	- Effective Poisson's modulus
\mathbf{C}^V	- Stiffness Tensor, Voigh and Reuss bonds theory
\mathbf{S}^R	- Compliance Tensor, Voigh and Reuss bonds theory
A^L	- Anisotropic factor
$\Delta\tau$	- Time step for mesoscale analysis
N_{times}	- Number of time steps for mesoscale analysis

Σ	-	Reciprocal value of the density of coincident sites
N	-	Number of atoms of the specimen at the nanoscale
P	-	Pressure of the macrostate at the nanoscale
V	-	Volume of the specimen at the nanoscale
T	-	Temperature of the macrostate at the nanoscale
E	-	Energy of the specimen at the nanoscale
H	-	Enthalpy of the macrostate at the nanoscale
γ_{GB}	-	Grain boundary energy
E_c	-	Cohesive energy
a	-	Lattice parameter
temp_i	-	Initial temperature at the nanoscale
overlap	-	Overlap parameter for atomistic simulations
E_{nc}	-	Critical tensile energy density
E_{sc}	-	Critical shear energy density
$\dot{\epsilon}_i$	-	Applied deformation rate at nanoscale
D_{na}	-	Size of the nanoscale
σ_{na}	-	Tensile strength at the mesoscale
σ_{na_s}	-	Shear strength at the mesoscale
D	-	Nominal size of the mesoscale
σ_o	-	Nominal tensile strength at the mesoscale
D_m	-	Size of the microscale
σ_m	-	Tensile strength at the microscale
σ_{m_s}	-	Shear strength at the microscale
η	-	Ratio between shear and tensile strengths at the nano and micro scales
E_n	-	Tensile energy density
E_s	-	Shear energy density
φ	-	Ratio between shear and tensile energy densities at the microscale
d	-	Damage coefficient at the microscale

Acronyms

ATGB	-	Asymmetrical Tilt Grain Boundary
ATwGB	-	Asymmetrical Twist Grain Boundary
bcc	-	Body Centered Cubic
BEM	-	Boundary Element Method
NVT	-	Canonical Ensemble
CZM	-	Cohesive Zone Model
CSL	-	Coincidence-Site Lattice
CG	-	Conjugate Gradient
DOF	-	Degrees Of Freedom
DRBEM	-	Dual Reciprocity Boundary Element Method
DRP	-	Dual Reciprocity Points
EAM	-	Embedded Atom Method
fcc	-	Face Centered Cubic
FEM	-	Finite Element Method
FS	-	Finnis-Sinclair
GB	-	Grain Boundary
hcp	-	Hexagonal Closed Package
NPH	-	Isoenthalpic–isobaric Ensemble
NPT	-	Isothermal–isobaric Ensemble
LAMMPS	-	Large Scale Atomic/Molecular Massively Parallel Simulator
MPI	-	Message Passing Interface
NVE	-	Microcanonical Ensemble
MD	-	Molecular Dynamics
MUMPS	-	Multifrontal Massively Parallel Sparse
RIM	-	Radial Integration Method
RVE	-	Representative Volume Element
STGB	-	Symmetric Tilt Grain Boundary
STwGB	-	Symmetric Twist Grain Boundary

Table of Contents

List of Figures	x
List of Tables	xiii
List of Symbols and Acronyms	xxi
Table of Contents	xviii
1 Introduction	20
1.1 State of the art	24
1.2 Industrial applications	26
1.3 Motivation	28
1.4 Objectives	28
1.5 Contributions	29
2 Material modeling	32
2.1 Polycrystalline structure mesh	32
2.2 Constitutive model	37
2.3 Anisotropic fundamental solution	38
3 Elastodynamic BEM formulation	43
3.1 Integral formulation	43
3.2 Discretization	45
3.3 Time domain integration	50
3.4 Multidomain assembly	51
4 Dynamic behavior of polycrystalline materials	55
4.1 Effective macroscopic properties	55
4.1.1 Effective Young's and shear moduli results	62
4.2 Dynamic behavior	69
4.2.1 Analytical isotropic models	72
4.2.2 Dynamic time-dependent results	73
4.2.3 Mesh and time step dependency	77
4.3 Computational aspects	80

5	Grain boundary model	82
5.1	Molecular dynamics	82
5.1.1	Energy minimization	84
5.1.2	Time integration method	87
5.1.3	Interatomic potentials	91
5.1.4	Stress tensor	95
5.2	Grain boundary energy	96
5.2.1	GB categories	97
5.2.2	Coincidence-Site Lattice	98
5.2.3	GB Simulations	102
6	Multiscale model	108
6.1	Critical energy densities	108
6.1.1	Asymptotic scaling	115
6.2	Intergranular failure	119
6.2.1	Generalized energy failure criterion	120
6.2.2	Mesoscale failure	122
7	Conclusions	131
	References	133
	Appendices	149
A	– Anisotropic fundamental solution	149
A.1	Barnett–Lothe in terms of Stroh’s eigenvalues	149
A.2	Displacement fundamental solution and its derivatives	150
B	– Triangular boundary elements	155
B.1	Shape functions and its derivatives	155
C	– Atomistic modeling	158
C.1	EAM potential parameters	158
C.2	Thermal process and energy minimization	159
C.3	GB structures for energy validation	162
C.4	GB structures for failure analysis	164
C.5	GB failure scripts	166

1 Introduction

Many industrial developments and applications used metallic materials in their components, basically designed to prevent the component failure that could lead to the collapse of the overall system. Additional to the optimal geometric design, the material behavior takes place on the configuration in the limits of the imposed environmental and boundary conditions. Important physical effects can be captured in the material behavior when very small length scales are considered in the analysis. Strong variations in the geometrical morphology, material properties and defects are observed when a microscale analysis is taken into account. Therefore, improvements in failure analyses can be achieved including the microscale behavior through bridging scale transitions. Furthermore, the atomistic scale can be considered in order to obtain a more realistic failure modeling of the mesoscale.

Microscopically, metallic materials are composed by randomly oriented crystal aggregates. From the macroscale, each material point is represented by a set of non-periodic polycrystal aggregates. Then, the macroscopic elastic properties are statistically approximated by the assembly of random morphology grains with their own crystalline orientations. The constitutive model of each grain can be assumed as an anisotropic elastic medium, where the elastic properties depend on the lattice structure, e.g. cubic or hexagonal crystals. It is a difficult task to reproduce artificial polycrystalline structures owing to its random morphology. The mesh generation is a critical task to adequately model polycrystalline materials. Process image reconstruction from experimental data, Voronoi and Laguerre tessellation meshing and remeshing are, in particular, useful for non-periodic polycrystalline aggregates. Computational frameworks to build polycrystalline structures can be found in the literature. The most common is the Voronoi tessellation for artificial structures as Voro++ (RYCROFT, 2009) and Neper (QUEY AND RENVERSADE, 2018). Several schemes were presented to discretize the Voronoi structure, such as superficial meshes for boundary elements (GULIZZI ET AL., 2018) and volumetric meshes (FRITZEN ET AL., 2009; BROMMESSON ET AL., 2016) for the finite element method (FEM). The mechanical response of these anisotropic materials quantified by the displacement and traction fields is evaluated using the 3D fundamental solution for general anisotropic materials proposed by Tan et al. (2013). As the displacement field is represented by double Fourier series, this fundamental solution offers the possibility to evaluate its coefficients once for each crystalline orientation. Hence, it represents an advantage for this analysis, because with this fundamental solution a database of Fourier coefficients can be generated for each material, considering a large number different crystalline orientations.

According to the description of the microscopic material, the BEM benefits from the model of high stress and strain gradients using the surface discretization of the polycrystalline aggregate. The mesoscale model considers the interfaces as perfect flat surfaces where the analysis is conducted applying traction equilibrium and displacement compatibility through the multidomain analysis. The grain boundaries (GBs) are the transition planes of the two adjacent crystalline orientations, being an important object of study for intergranular failure analysis. At the macroscale, metallic materials have the tendency to be isotropic when the number of grains is large. As validation of the static model, a convergence analysis of the effective macroscopic elastic properties were developed in this work, and presented in (GALVIS ET AL., 2018a) using the elastostatic BEM formulation based on previous studies (FRITZEN ET AL., 2009; BENEDETTI AND ALIABADI, 2013B). Reliable results were obtained, showing the macroscopic isotropic trend when more grains are contained in the micro-volume.

The application of dynamic loads with a rapid rate of change over time leads to other physical considerations, when compared with static or quasi-static models. The high-rate load conditions turn the mechanical fields dependent of the inertial force, which resists the acceleration induced in the body. These physical effects under these conditions are the main characteristic of dynamics problems (CLOUGH AND PENZIEN, 2003). Furthermore, the dynamic deformation due to high-rate loads should be analyzed. In this case, there is a high strain gradient in a part of the body, and the remaining parts do not yet experience stresses. Strain and stress waves propagate through the solid at a specified velocity (MEYERS, 1994). Dynamic loads play an important role in failure analysis, as the material is more susceptible to failure under impulsive or high-rate strain loads, which affects the fracture behavior (GROSS AND SEELIG, 2006), it requires a dynamic fracture mechanics analysis (ALBUQUERQUE ET AL., 2004). In this work, a new computational framework for the dynamic analysis of 3D hexagonal (hcp) and cubic (bcc/fcc) anisotropic polycrystalline materials is developed as presented in (GALVIS ET AL., 2018b). The dynamic effects are included by the dual reciprocity BEM (DRBEM) (KÖGL AND GAUL, 2000A; GAUL ET AL., 2003), using a small time step of $\tau = 15$ ns. In order to validate the dynamic anisotropic model, in the absence of analytical solutions for anisotropic media, comparisons with isotropic macroscale dynamic models are shown, using the effective Young's modulus. These isotropic models and effective elastic properties are available in the literature. The accuracy of this model depends on the number of crystal aggregates, that must be large enough to get an approximation of an isotropic material. Notably, results were achieved showing the degradation in the numerical response when the simulation time increases.

The failure analyses have advanced from conventional fracture mechanics and cohesive models. Nowadays, there are several numerical studies of brittle failure intergranular and transgranular 3D polycrystalline materials, through the measurement of the mechanical degradation of the material commonly using approaches such as cohesive zone models (CZM) (GULIZZI ET AL., 2018), quasi-continuum methods (LUTHER AND KÖNKE, 2011) or homogenized atomistic-continuum techniques (REN AND LI, 2013). This work focuses on the intergranular failure process in a multiscale atomistic-continuum modeling of GBs. In the atomistic scale, the GB model regards the transition lattice structure produced by the collapse of two adjoining interior grain lattices. It is widely known that the atomistic media is governed by the thermodynamic state and the force field. Moreover, the potential energy serves to identify the more susceptible failure structures. In the interfaces that contain a high quantity of defects, owing to the broken bonds of the transition lattice, a high potential energy reflects a failure interface zone. The failure is characterized by the critical energy density atomistically assessed for different modes, using the generalized energy failure criterion proposed by Qu et al. (2016). This criterion offers a straightforward way to evaluate failure at the microscale, taking into account a certain mixed level of ductile and brittle failure occurring in the interface. Due to the lack of available data of the critical energy densities for tensile and shear modes, a MD model of GBs is implemented. Additionally, using this strategy, the failure criterion is extended to consider the variation in the lattice structures in the interfaces. The nature of metallic materials in its mesoscale, flaws and defects such as intergranular cracks are contained in the polycrystalline structure. These initial defects act as potential weak zones where the failure could initiate. While the length scale increases, the magnitude of the failure stress drastically decreases. Therefore, the bridging approach to obtain the critical energy densities at the mesoscale represents a challenge that is worth of investigation.

In the analysis through different length scales, mechanical properties of materials vary owing to their size and rate dependence. It is well known that the yield stress decreases with the specimen size and increases with the strain rate (BASKES AND PLIMPTON, 2001). This represents a challenge on multiscale modeling due to the limitations of experimental available data. At the nanoscale, the yield stress limit occurs mainly for the nucleation of dislocations in the material. Therefore, a larger size of material can result in a higher chance for nucleating the dislocation, which yields a lower initial stress (HORSTEMEYER AND BASKES, 1999; GUO ET AL., 2007). Using MD simulations of single-crystal copper and nickel, Guo et al. (2007) showed that a critical strain-rate exists, below which the yield stress becomes nearly constant. They also analyzed the length scale dependence, that also affects the yield strength. Similar to the strain-rate case, when the length of the scale increases the yield stress tends to decrease. All the studies cited developed their results considering

bulk lattice structures. Another approach presented by Hammami and Kulkarni (2017), used grain boundary sliding in nanostructures to investigate rate dependence using atomistic simulations. They obtained similar results of rate dependence of mechanical properties for a tilt GB of aluminum. For larger scales, the scaling of properties is based on a continuum formulation of the geometrically necessary dislocations to produce plastic strain; some classical and recognized publications treating these phenomenons are (GAO ET AL., 1999; BAZANT, 2002). A useful formulation was presented by (CHEN ET AL., 2005; CHEN ET AL., 2007). They developed the hypersurface that combines strain-rate and the specimen size effects on material properties, and also showed functions to represent the size effect that are considered to be used in this work after some assumptions.

This thesis presents a multiscale scheme to analyze the dynamic intergranular failure in 3D polycrystalline materials. The model comprises the meso and atomistic scales using BEM and MD, respectively. The dynamic analysis of the polycrystal aggregate considers crack initiation at the micro-domain. As mentioned, the failure propagates according to the criterion defined by the critical energy densities at the interfaces. In order to apply the failure criterion in the mesoscale properly, an asymptotic analysis is adapted to scale the mechanical properties from the nano and micro scales. The main BEM application is implemented in Fortran 90, parallelized on a distributed architecture memory using MPI. The atomistic evaluation of the critical energy densities is carried out from the model of the GB as a bicrystal. This gives a detailed physical description of the atomistic arrangement at the interface differing from the structure inside of the adjacent grains. Hence, GB categories given by the coincident-site lattice (CSL) model are employed to construct a statistical sample of tilt and twist GBs. Figure 1.1 illustrates the multiscale approach.

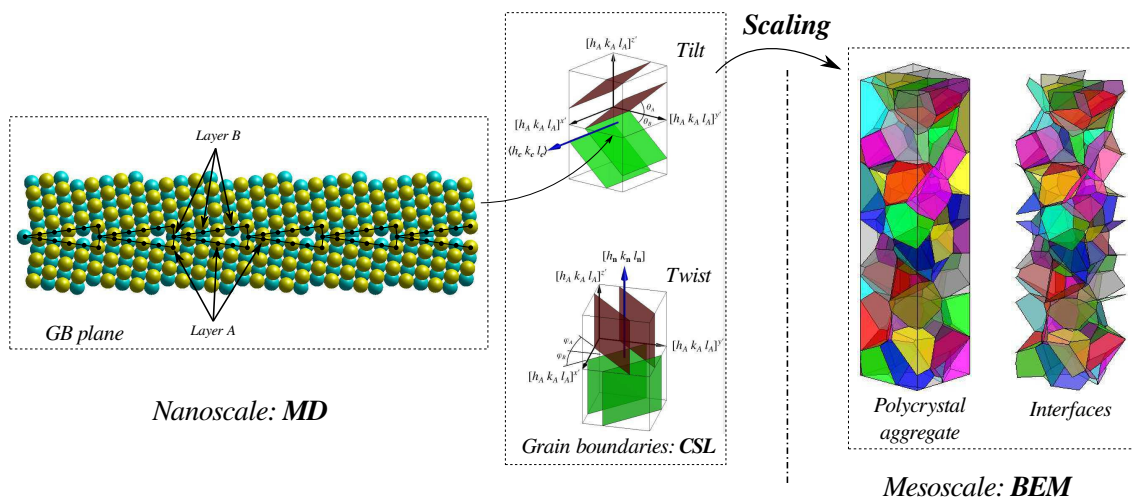


Figure 1.1: Multiscale approach.

An N -body potential must be used to describe the atomic interactions represented by the force field. Next, the atomistic analysis of failure contemplates annealing and quenching processes, the bicrystal relaxation and the dynamic evolution of the system under high-rate deformation boundary conditions. All the atomistic simulations are achieved using the Large-scale Atomic/Molecular Massively Parallel Simulator (LAMMPS) (PLIMPTON, 1995) available in (<http://lammms.sandia.gov>). Thus, the critical energy density is derived from the constitutive relationship between the strain and the Virial stress tensors. Due to the incorporation of the atomistic behavior, which considers the broken bonds formed in the GBs at the interfaces, the overall multiscale approach attempts to model a more realistic intergranular failure condition.

1.1 State of the art

In the literature, previous quasi-static and dynamic failure analyses were presented using several numerical methods and strategies. Quasi-static analyses of brittle failure using the CZM and BEM can be found in (BENEDETTI AND ALIABADI, 2013A; GULIZZI ET AL., 2015; GULIZZI ET AL., 2018). These publications have shown intergranular and transgranular crack propagations by applying conventional cohesive laws obtained directly from the micro-mechanics. In addition, failure analyses using FEM were presented in (BROMMESSON ET AL., 2016; NGUYEN ET AL., 2017). Other failure analyses can be cited, such as the damage measure based on an energy criterion under cyclic loading carried out by Beckmann and Hohe (2017) using FEM. Moreover, intergranular failure considering the stress corrosion were presented by Benedetti et al. (2018) using quasi-static BEM and CZM. All the mentioned methods consist in mesoscale approaches. Some multiscale works can be cited, such as the multiscale analysis between the meso and atomistic scales presented by Ren and Li (2013). They developed a 3D atomistic-based process zone model to describe behavior of polycrystalline solids taking into account the homogenized atomistic binding energy and atomistic lattice structure using the embedded atom method and dynamic FEM. Benedetti and Aliabadi (2015) proposed the macro- and mesoscale analysis using quasi-static BEM and CZM, to evaluate the degradation on the elastic properties at the macroscale due to the effect of flaws occurring in the mesoscale. Talebi et al. (2015) presented a coupling scheme between molecular dynamics and the extended FEM via the bridging domain method to model 3D cracks and dislocations at the atomistic level. van Beers et al. (2015) characterized details of the initial structure and energy of the grain boundaries of polycrystalline materials to develop a multiscale model coupling the atomistic and continuum descriptions in copper and aluminium using the embedded

atom method of interatomic potential. Prakash et al. (2016) examined the influence of changes in grain boundary strength on microstructure dependent crack propagation in polycrystalline tungsten using the extended FEM. All the mentioned references that applied BEM analysis of intergranular and transgranular failures were carried out using elastostatic BEM formulation and conventional CZM, being different to the proposed multiscale modeling of this work.

As part of the elastostatic BEM formulation, the fundamental solution used in this work has been applied to generally anisotropic solids in (SHIAH ET AL., 2008; SHIAH ET AL., 2012). Additionally, a more specific application was presented by Rodríguez et al. (2017) that analyzed fiber composites. Problems of anisotropic elastodynamics were studied by (KÖGL AND GAUL, 2000A; KÖGL AND GAUL, 2000B; KÖGL AND GAUL, 2003). The authors introduced works treating 3D anisotropic materials, where 3D piezoelectric materials, the dynamic behavior and free vibration of anisotropic elastic solids were presented. In these publications a fundamental solution based on the Radon transform and the DRBEM, as presented by Kögl and Gaul (2000a) and Gaul et al. (2003) were used. Recently, Rodríguez et al. (2018) presented an analysis of dynamic 3D anisotropic materials. They compared two methods to transform the domain integral into a boundary integral, the DRBEM and the radial integration method (RIM) (GAO, 2002). The DRBEM showed to be more efficient than the RIM in terms of computational time, despite the RIM uses a coarser discretization.

The initial BEM algorithms were based on those developed by Rodríguez et al. (2017). He implemented the fundamental solution using quadrilateral discontinuous quadratic boundary elements. In addition, he provided the DRBEM coupled to the Houbolt's integration method for 3D analyses. All implementations parallelized in a shared memory architecture with Fortran-OpenMP. In this thesis, these algorithms were re-implemented for triangular boundary elements with a linear interpolation. Moreover, due to the incorporation of a sparse analysis of the general system of equations. Moreover, the number of degrees of freedom (DOF) were drastically increased about 86% from approximately 35,000 to 250,000 DOF. Additionally, improvements in terms of efficiency were attained using Fortran-MPI parallelization in the most critical sections of the BEM application.

1.2 Industrial applications

Multiple industrial applications use metal alloys and ceramics in their components. The automotive and aerospace industries are developing light alloys such as aluminium silicon (Al–Si) and aluminium zirconium (Al–Zr) due to their excellent mechanical properties and low weight to strength ratio. In order to improve these characteristics in metal alloys, grain refinement is usually used in industry through methodologies such as presented by Djan (2016). The analysis of the structural integrity and the constitutive behavior of these materials, under severe environment conditions, is essential to predict the performance in present and future applications. Important physical properties such as yield strength, Young's moduli, fracture toughness and thermal conductivity depend on the material microstructure. The design of optimal structures and microstructures is important for hardware components in aerospace applications, where there is a necessity to optimize weight and dimensions to improve the performance (SUNDARARAGHAVAN AND ZABARAS, 2008). Three research studies on polycrystalline materials that achieved relevance in their pathways to impact are mentioned.

In manufacturing processes, tipped tools are of great importance. Manufacturing industries use ceramic cutting tool inserts on large scale but, on the other hand, environmental regulations are imposed to tool manufacturers. Many of the manufacturing industries have started using polycrystalline diamond and polycrystalline cubic boron nitride cutting tools, Fig. 1.2, which are less harmful to the environment. The automotive and aerospace industries use these materials for gaining precision and better surface finishing (GURAV ET AL., 2015).

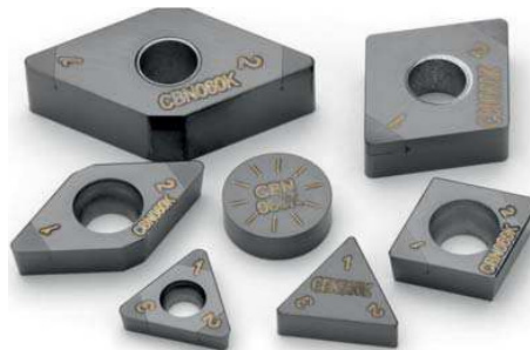


Figure 1.2: Polycrystalline cubic boron nitride tool inserts (GURAV ET AL., 2015).

The two major passenger aircraft manufacturers introduced materials with evolutionary im-

provements. The advanced materials include a number of improved aluminium and titanium alloys and polymer matrix composites, as well as laminates and lightweight sealants (WILLIAMS AND STARKE, 2003). Some examples of the aluminium alloys are shown in Fig. 1.3.

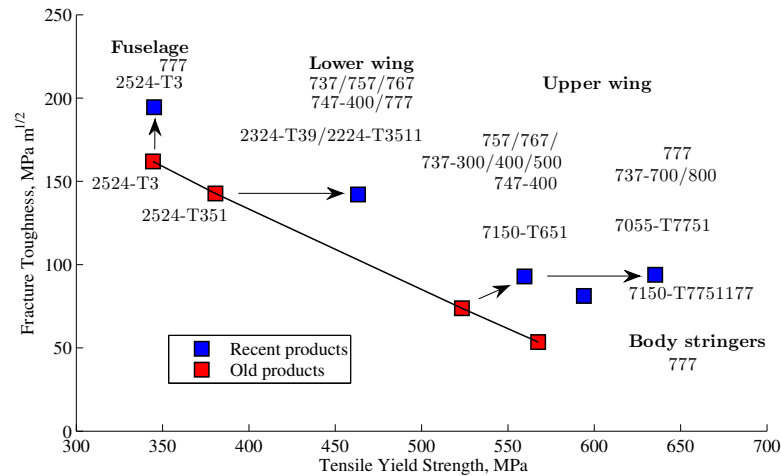


Figure 1.3: Improvements in strength-toughness combinations of some newer aluminium alloys (WILLIAMS AND STARKE, 2003).

Improvements in fracture toughness and greater resistance to fatigue crack growth helped in the elimination of tear straps in a weight-efficient manner (WILLIAMS AND STARKE, 2003).

Composite materials are being used in aircrafts, cars, turbine blades, and other products. Other materials, like graphene, hold even greater promise and may completely revolutionize industrial design¹. Large-area graphene films, which are necessary for industrial applications, are typically polycrystalline, composed of single-crystalline grains of varying orientation joined by grain boundaries (YAZYEV AND CHEN, 2014). Recently, a Chinese company incorporated grains of graphene in its cell phones to improve conductivity. Flakes of quasicrystals have been molded into frying pans and metal surgical instruments to increase their durability. Graphene is 200 times stronger than steel and the thinnest material on earth (1 million times thinner than a human hair). Lightweight aluminum alloys have now replaced high-strength steel in bumper systems, crash ring components and intrusion beams. In aircraft engines, super-hard alloys that are resistant to extreme temperatures can help improve energy conversion and reduce fuel costs².

¹<http://www.sandvik.coromant.com/en-us/aboutus/lookingahead/>

²<http://www.sandvik.coromant.com/en-us/aboutus/lookingahead/articles/Pages/a-material-revolution.aspx>

1.3 Motivation

Multiscale modeling has been increased in different scientific fields, owing to the advantage over the conventional methods that work at a single scale. The computational advances allow to consider the inclusion of models with a large DOF. The field of material modeling is being benefited. Then, it is possible to analyze additional physical effects present in the material coupling different space and time scales. An example is the modeling at the mesoscale using continuum mechanics formulation, and at the atomistic scale using quasi-continuum or atomistic methods. Physical atomic and molecular effects, such as the atomic vibration of bonds in a femtoseconds time scale, the presence of vacancies, nanovoids and microcracks are possible to be considered. The motivation to research metallic materials at meso and atomistic scales is more specifically defined as: i) the study of the effects on the failure of polycrystal aggregates due to the high-rate boundary conditions applied. ii) This type of load produces strain and stress waves traveling through the solid, increasing the sensitivity of polycrystalline structures to failure and propagation crack paths in the interfaces between grains. iii) The definition of a failure criterion from the atomistic analysis of the GBs using N -body sophisticated potentials. iv) In terms of implementation, the challenge is the reduction of the computational time required by this application, especially in the mesoscale model, through efficient parallelized algorithms implemented on distributed memory architecture.

1.4 Objectives

The main objective of this thesis is the formulation of a new multiscale approach of dynamic failure in 3D polycrystalline materials using BEM at the mesoscale and MD to model the atomistic scale at the interfaces. At the mesoscale, the polycrystalline aggregate is generated using Voronoi tessellation and discretized using triangular boundary elements. As mentioned, each grain is modeled as an anisotropic continuum body with stochastic crystalline orientation. The dynamic traction and displacement fields are evaluated using the DRBEM and the fundamental solution based on double Fourier series. At the atomistic scale, a large number of tilt-twist periodic GBs for bcc cubic bi-crystals are analyzed, where the MD simulations are carried out using LAMMPS. The failure criterion is based on the energy density considering coupled failure modes. Finally, the intergranular failure path propagates in the polycrystalline structure under dynamic boundary conditions. More specific objectives are listed below.

- Implementation and discretization of 3D polycrystalline structure mesh generator using Voro++ and Triangle libraries on (C++/C) respectively.
- Implementation of the parallelized dynamic BEM formulation composed by the fundamental solution based on double Fourier series, the DRBEM and the multidomain algorithm on a distributed memory architecture using MPI-Fortran.
- Homogenization and dynamic analyses of 3D polycrystalline materials at the mesoscale.
- Implementation of atomistic MD simulations of tilt-twist GBs using LAMMPS to evaluate the critical energy densities.
- Scaling and coupling the generalized energy failure criterion to the polycrystalline aggregate to analyze the dynamic intergranular failure.

1.5 Contributions

- The modeling of 3D polycrystalline materials using elastostatic and elastodynamic BEM formulations, both applying the fundamental solution based on double Fourier series and the DRBEM. This implementation is efficient, due to the previous generation of a large Fourier coefficient database for a specific material.
- The analysis of cubic and hexagonal polycrystal aggregates that macroscopically convergent to isotropic materials, using average homogenization on the grain surfaces. This work led to the publication: (GALVIS ET AL., 2018a). The novelties of this publication were the use of the above mentioned formulation, the MPI parallelized and serial computational algorithms, see sections 2 and 3. Reliable results were obtained, showing the validation of the elastostatic BEM formulation and implementation, see section 4.1.
- The dynamic analysis of cubic and hexagonal polycrystal aggregates. This study was carried out for step, ramp and harmonic dynamic loads. Using the results of the last work, a statistical analysis is applied to demonstrate that the dynamic behavior of polycrystalline materials convergent to an approximate dynamic behavior of macroscopic isotropic materials. This work led to the paper: (GALVIS ET AL., 2018b). The publication presents a new computational framework to analyze the 3D dynamic behavior of polycrystals. Due to the lack of analytical models for the dynamic response of anisotropic solids, with the results of this publication it

was possible to validate the elastodynamic BEM formulation for anisotropic materials, see section 4.2.

- This is a multiscale approach to analyze dynamic intergranular failure in 3D polycrystalline materials. This is the first time the elastodynamic BEM formulation and the failure criterion based on the energy density were employed, considering its variation depending on the crystalline orientation of the GBs analysed via MD modeling. The bridging approach is carried out using the asymptotic scaling methodology applied to the mechanical properties such as the yield strength. Finally, the dynamic intergranular failure at the mesoscale under distinct boundary conditions is predicted.

This thesis has generated the following publications in international journals:

- 1 Galvis., A. F., Rodriguez, R. Q., and Sollero, P. (2018). Dynamic analysis of three-dimensional polycrystalline materials using the boundary element method. *Computers & Structures*, 200:11–20.
- 2 Galvis., A. F., Rodriguez, R. Q., and Sollero, P. (2018). Analysis of three-dimensional hexagonal and cubic polycrystals using the boundary element method. *Mechanics of Materials*, 117:58–72.
- 3 Rodríguez, R., Galvis, A. F., Sollero, P., Tan, C. L., and Albuquerque, E. L. (2018). Transient dynamic analysis of generally anisotropic materials using the boundary element method. *Acta Mechanica*, 229:1893-1910.
- 4 Galvis, A. F. and Sollero, P. (2016). 2D analysis of intergranular dynamic crack propagation in polycrystalline materials a multiscale cohesive zone model and dual reciprocity boundary elements. *Computers & Structures*, 164:1–14.
- 5 Alvarez., J. E., Galvis, A. F., and Sollero, P. (2018). Multiscale dynamic transition of 2D metallic materials using the boundary element method. *Computational Materials Science*, 155:383-392.
- 6 Rodriguez, R. Q., Galvis, A. F., Sollero, P., Tan, C. L., and Albuquerque, E. L. (2017). Fast BEM multi-domain approach for the elastostatic analysis of short fibre composites. *European Journal of Computational Mechanics*, 26(5-6):525–540.

- 7 Prada, D. M., Galvis, A. F., Alcântara, A. C., and Sollero, P. (2018). 3D Boundary element meshing for multiscale bone anisotropic analysis. *European Journal of Computational Mechanics*, (doi:10.1080/17797179.2018.1524054).

Publications in international conferences:

- 1 Alvarez, J.E., Galvis, A.F., and Sollero, P. (2018). Micro dynamic failure of 2D crystal aggregate structures using BEM and a hierarchical multiscale cohesive zone model. *19th International Conference on Boundary Element and Meshless Techniques - BETEQ*, pp.213-219, Malaga, Spain.
- 2 Alvarez, J.E., Galvis, A.F., and Sollero, P. (2017). Macro-Micro scale dynamic analysis of 2D polycrystalline materials using the boundary element method. *XXXVIII Ibero-Latin American Congress on Computational Methods in Engineering - CILAMCE*, (doi:10.20906/CPS/CILAMCE2017-0088), Florianopolis-SC, Brazil.
- 3 Prada, D.M., Galvis, A.F., and Sollero, P. (2017). Superficial 3D mesh generation process using multimedia software for multiscale bone analysis. *18th International Conference on Boundary Element and Meshless Techniques - BETEQ*, pp.126-131, Bucharest, Romania.
- 4 Galvis, A.F., Rodríguez, and R.Q., Sollero, P. (2016). Intergranular fracture in polycrystalline materials using the dual reciprocity boundary element method. *16th International Conference on Boundary Element and Meshless Techniques - BETEQ*, pp.254-258, Valencia, Spain.

2 Material modeling

Polycrystalline materials are represented by the aggregate of several crystals or grains with proper crystalline orientations and planes. At the macroscale, these materials are commonly modeled as isotropic bodies due to overall homogenized effects. At the mesoscale, each grain is modeled as linear elastic anisotropic material as presented in the majority of metallic and ceramic crystalline materials. Artificial polycrystalline morphologies are generated and discretized to model the stochastic constitutive elastic behavior.

2.1 Polycrystalline structure mesh

A random geometrical structure is generated to represent the artificial polycrystalline material. Several methods were developed in the literature to achieve this task, widely used for FEM models. The nature of the BEM discretization requires a surface mesh that is generated following the scheme presented by Fritzen et al. (2009) and Galvis et al. (2018a). A polycrystalline structure is shown in Figure 2.1 using Voronoi tessellation.

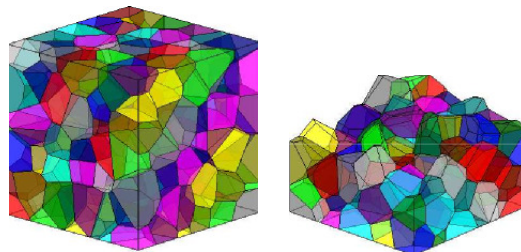


Figure 2.1: 3D polycrystalline structure.

This artificial structure was generated using the Voro++ library (RYCROFT ET AL., 2006; RYCROFT, 2007; RYCROFT, 2009) available in <http://math.lbl.gov/voro++/> preserving the volumetric proportion between grains. Three-node discontinuous triangular boundary elements are used to discretize the whole structure, in order to avoid shared nodes between more than two grains and to facilitate the multidomain implementation. As described in (FRITZEN ET AL., 2009), a 2D triangle mesh generator (SHEWCHUK, 1996), available in <https://www.cs.cmu.edu/~quake/triangle.html> is used over the flat faces of the grains. To guarantee the best mesh compatibility in the edges, the procedure established in (BENEDETTI AND

ALIABADI, 2013b) is implemented with a modest variation, and a hierarchical scheme is used for discretization. After the generation of the Voronoi tessellation, the edges are split to obtain the continuity. Due to the fact that faces are discretized independently, all 3D faces are converted into 2D faces to this end. Each grain is composed of faces that are formed by edges defined for two vertices, then the average length edge is defined as (\bar{L}_e) . Introducing a discretization density parameter (ρ_d), the current edge length (L_e) is split into a number of segments (n_s) as indicated by the following equation

$$n_s = \rho_d \left[\text{round} \left(\frac{L_e}{\bar{L}_e} + 1 \right) \right] , \quad (2.1)$$

where the $\text{round}(x)$ function expresses the rounded values close to x . The maximum triangle area constraint A_{max} used to enforce the regularity of the mesh is estimated as

$$A_{max} = \frac{1}{2} (\bar{L}_e)^2 , \quad (2.2)$$

which is the area of an isosceles triangle of sides of (\bar{L}_e) . Using some of the customized output references in (SHEWCHUK, 1996; RYCROFT, 2009), the format data are obtained creating some description matrices Figure 2.2 helps to understand the nomenclature employed in this work.

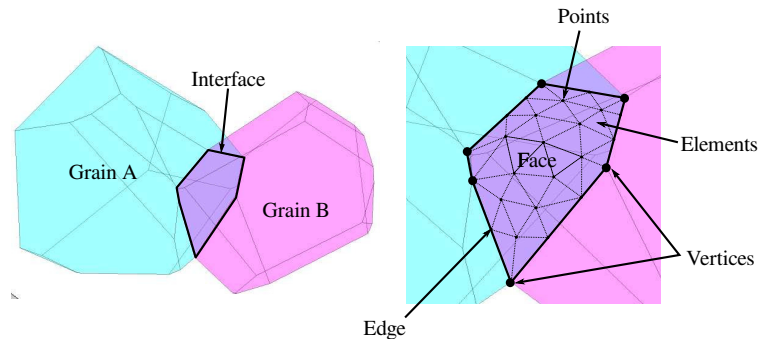


Figure 2.2: Mesh description.

The artificial solid is defined by the description connectivity matrices as e.g., FACES, VERTICES, NORMAL_VECTORS and VOLUMES in the first hierarchical level. These matrices are used as input of the second stage, a C algorithm to discretize all faces by transforming the 3D sur-

face into a 2D plane and then reversing the transformation. The triangle mesh is carried out using the command line switches (SHEWCHUK, 1996). Here, the description matrices of the second level as POINTS and ELEMENTS are generated, Figure 2.2. To avoid numerical errors of compatibility in the interface discretization stage, the algorithm discretizes one face as being an exact copy of the other face. Finally, an output file is exported to the main BEM application code with the minimum necessary connectivity information as e.g., FACES, ELEMENTS, POINTS, E_GRAIN (elements per grain), NORMAL_VECTORS and VOLUMES. A general scheme of this algorithm is presented in Figure 2.3, where the different stages are shown.

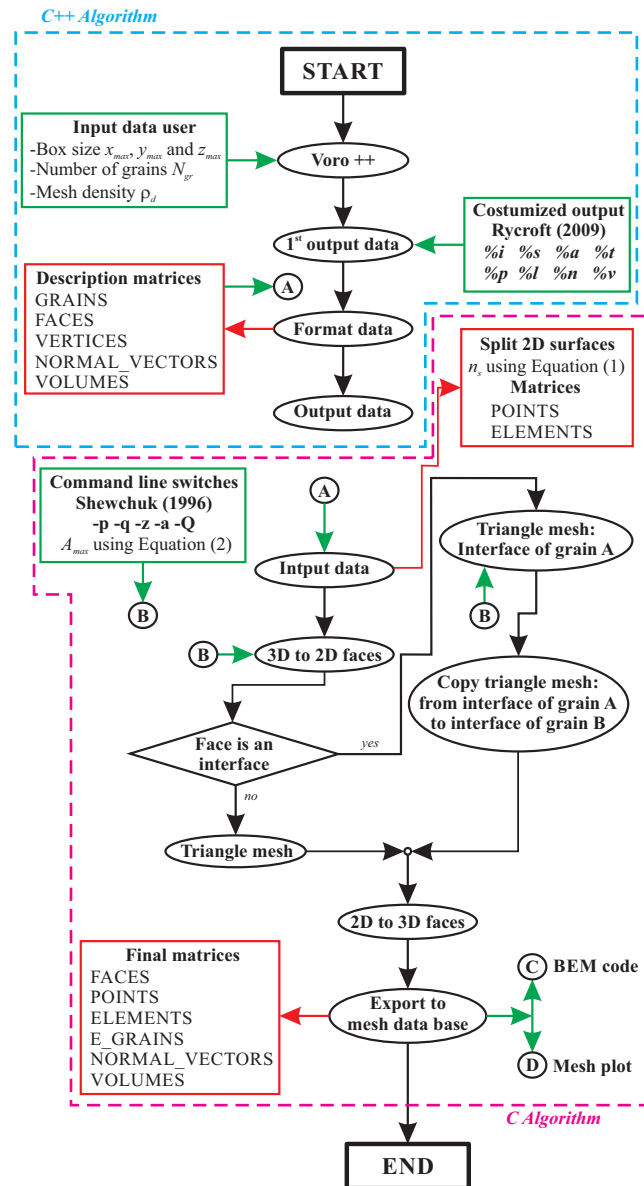


Figure 2.3: Multi-compiler algorithm C++/C of the mesh generator.

In Figure 2.3, at first stage, a C++ algorithm generates the polycrystalline structure, where the user sets the box size x_{max} , y_{max} and z_{max} , number of grains (N_{gr}) and mesh density ρ_d . Mesh results for different discretization levels, according to the parameter ρ_d , are given in Figure 2.4. In the case where $\rho_d = 1$, the structure has 15,186 elements. In the case where $\rho_d = 2$, the structure contains 44,082 elements.

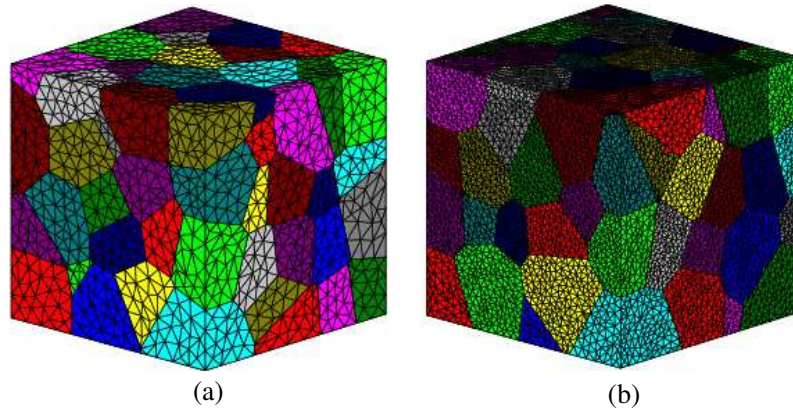


Figure 2.4: Polycrystalline structure of 100 grains: (a) $\rho_d = 1$ and (b) $\rho_d = 2$.

An acceptable compatibility is observable in the edges highlighting the difficulty to avoid all atypical grains in volume and surface sizes. In Figure 2.5, distribution of elements and volumes is presented.

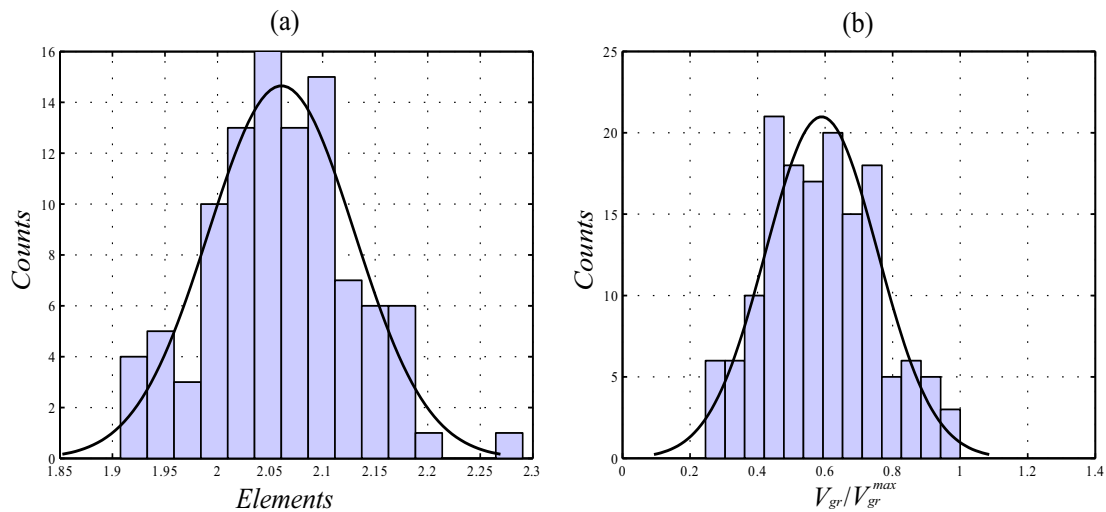


Figure 2.5: Polycrystalline structure of 150 grains using $\rho_d = 1$: (a) Elements of 100 generated structures and (b) normalized grain volumes V_{gr} of one Voronoi tessellation.

These cases show a trend to a mean value in the distribution for elements over 100 generated materials and volumes for a specific structure. Due to the large number of interfaces in the physical model, the matrix of interfaces is also generated in a parallel code, Figure 2.6. It consists in a simple way to compare the elements in the interfaces by its triangle coordinates.

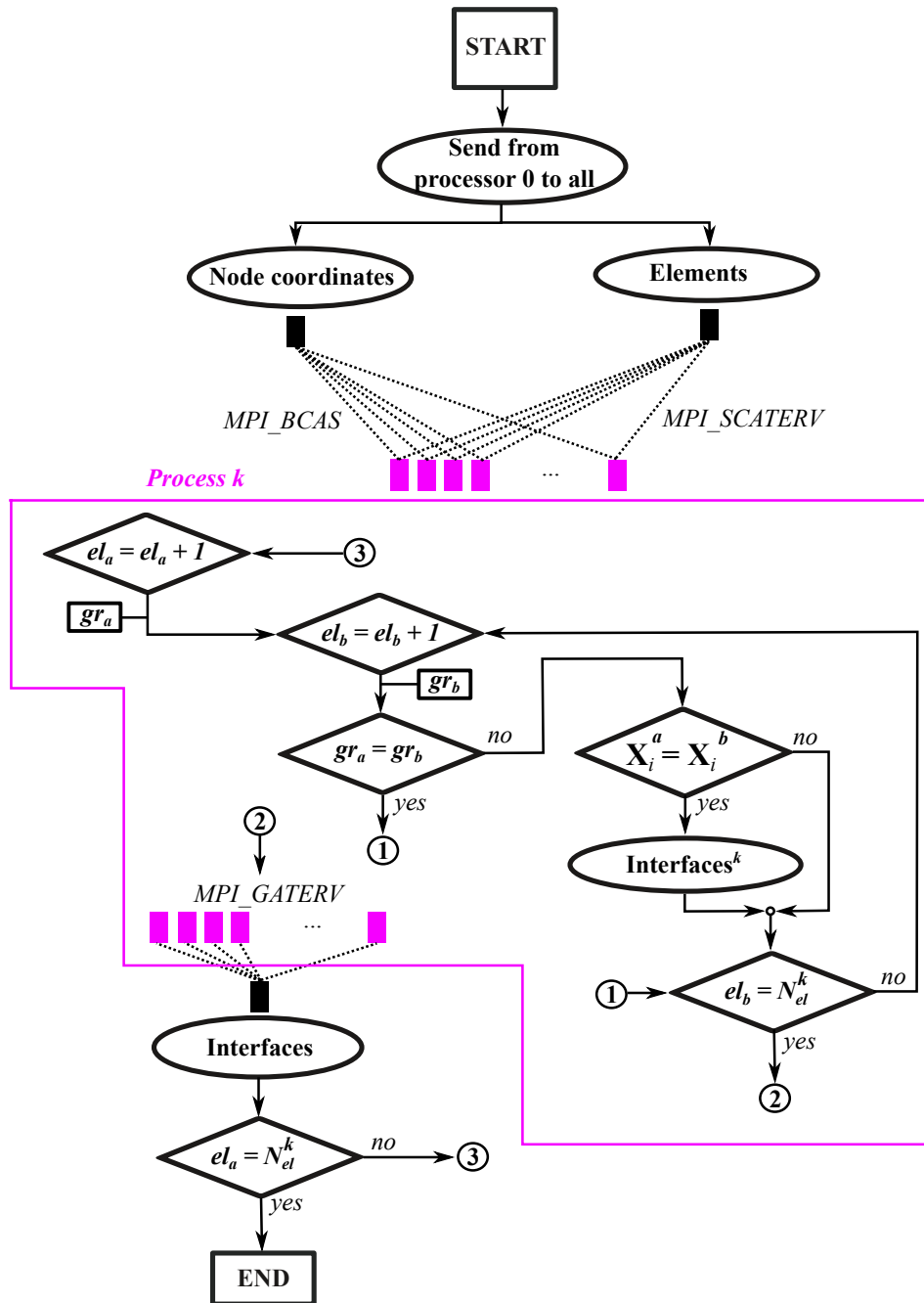


Figure 2.6: Parallel algorithm of interfaces.

In Figure 2.6, a and b refers to the number of the specific grain (gr) at the interface. The terms el_i and \mathbf{X}_i are the element and coordinates respectively. This algorithm leads to a drastic reduction of processing time to compute the matrix of interfaces when a considerable number of grains compose the polycrystalline aggregate. In order to test the performance of this algorithm, it is used a 216 grain structure with $\rho_d = 2$. In total it accounts with 232,046 boundary elements and 202,774 interfaces, results are shown in the following table

<i>Threads</i>	<i>Time [s]</i>
1	427.77
8	40.24
16	25.18
32	17.63
64	9.49
128	5.55

Table 2.1: Performance: algorithm of interfaces.

Table 2.1, shows the time reduction when the the number of threads increase. It represents an advantage for modeling large number of grains with high mesh refinement.

2.2 Constitutive model

Constitutive models of polycrystalline materials at microscale has been studied by many authors. It can be considered as a collection of grains that compose the aggregate, every grain is modeled as a linear elastic anisotropic body. From the atomistic scale, the lattice structure defines the anisotropy in the continuum grain model. The constitutive relation of stress-strain fields are represented by the stiffness tensor \mathbf{C} of 36 constants. Elastic constants of the stiffness tensor are dependent of the lattice structure of the material. Huntington (1958) and Tromans (2011) show the elastic constants for several materials with cubic and hexagonal systems, respectively. Cubic systems have three elastic constants in the stiffness tensor, while hexagonal systems have five. The representation is given by Equation (2.3) using the compact Voigt notation and reference system coordination.

$$\begin{array}{c}
\text{Cubic systems} \\
\left[\begin{array}{cccccc}
C_{11} & C_{12} & C_{12} & \bullet & \bullet & \bullet \\
C_{12} & C_{11} & C_{12} & \bullet & \bullet & \bullet \\
C_{12} & C_{12} & C_{11} & \bullet & \bullet & \bullet \\
\bullet & \bullet & \bullet & C_{44} & \bullet & \bullet \\
\bullet & \bullet & \bullet & \bullet & C_{44} & \bullet \\
\bullet & \bullet & \bullet & \bullet & \bullet & C_{44}
\end{array} \right]
\end{array}
\begin{array}{c}
\text{Hexagonal system} \\
\left[\begin{array}{cccccc}
C_{11} & C_{12} & C_{13} & \bullet & \bullet & \bullet \\
C_{12} & C_{11} & C_{13} & \bullet & \bullet & \bullet \\
C_{13} & C_{13} & C_{33} & \bullet & \bullet & \bullet \\
\bullet & \bullet & \bullet & C_{44} & \bullet & \bullet \\
\bullet & \bullet & \bullet & \bullet & C_{44} & \bullet \\
\bullet & \bullet & \bullet & \bullet & \bullet & C_{66}
\end{array} \right], \quad (2.3)
\end{array}$$

where $C_{66} = (C_{11} - C_{12})/2$. Random crystalline orientations are assigned to each grain uniformly distributed over the material based on the scheme given by Fritzen et al. (2009). Figure 2.7 shows an illustration to better explain this main idea.

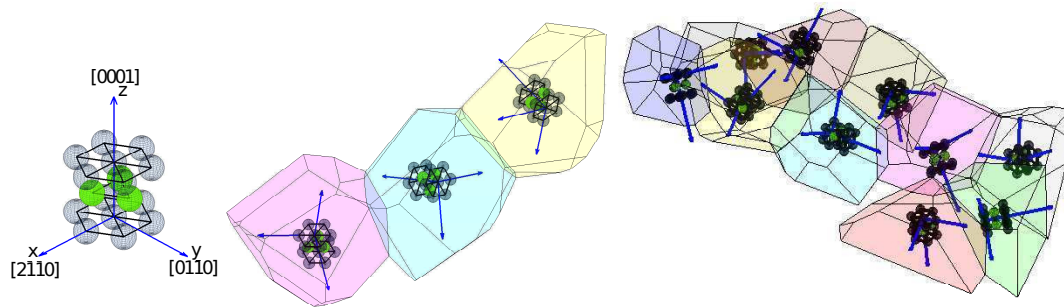


Figure 2.7: Distribution of crystalline orientation of lattice HCP structure.

Figure 2.7 shows a small sample of the distribution of random crystalline orientation depending on the lattice structure. A Fully populated stiffness tensor \mathbf{C}^* is obtained after the coordinate basis rotation. As suggested by Fritzen et al. (2009), the Euler angles are randomly generated from a uniform distribution following the $(z - x - z)$ convention. Thus a different stiffness tensor \mathbf{C} is obtained for each crystal orientation.

2.3 Anisotropic fundamental solution

The displacement fundamental solution is considered as the response in x_i direction at the field point \mathbf{x} owing to the perturbation produced by a unit load in the x_j direction at the source point \mathbf{x}' in a homogeneous infinite body. The analytical expression of the displacement fundamental solu-

tion or Green's function $U(\mathbf{x}', \mathbf{x})$ and its derivatives were first derived by Lifshitz and Rozenzweig (1947). Several efforts were made to produce an explicit form to evaluate $U(\mathbf{x}', \mathbf{x})$, and an explicit form to compute the Green's function was proposed by Ting and Lee (1997). The authors presented the Green's function in terms of the Barnett-Lothe tensor (SYNGE, 1957; BARNETT, 1972) $\mathbf{H}(\theta, \phi)$ as follows:

$$U(r, \theta, \phi) = \frac{1}{4\pi r} \mathbf{H}(\theta, \phi) \quad , \quad (2.4)$$

where, in the solution derived by Lifshitz and Rozenzweig (1947), $\mathbf{H}(\theta, \phi)$ is expressed as a contour integral around a unit circle as

$$\mathbf{H}(\theta, \phi) = \frac{1}{\pi} \int_0^{2\pi} \mathbf{Z}^{-1} d\psi \quad . \quad (2.5)$$

In Equation (2.4), r is the distance between the source point \mathbf{x}' located at the origin and the field point \mathbf{x} , and in Equation (2.5), \mathbf{Z}^{-1} is the inverse of \mathbf{Z} that depends on the stiffness tensor $\mathbf{C} \equiv C_{ijkl}$ (TING AND LEE, 1997). The Barnett-Lothe tensor $\mathbf{H}(\theta, \phi)$ depends only on the spherical angles (θ, ϕ) . For illustrative purposes, the contour integral around a unit circle $|\mathbf{n}^*|$ on a oblique plane at field point \mathbf{x} is shown in Figure 2.8.

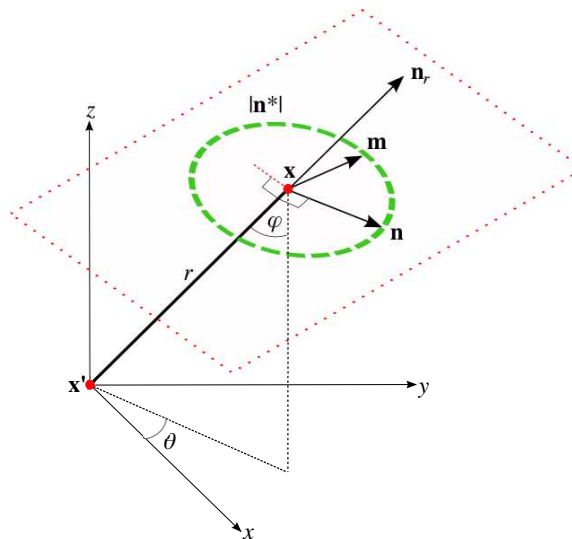


Figure 2.8: Integration scheme of Barnett-Lothe tensor.

The unit vector $|\mathbf{n}^*|$ on the oblique plane, the two mutually orthogonal vectors \mathbf{n} and \mathbf{m} are defined as

$$\begin{aligned} |\mathbf{n}^*| &= \mathbf{n} \cos \psi + \mathbf{m} \sin \psi \\ \mathbf{n} &= (\cos \phi \cos \theta, \cos \phi \sin \theta, -\sin \phi) \\ \mathbf{m} &= (-\sin \theta, \cos \theta, 0) \end{aligned} \quad \left\{ \begin{array}{l} \psi \text{ Arbitrary} \\ 0 \leq \theta < 2\pi \\ 0 \leq \phi \leq \pi \end{array} \right. . \quad (2.6)$$

The $[\mathbf{n}, \mathbf{m}, \mathbf{n}_r]$ form the right-handed triad, where $\mathbf{n}_r = \mathbf{x}/r$ and ψ is an arbitrary parameter. A more explicit way to evaluate the Barnett-Lothe tensor $\mathbf{H}(\theta, \phi)$ is expressed in terms of the Stroh's eigenvalues (TING AND LEE, 1997) as

$$\mathbf{H}(\theta, \phi) = \frac{1}{|\boldsymbol{\kappa}|} \sum_{n=0}^4 q_n \hat{\Gamma}^{(n)} . \quad (2.7)$$

Equation (2.7) is presented in detail in Appendix A.1. In the BEM formulation, the first approximation of displacement fundamental solution was presented by Wilson and Cruse (1978). They developed a technique to evaluate the anisotropic point load solutions and used a interpolation to obtain large databases of different anisotropic materials. Some schemes have developed for the efficient evaluation of the BEM fundamental solution. Shiah et al. (2012) proposed an alternative and accurate numerical scheme to compute these quantities, also Shiah and Tan (2011) and Tan et al. (2013) presented an elastic stress analysis using a BEM code. In this work, the evaluation of the fundamental solution was implemented using the scheme proposed by Tan et al. (2013). Due to the periodic characteristic of $\mathbf{H}(\theta, \phi)$, a representation in terms of double Fourier series around θ and ϕ gives

$$H_{uv}(\theta, \phi) = \sum_{m=-\alpha}^{\alpha} \sum_{n=-\alpha}^{\alpha} \lambda_{uv}^{(m,n)} e^{i(m\theta+n\phi)} \quad (u, v = 1, 2, 3) , \quad (2.8)$$

$$\lambda_{uv}^{(m,n)} = \frac{1}{4\pi^2} \int_{-\pi}^{\pi} \int_{-\pi}^{\pi} H_{uv}(\theta, \phi) e^{-i(m\theta+n\phi)} d\theta d\phi , \quad (2.9)$$

where $\lambda_{uv}^{(m,n)}$ are the Fourier coefficients, which can be numerically integrated by, e.g., Gaussian

quadrature. The k abscissa points, $\lambda_{uv}^{(m,n)}$, may be re-written as

$$\lambda_{uv}^{(m,n)} = \frac{1}{4} \sum_{p=1}^k \sum_{q=1}^k w_p w_q f_{uv}^{(m,n)}(\pi\xi_p, \pi\xi_q) \quad , \quad (2.10)$$

being w and ξ the weights and positions of the Gauss points, respectively, and $f_{uv}^{(m,n)}(\theta, \phi)$ represents the integrand of $\lambda_{uv}^{(m,n)}$. In short, substituting Equation (2.9) into the Equation (2.4), the fundamental displacement solution can also be written as

$$U_{uv}(r, \theta, \phi) = \frac{1}{4\pi r} \sum_{m=-\alpha}^{\alpha} \sum_{n=-\alpha}^{\alpha} \lambda_{uv}^{(m,n)} e^{i(m\theta+n\phi)} \quad (u, v = 1, 2, 3) \quad , \quad (2.11)$$

the α term is an integer number, large enough to yield the desired accuracy. Numerical experiments reported in (SHIAH ET AL., 2012) have shown that values of $k = 64$ and $\alpha = 16$ will be adequate to evaluate even the most highly anisotropic materials. The fundamental solution \mathbf{U} is expressed by

$$U_{uv}(r, \theta, \phi) = \frac{1}{2\pi r} \left\{ \begin{array}{l} \sum_{m=1}^{\alpha} \sum_{n=1}^{\alpha} \left[\begin{array}{l} (\tilde{R}_{uv}^{(m,n)} \cos m\theta - \tilde{I}_{uv}^{(m,n)} \sin m\theta) \cos n\phi \\ -(\hat{R}_{uv}^{(m,n)} \sin m\theta - \hat{I}_{uv}^{(m,n)} \cos m\theta) \sin n\phi \end{array} \right] \\ + \sum_{m=1}^{\alpha} \left(\begin{array}{l} R_{uv}^{(0,m)} \cos m\phi - I_{uv}^{(0,m)} \sin m\phi \\ +R_{uv}^{(m,0)} \cos m\theta - I_{uv}^{(m,0)} \sin m\theta \end{array} \right) + \frac{R_{uv}^{(0,0)}}{2} \end{array} \right\} . \quad (2.12)$$

A complete description of Equation (2.12) and its first order derivative \mathbf{U}' are presented in Appendix A.2. The traction fundamental solution T_{ij} can be evaluated by

$$T_{ij} = (\sigma_{ik} n_k)_j \quad , \quad (2.13)$$

where σ_{ik} is the fundamental solution of stresses and n_k is the outward normal vector on the surface at the field point. Using the generalized Hooke's law

$$(\sigma_{ik})_j = C_{ikmn}(U_{mj,n} + U_{nj,m})/2 \quad . \quad (2.14)$$

The most significant advantage of using this Fourier series representation of the Green's function and its derivatives is that Fourier series coefficients, $\lambda_{uv}^{(m,n)}$, are evaluated just one time for a given material, (TAN ET AL., 2013). Due to the constitutive model of polycrystalline materials, this application requires the evaluation of the Fourier coefficients for each grain with specific crystalline orientation. This fact makes necessary the evaluation of the Fourier coefficients in an auxiliary code implemented in a serial algorithm using Fortran 90. For each crystalline orientation, the evaluation of these coefficients requires approximately 20 ~ 23 seconds, the procedure of calculation of $\lambda_{uv}^{(m,n)}$ is shown in Figure 2.9.

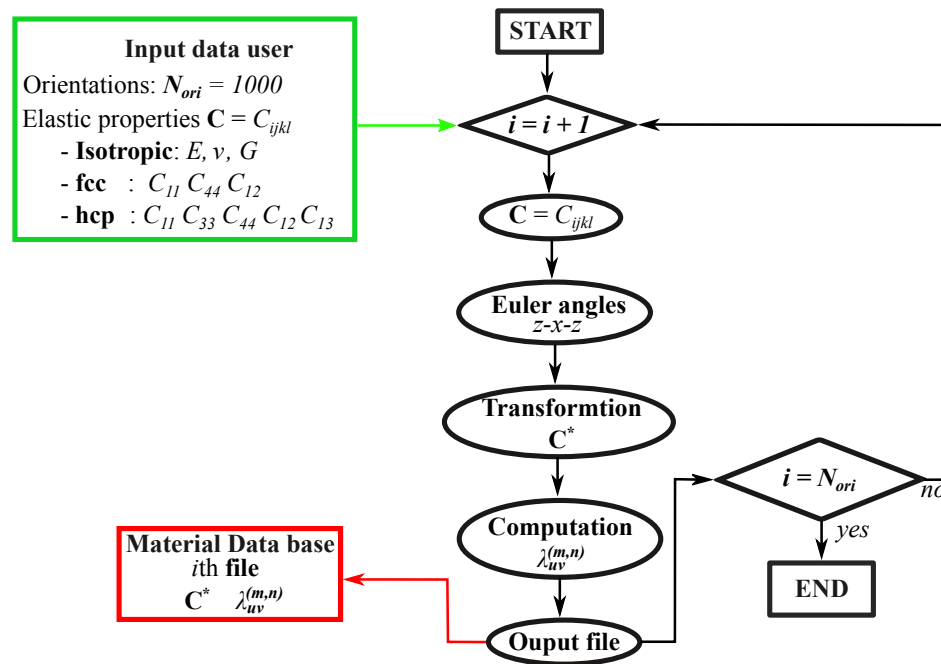


Figure 2.9: Algorithm: database of Fourier coefficients $\lambda_{uv}^{(m,n)}$ for a specific material.

For this application, a database of 1,000 crystalline orientations (N_{ori}) is created for each specific material. Therefore, this implementation offers a more efficient computational effort and simulation time in the main BEM code.

3 Elastodynamic BEM formulation

The BEM formulation permits to model high gradients of different mechanical fields only using the surface information. The surface discretization leads to a reduction in the number of DOF used in the model. Depending on the application, a fundamental solution is required by the BEM. In the modeling of isotropic and general anisotropic solids, the displacement fundamental solution based on double Fourier series proposed by Tan et al. (2013) is implemented. The BEM represents a useful numerical tool for modeling polycrystalline materials only using the surface grain boundaries. Thus, in case of different constitutive domains, the multidomain algorithm needs to be implemented. To model the dynamic effects, the response of the displacement field will be obtained in the time domain. In order to develop this dynamic analysis, it is necessary the transformation of the domain integral into a boundary integral applying the DRBEM formulation. Also Dirichlet and Neumann boundary conditions can be applied to the model.

3.1 Integral formulation

The boundary integral equation expresses the relation of the displacement u_i and traction t_i on a surface Γ using the known fundamental solution for displacement $U_{ik}(\mathbf{x}', \mathbf{x})$ and traction $T_{ik}(\mathbf{x}', \mathbf{x})$. For homogeneous elastic body, the boundary integral equation considering the body forces on the domain Ω is given by

$$c_{ik}(\mathbf{x}')u_i(\mathbf{x}') + \int_{\Gamma} T_{ik}(\mathbf{x}', \mathbf{x})u_i(\mathbf{x}) d\Gamma = \int_{\Gamma} U_{ik}(\mathbf{x}', \mathbf{x})t_i(\mathbf{x}) d\Gamma + \int_{\Omega} \rho \ddot{u}_i U_{ik}(\mathbf{x}', \mathbf{x}) d\Omega \quad , \quad (3.1)$$

where (\mathbf{x}') and (\mathbf{x}) are the source and field points respectively, $c_{ik}(\mathbf{x}')$ is $\delta_{ik}/2$ for a smooth surface boundary at source point and ρ is the mass density. For transient analysis, the body forces are caused by the acceleration field \ddot{u}_i . In the Equation (3.1), the fourth domain integral considers the terms of the dynamic effects due to its body acceleration. Thus, in order to apply the BEM formulation, it is required the transformation of this domain integral into a boundary or surface integral. In this work, the DRBEM is implemented to pursue this transformation. Moreover, other numerical approximation such as the RIM proposed by Gao (2002) can be used to this end. After some nu-

merical experiments, Rodriguez (2016) made comparisons between DRBEM and RIM. His results showed that, using a coarse discretization, the RIM offers more accurate results than the DRBEM using a finer discretization. However, the RIM demands a high computational requirements in its implementation. The acceleration field of the domain integral in Equation (3.1) can be represented by

$$\rho \ddot{u}_i = \sum_{j=1}^M f_{mk}^j(x) \alpha_m^j \quad , \quad (3.2)$$

where α_m^j are unknown coefficients and f_{mk}^j are M radial functions that have to fulfil the equilibrium equation, in the D'Alembert sense

$$C_{mnr s} \hat{u}_{rk,ns} = f_{mk}^j \quad . \quad (3.3)$$

The term \hat{u}_{rk} is the particular solution to solve Equation (3.3). Substituting Equation (3.2) into the fourth integral of Equation (3.1) gives

$$\int_{\Omega} \rho \ddot{u}_i U_{ik} d\Omega = \sum_{j=1}^M \alpha_n^j \int_{\Omega} U_{ik} f_{kn}^j d\Omega \quad . \quad (3.4)$$

The reciprocal integral relation can also be obtained between the fundamental solution and the particular solution as

$$c_{ik} \hat{u}_{kn}^j + \int_{\Gamma} T_{ik} \hat{u}_{kn}^j d\Gamma = \int_{\Gamma} U_{ik} \hat{t}_{kn}^j d\Gamma + \int_{\Omega} U_{ik} f_{kn}^j d\Omega \quad , \quad (3.5)$$

by substituting Equation (3.5) into Equation (3.4) and then into Equation (3.1), the integral equation results in

$$c_{ik}u_i + \int_{\Gamma} T_{ik}u_i d\Gamma = \int_{\Gamma} U_{ik}t_i d\Gamma + \sum_{j=1}^M \alpha_n^j \left\{ c_{ik}\hat{u}_{kn}^j - \int_{\Gamma} U_{ik}\hat{t}_{kn}^j d\Gamma + \int_{\Gamma} T_{ik}\hat{u}_{kn}^j d\Gamma \right\} , \quad (3.6)$$

where the particular solution \hat{u}_{in}^m is a radial function (KÖGL AND GAUL, 2000a) expressed as

$$\hat{u}_{rk} = \delta_{kn}(r^2 + r^3) , \quad (3.7)$$

and its derivatives

$$\begin{aligned} \hat{u}_{rk,l} &= \delta_{rk}(2r + 3r^2)r_{,l} , \\ \hat{u}_{rk,lj} &= \delta_{rk}((2 + 3r)\delta_{lj} + 3rr_{,j}r_{,l}) . \end{aligned} \quad (3.8)$$

The particular solution \hat{t}_{rk}^j can be evaluated using the Equation (3.7) into the Equation (2.14).

3.2 Discretization

The Equation (3.6) must be discretized into surface elements, different type of elements can be used such as quadrilateral or triangular, each of them can be implemented usually as linear or quadratic (KANE, 1994). In this work, linear three-node discontinuous triangular boundary elements are used. The main reasons to use this type of boundary element are: (i) the facility in the implementation of the mesh generator described in section 2.1, (ii) linear elements represent a drastic reduction in the DOF and the computational cost required by the numerical integration. Finally, (iii) discontinuous elements offer advantages in the implementation of the multidomain algorithm. Due to the nature of this application, there are no nodes shared by more than two grains of the polycrystal aggregate. Rewriting the Equation (3.6) the overall polycrystalline materials is represented by

$$\begin{aligned}
c_{ik}^g u_i^g + \int_{\Gamma^g} T_{ik} u_i \, d\Gamma^g &= \int_{\Gamma^g} U_{ik} t_i \, d\Gamma^g \\
+ \sum_{j=1}^M \alpha_n^{j,g} \left(c_{ik}^g \hat{u}_{kn}^{j,g} + \int_{\Gamma^g} T_{ik} \hat{u}_{kn}^j \, d\Gamma^g - \int_{\Gamma^g} U_{ik} \hat{t}_{kn}^j \, d\Gamma^g \right) , & \quad (3.9)
\end{aligned}$$

where the superscript g represent the g th grain. The linear three-node discontinuous element is shown in Figure 3.1, the three nodes are function of the two intrinsic parametric coordinates (η, ξ) . Thus, the position of all nodes in the element is controlled by the parametric distance λ .

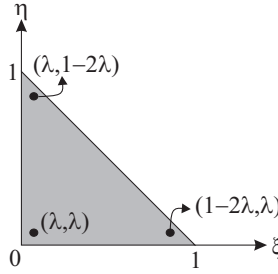


Figure 3.1: Linear three-node discontinuous element.

The surface response is interpolated within an element from the nodal values, using shape functions $h^{(1)}$ $h^{(2)}$ $h^{(3)}$ corresponding to the nodes 1, 2 and 3 respectively. The interpolated field X expressed in terms of the known nodal values $X^{(k)}$ are

$$X(\xi, \eta) = \sum_{k=1}^3 h^{(k)}(\xi, \eta) X^{(k)} \quad . \quad (3.10)$$

The first derivative of the interpolated field, in terms of the shape functions can be written as

$$\begin{aligned}
\frac{\partial X(\xi, \eta)}{\partial \xi} &= \sum_{k=1}^3 \frac{\partial h^{(k)}(\xi, \eta)}{\partial \xi} X^{(k)} \quad , \\
\frac{\partial X(\xi, \eta)}{\partial \eta} &= \sum_{k=1}^3 \frac{\partial h^{(k)}(\xi, \eta)}{\partial \eta} X^{(k)} \quad .
\end{aligned} \quad (3.11)$$

The detailed procedure to obtain the three shape functions and its derivatives in a numerical

way are exposed in Appendix B.1, also the formulation to evaluate the Jacobian and the normal vector is shown. Therefore, Equation (3.9) in terms of grains can be discretized into linear three-node discontinuous triangular elements. Rewriting Equation (3.9) gives

$$c_{ik}^g u_i^g + \sum_{\epsilon=1}^{N_\epsilon^g} \int_{\Gamma_\epsilon^g} T_{ik} \left(\sum_{n=1}^{N_n^c} h^n u_i^n \right) d\Gamma_\epsilon^g = \sum_{\epsilon=1}^{N_\epsilon^g} \int_{\Gamma_\epsilon^g} U_{ik} \left(\sum_{n=1}^{N_n^c} h^n t_i^n \right) d\Gamma_\epsilon^g + \sum_{j=1}^M \alpha_n^{j,g} \left(c_{ik}^g \hat{u}_{kn}^{j,g} + \sum_{\epsilon=1}^{N_\epsilon^g} \int_{\Gamma_\epsilon^g} T_{ik} \hat{u}_{kn}^j d\Gamma_\epsilon^g - \sum_{\epsilon=1}^{N_\epsilon^g} \int_{\Gamma_\epsilon^g} U_{ik} \hat{t}_{kn}^j d\Gamma_\epsilon^g \right) . \quad (3.12)$$

In Equation (3.12), the g th grain is divided by the elements ϵ and the nodes n in the element. The integration of the Equation (3.12) is carried out by the numerical Gauss integration, for triangles following the procedures presented by Kane (1994). Thus, the Equation (3.12) can be expressed as

$$c_{ik}^g u_i^g + \sum_{\epsilon=1}^{N_\epsilon^g} \left(\sum_{n=1}^{N_n^c} \int_0^1 \int_0^{1-\eta} T_{ik} h^n J d\xi d\eta \right) u_i^n = \sum_{\epsilon=1}^{N_\epsilon^g} \left(\sum_{n=1}^{N_n^c} \int_0^1 \int_0^{1-\eta} U_{ik} h^n J d\xi d\eta \right) t_i^n + \sum_{j=1}^M \alpha_n^{j,g} \left[c_{ik}^g \hat{u}_{kn}^{j,g} + \sum_{\epsilon=1}^{N_\epsilon^g} \left(\sum_{n=1}^{N_n^c} \int_0^1 \int_0^{1-\eta} T_{ik} h^n J d\xi d\eta \right) \hat{u}_{kn}^j - \sum_{\epsilon=1}^{N_\epsilon^g} \left(\sum_{n=1}^{N_n^c} \int_0^1 \int_0^{1-\eta} U_{ik} h^n J d\xi d\eta \right) \hat{t}_{kn}^j \right] , \quad (3.13)$$

where the integration for the traction fundamental solution is defined as

$$c_{ik}^g + \sum_{\epsilon=1}^{N_\epsilon^g} \left(\sum_{n=1}^{N_n^c} \int_0^1 \int_0^{1-\eta} T_{ik} h^n J d\xi d\eta \right) = \mathbf{H}^g , \quad (3.14)$$

and the integration of the displacement fundamental solution is

$$\sum_{\epsilon=1}^{N_\epsilon^g} \left(\sum_{n=1}^{N_n^c} \int_0^1 \int_0^{1-\eta} U_{ik} h^n J d\xi d\eta \right) = \mathbf{G}^g . \quad (3.15)$$

Rewriting Equation (3.13) in the matrix form for the g th grain

$$\mathbf{H}^g \mathbf{u}^g = \mathbf{G}^g \mathbf{u}^g + \sum_{j=1}^M \alpha^{j,g} (\mathbf{H}^g \hat{\mathbf{u}}^{j,g} - \mathbf{G}^g \hat{\mathbf{t}}^{j,g}) . \quad (3.16)$$

The summation in Equation (3.16), is over the total number of nodes M of the physical problem. Then, the final equation in the matrix form for the g th grain is

$$\mathbf{H}^g \mathbf{u}^g = \mathbf{G}^g \mathbf{t}^g + (\mathbf{H}^g \hat{\mathbf{U}}^g - \mathbf{G}^g \hat{\mathbf{T}}^g) \boldsymbol{\alpha}^g . \quad (3.17)$$

From Equation (3.2) in its matrix form, the term $\boldsymbol{\alpha}$ can be expressed as

$$\boldsymbol{\alpha}^g = \rho \mathbf{E}^g \ddot{\mathbf{u}}^g , \quad (3.18)$$

where \mathbf{E}^g is the inverse of the matrix \mathbf{F}^g , the matrix \mathbf{F}^g contains all the components of f_{mk}^j . Substituting the Equation (3.18) into Equation (3.17)

$$\mathbf{H}^g \mathbf{u}^g = \mathbf{G}^g \mathbf{t}^g + \rho (\mathbf{H}^g \hat{\mathbf{U}}^g - \mathbf{G}^g \hat{\mathbf{T}}^g) \mathbf{E}^g \ddot{\mathbf{u}}^g . \quad (3.19)$$

In this formulation, the mass matrix can be defined as $\mathbf{M}^g = \rho (\mathbf{G}^g \hat{\mathbf{T}}^g - \mathbf{H}^g \hat{\mathbf{U}}^g) \mathbf{E}^g$, the final form of Equation (3.19) is

$$\mathbf{M}^g \ddot{\mathbf{u}}^g + \mathbf{H}^g \mathbf{u}^g = \mathbf{G}^g \mathbf{t}^g . \quad (3.20)$$

At this point, the formulation considers the inertial effects of the body caused by its own acceleration. Moreover, body forces can be added to the right-hand termed in Equation (3.20). Due to the large number of Fourier coefficients and the Gauss integration, this section requires a lot of processing time. A parallelized algorithm is shown in Figure 3.2, where each grain matrices \mathbf{H}^g ,

For each grain, all elements and coordinates are distributed to the processors (k), using an adequate balance load for each processor in order to guarantee an homogeneous processing. Inside each processor, the integration is carried out between the source points (sp), the source elements (se) and the field elements (fe). In order to test the performance of this algorithm, it is used a 216 grain structure with $\rho_d = 2$. For this analysis, it is considered only one grain with 882 boundary elements, results are shown in the following table

<i>Threads</i>	<i>Time [s]</i>
1	3880.01
8	652.46
16	392.01
32	268.69
64	162.21
128	103.73

Table 3.1: Performance: algorithm of matrices.

Table 3.1, shows the time reduction for computing matrices \mathbf{H}^g and \mathbf{G}^g when the number of threads increase. It represents an advantage for modeling structures with high mesh refinement. The matrix \mathbf{M}^g requires the inversion of \mathbf{F}^g , for that reason it was not included in the performance analysis.

3.3 Time domain integration

A transient dynamic analysis of 3D polycrystalline materials is proposed. Thus, it is required the time-domain integration of Equation (3.20). The Houbolt's algorithm (HOUBOLT, 1950) is an implicit appropriate method to be used coupled to the DRBEM (DOMINGUEZ, 1993; ALBUQUERQUE ET AL., 2002). The time-dependent solution of Equation (3.20) is obtained at every instant $\tau + \Delta\tau$. Therefore, the acceleration of the body can be expressed as

$$\ddot{\mathbf{u}}_{\tau+\Delta\tau}^g = \frac{1}{\Delta\tau^2} (2\mathbf{u}_{\tau+\Delta\tau}^g - 5\mathbf{u}_{\tau}^g + 4\mathbf{u}_{\tau-\Delta\tau}^g - \mathbf{u}_{\tau-2\Delta\tau}^g) \quad . \quad (3.21)$$

The matrix Equation (3.20) at instant $\tau + \Delta\tau$ is

$$\mathbf{M}^g \ddot{\mathbf{u}}_{\tau+\Delta\tau}^g + \mathbf{H}^g \mathbf{u}_{\tau+\Delta\tau}^g = \mathbf{G}^g \mathbf{t}_{\tau+\Delta\tau}^g \quad . \quad (3.22)$$

The substitution of the Equation (3.21) into Equation (3.22) leads to Equation (3.23), which is the response at instant $\tau + \Delta\tau$ using the information of the last three time steps

$$\left[\frac{2}{\Delta\tau^2} \mathbf{M}^g + \mathbf{H}^g \right] \mathbf{u}_{\tau+\Delta\tau}^g = \mathbf{G}^g \mathbf{t}_{\tau+\Delta\tau}^g + \frac{1}{\Delta\tau^2} \mathbf{M}^g (5\mathbf{u}_{\tau}^g - 4\mathbf{u}_{\tau-\Delta\tau}^g + \mathbf{u}_{\tau-2\Delta\tau}^g) \quad . \quad (3.23)$$

In Equation (3.23), vectors $\mathbf{u}_{\tau+\Delta\tau}^g$ and $\mathbf{t}_{\tau+\Delta\tau}^g$ are the displacement and traction fields of the g th grain in the instant $\tau + \Delta\tau$, respectively. Due to the nature of the material, the multidomain formulation of BEM is implemented to a domain divided into grains.

3.4 Multidomain assembly

Polycrystalline aggregates require a multidomain assembly, where the boundary conditions imposed in the external grains and the displacement compatibility and traction equilibrium must be applied in the interfaces, as shown in the following equation.

$$\begin{aligned} \mathbf{u}_i^j &= \mathbf{u}_j^i \quad , \\ \mathbf{t}_i^j &= -\mathbf{t}_j^i \quad . \end{aligned} \quad (3.24)$$

where the i and j indices represent the i th and j th grains. Figure 3.3 shows an interface between two grains, Γ_i and Γ_j relates the grain surfaces, Ω_i and Ω_j are the domains and $\bar{\mathbf{n}}$ represents the outward normal vector.

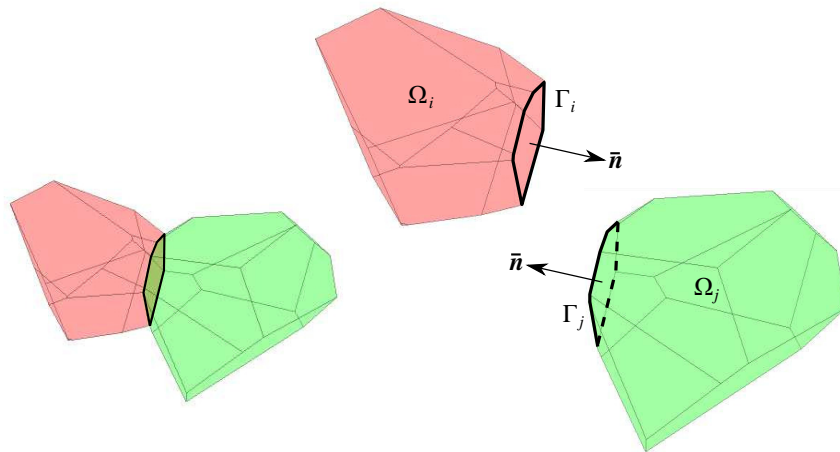


Figure 3.3: Interfaces.

The multidomain algorithm divides the matrices into blocks. The first correspond to the elements where the boundary conditions are applied in the external surfaces defines as

$$\mathbf{A}^g = \left[\frac{2}{\Delta\tau^2} \mathbf{M}^g + \mathbf{H}_{bc}^g \right] , \quad (3.25)$$

$$\mathbf{B}^g = \mathbf{G}_{bc}^g .$$

where \mathbf{H}_{bc}^g and \mathbf{G}_{bc}^g are the blocks after the exchange columns when known displacement boundary conditions are imposed. For the internal elements that belong to the interfaces, the matrix is

$$\mathbf{F}^g = \left[\frac{2}{\Delta\tau^2} \mathbf{M}^g + \mathbf{H}_I^g \right] , \quad (3.26)$$

and

$$\mathbf{u}_\alpha = \frac{1}{\Delta\tau^2} (5\mathbf{u}_\tau - 4\mathbf{u}_{\tau-\Delta\tau} + \mathbf{u}_{\tau-2\Delta\tau}) . \quad (3.27)$$

For this illustrative case of two grains, Figure 3.3, the final system of equation after the

application of the boundary conditions is

$$\begin{aligned}
 \begin{bmatrix} \mathbf{A}_i & \mathbf{F}_i^j & -\mathbf{G}_i^j & 0 \\ 0 & \mathbf{F}_j^i & \mathbf{G}_j^i & \mathbf{A}_j \end{bmatrix} \begin{Bmatrix} \mathbf{x}_i \\ \mathbf{u}_i^j \\ \mathbf{t}_i^j \\ \mathbf{x}_j \end{Bmatrix}_{\tau+\Delta\tau} &= \begin{bmatrix} \mathbf{B}_i & 0 & 0 & 0 \\ 0 & 0 & 0 & \mathbf{B}_j \end{bmatrix} \begin{Bmatrix} \mathbf{k}_i^{bc} \\ 0 \\ 0 \\ \mathbf{k}_j^{bc} \end{Bmatrix}_{\tau+\Delta\tau} + \\
 &+ \begin{bmatrix} \mathbf{M}_i & \mathbf{M}_i^j & 0 & 0 \\ 0 & \mathbf{M}_j^i & 0 & \mathbf{M}_j \end{bmatrix} \begin{Bmatrix} \mathbf{u}_{\alpha i} \\ \mathbf{u}_{\alpha i}^j \\ 0 \\ \mathbf{u}_{\alpha j} \end{Bmatrix}, \tag{3.28}
 \end{aligned}$$

where \mathbf{A}_i , \mathbf{B}_i and \mathbf{M}_i belong to the boundary of the polycrystalline aggregate; \mathbf{A}_i and \mathbf{B}_i are the blocks corresponding to \mathbf{H}_i and \mathbf{G}_i where the load conditions are applied. The blocks \mathbf{F}_i^j and \mathbf{G}_i^j are the interfaces between i th and j th grains. Vectors \mathbf{x}_i represent all the traction and displacements unknowns to be evaluated in the elements corresponding to the boundaries and the vectors \mathbf{k}_i^{bc} are the known boundary conditions applied respectively. In the interfaces, displacement \mathbf{u}_i^j and traction \mathbf{t}_i^j are evaluated. The last three step displacement responses are defined by $\mathbf{u}_{\alpha i}$, where $\mathbf{u}_{\alpha j}$ is for blocks belonging to the boundaries and $\mathbf{u}_{\alpha i}^j$ for blocks in the interfaces. A general algorithm to assemble the system of equation in multidomain applications can be found in (KANE, 1994; KATSIKADELIS, 2002). For this application, the final three block matrices and vectors in Equation (3.28) are highly sparse due to the incidence between grains. Thus, in order to improve the implementation in terms of memory and processing cost, it is necessary to treat all operations as sparse. The final matrix equation is

$$\mathcal{A}\mathbf{x}_{\tau+\Delta\tau} = \mathcal{B}\mathbf{k}_{\tau+\Delta\tau}^{bc} + \mathcal{M}\mathbf{u}_{\alpha} \quad . \tag{3.29}$$

When elastostatic problems are treated, the mass terms are void and the system becomes time-independent, or

$$\begin{bmatrix} \mathbf{F}_i & \mathbf{H}_i^j & -\mathbf{G}_i^j & 0 \\ 0 & \mathbf{H}_j^i & \mathbf{G}_j^i & \mathbf{F}_j \end{bmatrix} \begin{Bmatrix} \mathbf{x}_i \\ \mathbf{u}_i^j \\ \mathbf{t}_i^j \\ \mathbf{x}_j \end{Bmatrix} = \begin{bmatrix} \mathbf{B}_i & 0 & 0 & 0 \\ 0 & 0 & 0 & \mathbf{B}_j \end{bmatrix} \begin{Bmatrix} \mathbf{k}_i^{bc} \\ 0 \\ 0 \\ \mathbf{k}_j^{bc} \end{Bmatrix} . \quad (3.30)$$

In this case $\mathbf{F}^g = \mathbf{H}_{bc}^g$ and $\mathbf{B}^g = \mathbf{G}_{bc}^g$. The remaining blocks belong to the elements in the interfaces. The final general matrix equation for elastostatic problems is

$$\mathcal{A}\mathbf{x} = \mathcal{B}\mathbf{k}^{bc} . \quad (3.31)$$

In order to solve the large sparse system of equations, a Multifrontal Massively Parallel Sparse (MUMPS) (AMESTOY ET AL., 2001; AMESTOY ET AL., 2006) direct solver is used. The code and user's guide are available in <http://mumps.enseeiht.fr/>. MUMPS implements a direct method based on a multifrontal approach, which performs a Gaussian factorization. This solver is configured for general unsymmetrical real matrices using the out of core option.

4 Dynamic behavior of polycrystalline materials

The microscale dynamic behavior of 3D polycrystalline materials with different lattice structures is presented. In addition, this analysis serves as validation of the constitutive modeling and the BEM formulation presented. The absence of analytical solutions of these stochastic materials has been a challenge in validating numerical results under dynamic boundary conditions. In the macroscale analysis, these materials present an effective isotropic nature, when the number of crystal aggregates in the microscale is large. Therefore, the macroscopic effective Young's and shear moduli are evaluated using the average homogenization technique and compared with reference values. For this case, examples are presented showing the convergence to isotropic media. A computational framework is proposed to validate the dynamic behavior of polycrystalline materials, using the effective macroscopic properties assessed on the available analytical dynamic isotropic models. Numerical results applying several dynamic loads are presented, including the resonance condition. Finally, all results are treated through statistical analysis for a large number of simulations.

4.1 Effective macroscopic properties

The random distribution of crystalline orientations and the geometrical morphology in the polycrystal aggregate are significant in the evaluation of the overall macroscopic isotropic behavior. Average homogenization technique is used to obtain the effective elastic properties of polycrystals with cubic and hexagonal lattice systems. Mechanical properties in the analysis of microheterogeneous materials are characterized by the elasticity tensor \mathbf{C} . Then, in order to represent the homogenized effective macroscopic tensor $\bar{\mathbf{C}}$ of such materials (ZOHDI AND WRIGGERS, 2005), the Hooke's law relation between the averages fields have to be used. It is given by

$$\langle \bar{\boldsymbol{\sigma}} \rangle = \bar{\mathbf{C}} : \langle \bar{\boldsymbol{\varepsilon}} \rangle \quad , \quad (4.1)$$

where " $\langle \cdot \rangle$ " indicates the homogenization of a field, $\langle \bar{\boldsymbol{\sigma}} \rangle$ is the homogenized effective Cauchy stress tensor, $\langle \bar{\boldsymbol{\varepsilon}} \rangle$ represents the effective homogenized strain tensor. The stiffness tensor can take the form shown in Equation (2.3). Computational procedures have been described in the literature to evaluate the effective $\bar{\mathbf{C}}$ and apparent $\hat{\mathbf{C}}$ stiffness tensor of elastic properties (ZOHDI AND

WRIGGERS, 2005; OSTOJA-STARZEWSKI, 2006; FRITZEN ET AL., 2009; BENEDETTI AND ALIABADI, 2013B). In the present work, a set of six kinematic boundary conditions as linear displacements are applied, Figure 4.1.

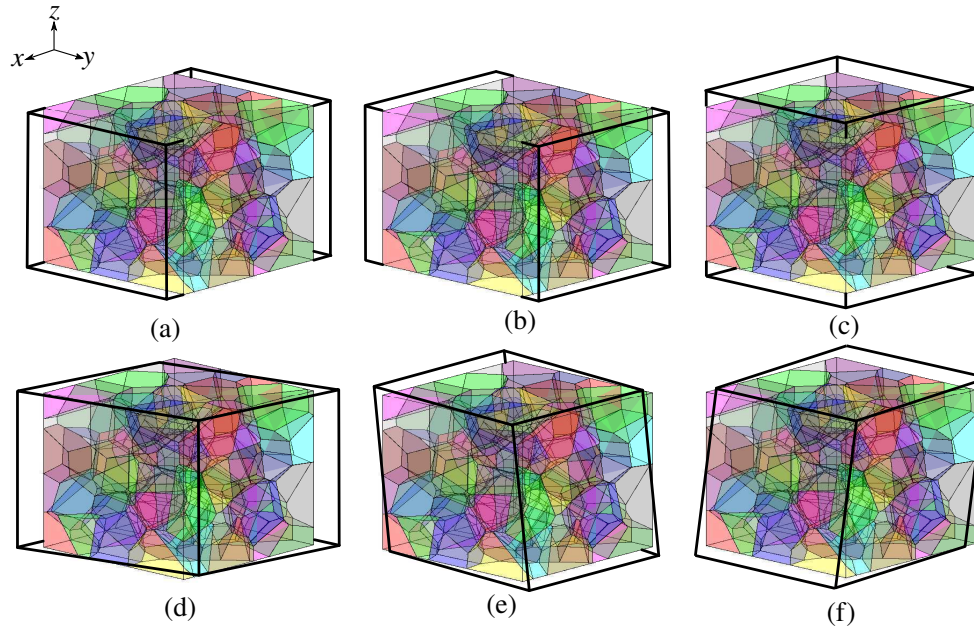


Figure 4.1: Kinematic boundary conditions: (a) ε_x , (b) ε_y , (c) ε_z , (d) ε_{xy} , (e) ε_{yz} and (f) ε_{xz} .

The six tests shown in Figure 4.1, represent one realization in the statistical analysis. The homogenized stress and strain tensors are evaluated in the surface Γ after the application of the divergence theorem (HILL, 1963). The expression for the stress field is

$$\langle \hat{\sigma}_{ij} \rangle = \frac{1}{|\Omega|} \int_{\Omega} \sigma_{ij} \, d\Omega = \frac{1}{2|\Omega|} \int_{\Gamma} (t_i x_j + t_j x_i) \, d\Gamma \quad , \quad (4.2)$$

and for the strain field gives

$$\langle \hat{\varepsilon}_{ij} \rangle = \frac{1}{|\Omega|} \int_{\Omega} \varepsilon_{ij} \, d\Omega = \frac{1}{2|\Omega|} \int_{\Gamma} (n_i u_j + n_j u_i) \, d\Gamma \quad . \quad (4.3)$$

where, $|\Omega|$ is the volume of the representative volume element (RVE), u_i and t_i are the nodal response of displacement and traction, respectively. The n_i term is the normal outward vector and

x_i is the coordinate of the deformed position of the surface Γ . These two homogenized fields are easily evaluated due to the displacement and traction fields directly obtained from the BEM on the surface (BENEDETTI AND ALIABADI, 2013b). The apparent stiffness tensor can be evaluated by

$$\langle \hat{\sigma} \rangle = \hat{\mathbf{C}} : \langle \hat{\varepsilon} \rangle \quad . \quad (4.4)$$

The tensor $\hat{\mathbf{C}}$ has 36 unknowns, then, the final system of equations composed by the contribution of each boundary condition shown in Figure 4.1 gives 36 equations for each realization. In polycrystalline materials, the macrodomain effective stiffness $\bar{\mathbf{C}}$ are estimated by a statistical analysis as the mean value of a set of variety number of simulation tests. Two materials are analyzed, copper (Cu) fcc and zinc (Zn) hcp, the properties of these materials at the microscale are presented in Table 4.1.

	C_{11}	C_{33}	C_{44}	C_{12}	C_{13}
Zn	165	61.8	39.6	31.1	50
Cu	168.4		75.4	121.4	

Table 4.1: Anisotropic elastic constants for Zn (TROMANS, 2011) and Cu (HUNTINGTON, 1958) in [GPa].

Six specimens with 18, 36, 60, 100, 150 and 210 number of grains are considered, each of them with 100 aggregate structures. Thus, a total of 600 different polycrystals and 1200 virtual materials are used in the simulations. A random distribution of crystalline orientation is also used from a database that contains 1000 orientations. The number of DOF for each number of grains of each RVE is given in Table 4.2.

N_{gr}	18	36	60	100	150	210
$N_{DOF_{min}}$	12,645	31,662	59,715	108,630	171,684	250,938
$N_{DOF_{mean}}$	15,666	36,365	67,054	118,317	185,475	269,636
$N_{DOF_{max}}$	21,735	42,553	79,056	132,777	206,136	298,494

Table 4.2: Number of DOF for different grain numbers.

Considering a given stiffness tensor of an isotropic materials \mathbf{C}_{iso} , this tensor can be expressed in the following projection representation

$$\mathbf{C}_{\text{iso}} = \lambda_1 \mathbf{P}_1^{\text{iso}} + \lambda_2 \mathbf{P}_2^{\text{iso}} \quad , \quad (4.5)$$

where \mathbf{P}_i are the projectors and λ_i represents the elastic eigenvalues. For isotropic materials, the eigen-projectors (KOWALCZYK-GAJEWSKA AND OSTROWSKA-MACIEJEWSKA, 2009), are given by

$$\mathbf{P}_1^{\text{iso}} = \frac{1}{3} \mathbf{I} \otimes \mathbf{I}, \quad \mathbf{P}_2^{\text{iso}} = \mathbf{I}^s - \mathbf{P}_1^{\text{iso}} \quad . \quad (4.6)$$

In Equation (4.6), \mathbf{I} is the second-order identity tensor, \mathbf{I}^s is the fourth-order symmetric tensor resulting from $\mathbf{I}^s = \mathbf{C}^{-1} \mathbf{C}$ product and the symbol “ \otimes ” is the dyadic or tensor product. The apparent bulk \hat{K} and shear \hat{G} moduli are evaluated by the projection of the apparent stiffness tensor $\hat{\mathbf{C}}$ on the space of isotropic elasticity tensor (FRITZEN ET AL., 2009). The most common representation of a stiffness tensor of a isotropic material is

$$\mathbf{C}_{\text{iso}} = 3K \mathbf{P}_1^{\text{iso}} + 2G \mathbf{P}_2^{\text{iso}} \quad , \quad (4.7)$$

the bulk and shear moduli resulting from the projection of an anisotropic tensor onto an isotropic tensor treated by Fedorov (FEDOROV, 1968), are expressed by

$$3\hat{K} = \hat{\mathbf{C}} \cdot \mathbf{P}_1^{\text{iso}} = \frac{1}{3} \hat{C}_{iikk} \quad , \quad (4.8)$$

and

$$2\hat{G} = \frac{1}{5} \hat{\mathbf{C}} \cdot \mathbf{P}_2^{\text{iso}} = \frac{1}{5} \left(\hat{C}_{ijij} - \frac{1}{3} \hat{C}_{iikk} \right) \quad , \quad (4.9)$$

where for repeated indices the Einstein's summation convention is used. Effective properties \bar{K} and \bar{G} can be evaluated likewise using \bar{C} over all realizations for a specific RVE. The effective values of \bar{E} and $\bar{\nu}$ are calculated using the following equations

$$\bar{E} = \frac{9\bar{K}\bar{G}}{3\bar{K} + \bar{G}} \quad , \quad (4.10)$$

$$\bar{\nu} = \frac{3\bar{K} - 2\bar{G}}{2(3\bar{K} + \bar{G})} \quad . \quad (4.11)$$

Many works in the literature were dedicated to analyze the existence and size of the RVE (REN AND ZHENG, 2002; GITMAN ET AL., 2007; XU AND CHEN, 2009; SALAHOUELDADI AND HADDADI, 2010) in general for heterogeneous materials with computational simulations. Also using experimentation by digital image correlation (LIU, 2005). The RVE is defined as the minimum element in the mesoscale, that contains the material microconstituents leading to a possible representation of the macroscale. This reduces the computational cost of simulations in the macroscale when heterogeneities are considered. In case of polycrystal materials, an ideal macroscopic behavior is reached when $N_{gr} \rightarrow \infty$. Geometrical heterogeneities and the random constitutive behavior can cause a dependency in the macroscopic elastic properties, due to the anisotropic characteristics of the mesoscale. This analysis was pursued by Ren and Zheng (2002), they compared results with their previous work (REN AND ZHENG, 2004) that used periodic grain shapes.

The analyses presented by Voigt (1889) and Reuss (1929), proposed the relation between the monocrystal elastic constants and the general quasi-isotropic behavior of the polycrystal aggregate. The homogeneous strain is maintained in the body when the polycrystal is stressed in all directions, Voigt formulated expressions in terms of the stiffness tensor C_{ijkl}^V . In other study, Reuss proposed equations where homogeneous stress is maintained while the polycrystal is strained. In that case, the formulation is based on the compliance elastic constants S_{ijkl}^R . The superscripts V and R refer to the Voigt and Reuss analyses. Both analyses offer a set of equations to evaluate bulk, shear and Young moduli, see details in (HILL, 1952; TROMANS, 2011; KUBE, 2016). Hill (1952), established that a homogenized stiffness tensor lies between the Voigt and Reuss bounds. The author proposed the following expression

$$[\mathbf{S}^R]^{-1} \leq \bar{\mathbf{C}} \leq \mathbf{C}^V \quad , \quad (4.12)$$

and

$$\{K^R, E^R, G^R\} \leq \{\bar{K}, \bar{E}, \bar{G}\} \leq \{K^V, E^V, G^V\} \quad . \quad (4.13)$$

For comparison purposes, an average between Voigt and Reuss conditions V - R proposed by Hill (1952) is evaluated and expressed as \mathbf{C}^{V-R} , K^{V-R} , E^{V-R} and G^{V-R} . Additionally, it is useful the evaluation of the level of anisotropy of materials independently of its lattice structure. In the literature, there are schemes of comparison the level of anisotropy between different materials. Zener (1948) defined an anisotropy factor A_z for crystals of cubic symmetry based on the ratio of extreme values of shear modulus. Kube (2016) in his work and in the references therein (CHUNG AND BUESSEM, 1967; RANGANATHAN AND OSTOJA-STARZEWSKI, 2008), exposes a variety of anisotropy factors of materials with different lattices in its review. Kube defined an anisotropy factor A^L as the The log-Euclidean distance between \mathbf{C}^V and \mathbf{C}^R . This factor offers a universal measure of anisotropy, applicable to all crystalline materials. The expression of the A^L index is

$$A^L = (\mathbf{C}^V, \mathbf{C}^R) = \left\{ \left[\ln \left(\frac{K^V}{K^R} \right) \right]^2 + 5 \left[\ln \left(\frac{G^V}{G^R} \right) \right]^2 \right\}^{1/2} \quad , \quad (4.14)$$

which are valid for any crystal symmetry. Using the material properties shown in Table 4.1, the values of the A^L parameter for each material are listed in Table 4.3.

	A^L
Cu	0.695
Zn	0.652

Table 4.3: Absolute measure of anisotropy of Cu and Zn.

The distance between C^V and C^R yields to zero when the crystal is elastically isotropic. The parameter A^L will be helpful to compare the final homogenized results. In terms of implementation, an algorithm is presented in Figure 4.2, the parallelized sections using MPI are also specified.

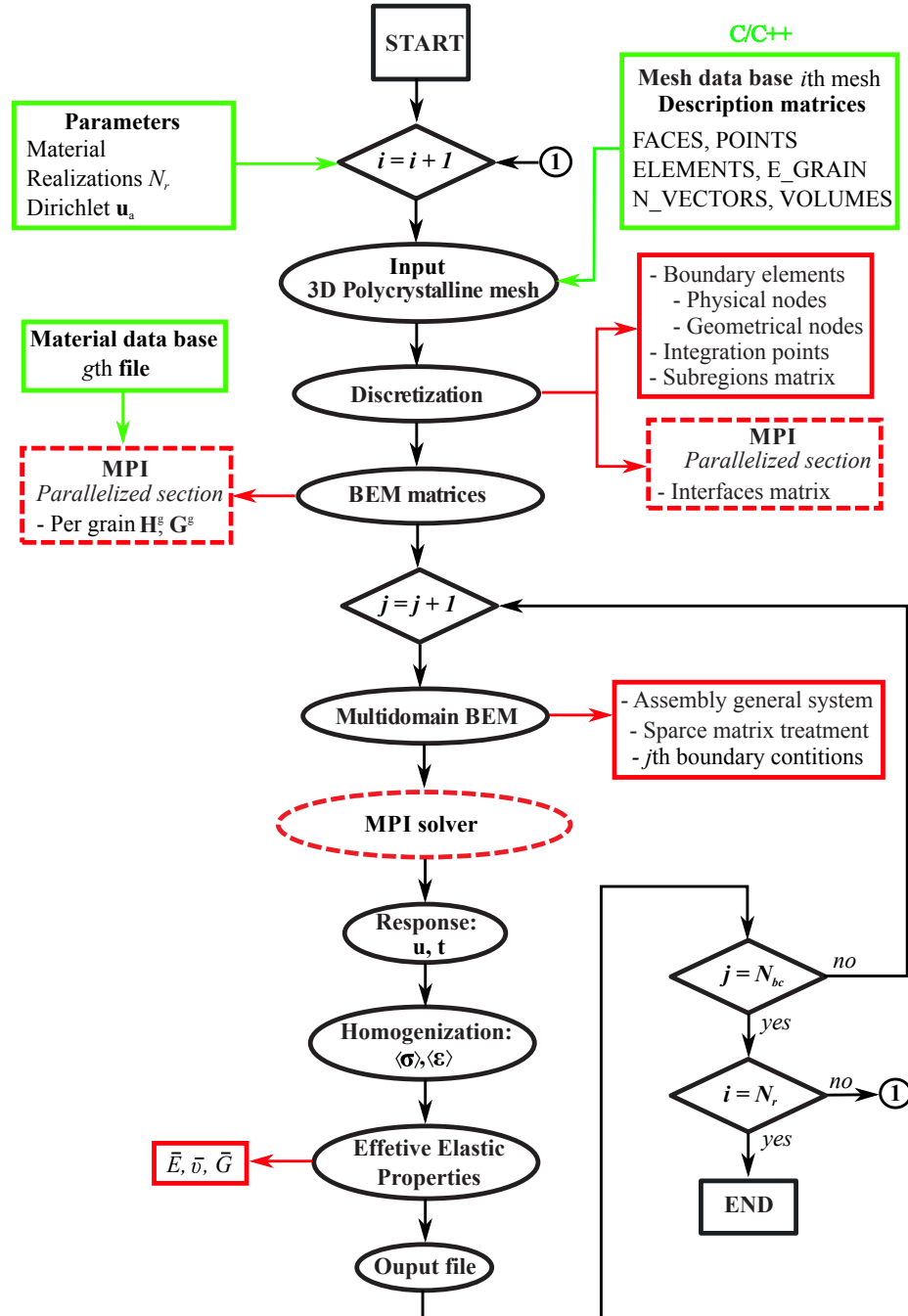


Figure 4.2: Algorithm to evaluate \bar{E} and \bar{G} .

As mentioned, this is a multi-compiler algorithm composed by sections implemented using C, C++ for meshing, Fortran 90 for BEM analysis and post-processing. The BEM analysis corresponds to the root of the algorithm, databases are already generated for mesh and materials in separated directories, see Figure 2.3 and 2.9. Input parameters, such as the number of realizations N_r , material and Dirichlet boundary conditions \mathbf{u}_a , must be defined. The counter “ i ”, in Figure 4.2, refers to the loop over the number of realization N_r , where different polycrystalline structures are loaded for each realization. The BEM grain matrices \mathbf{H}^g and \mathbf{G}^g are computed in a parallelized module, Figure 3.2, for each realization. Furthermore, geometrical description matrices such as geometrical and physical nodes, integration points in the isoparametric element, subregions and interfaces are defined. The counter “ j ” refers to the loop over the six displacement boundary conditions N_{bc} , Figure 4.1. Each boundary condition demands changes in the assembly of the general matrix system, this is a critical section in the code. Then, an efficient algorithm was developed to assembly the general matrix in a reduced format for highly sparse matrices.

4.1.1 Effective Young’s and shear moduli results

The Young’s and shear moduli are evaluated in each polycrystal material for a set of number of grains, using a basic statistical analysis. The apparent and effective values of these quantities are determined in a similar way as presented Fritzen et al. (2009) for fcc materials. Moreover, hcp materials are also considered in this analysis.

Here, the apparent Young’s (\hat{E}) and shear (\hat{G}) values are evaluated from Equations (4.10) and (4.11), respectively. The effective Young’s (\bar{E}) and shear (\bar{G}) moduli are computed as the mean value from \hat{E} and \hat{G} , respectively. From the statistical theory, a confidence interval for normal distribution is assumed to guarantee that the interval contains a true value of the unknown parameter. For normal distributions, the particular probability of 99.7% used is

$$P(\bar{X} - 3\sigma < X < \bar{X} + 3\sigma) = 0.997 \quad , \quad (4.15)$$

where X takes the value of \hat{E} or \hat{G} , the term \bar{X} refers to the mean value and σ is the standard deviation. Curves of all grain numbers are generated showing the asymptotic trend of the mean values of \bar{E} and \bar{G} for a probability of 99.7% and standard deviation $\sigma(\hat{E})$ and $\sigma(\hat{G})$. Histograms

of 100 values of apparent $\sigma(\hat{E})$ and $\sigma(\hat{G})$ are compared with the Gaussian probability curve for the polycrystal cell of 210 grains (FRITZEN ET AL., 2009).

Results of simulations of the apparent \hat{E} and \hat{G} values for each configuration of Cu are shown in Figure 4.3(a,b) and for Zn in Figure 4.3(c,d). The number of grains in the x -axis, the apparent property in y -axis, the maximum and minimum values and the scatter dispersion using a probability of 97.5% with 3σ are shown.

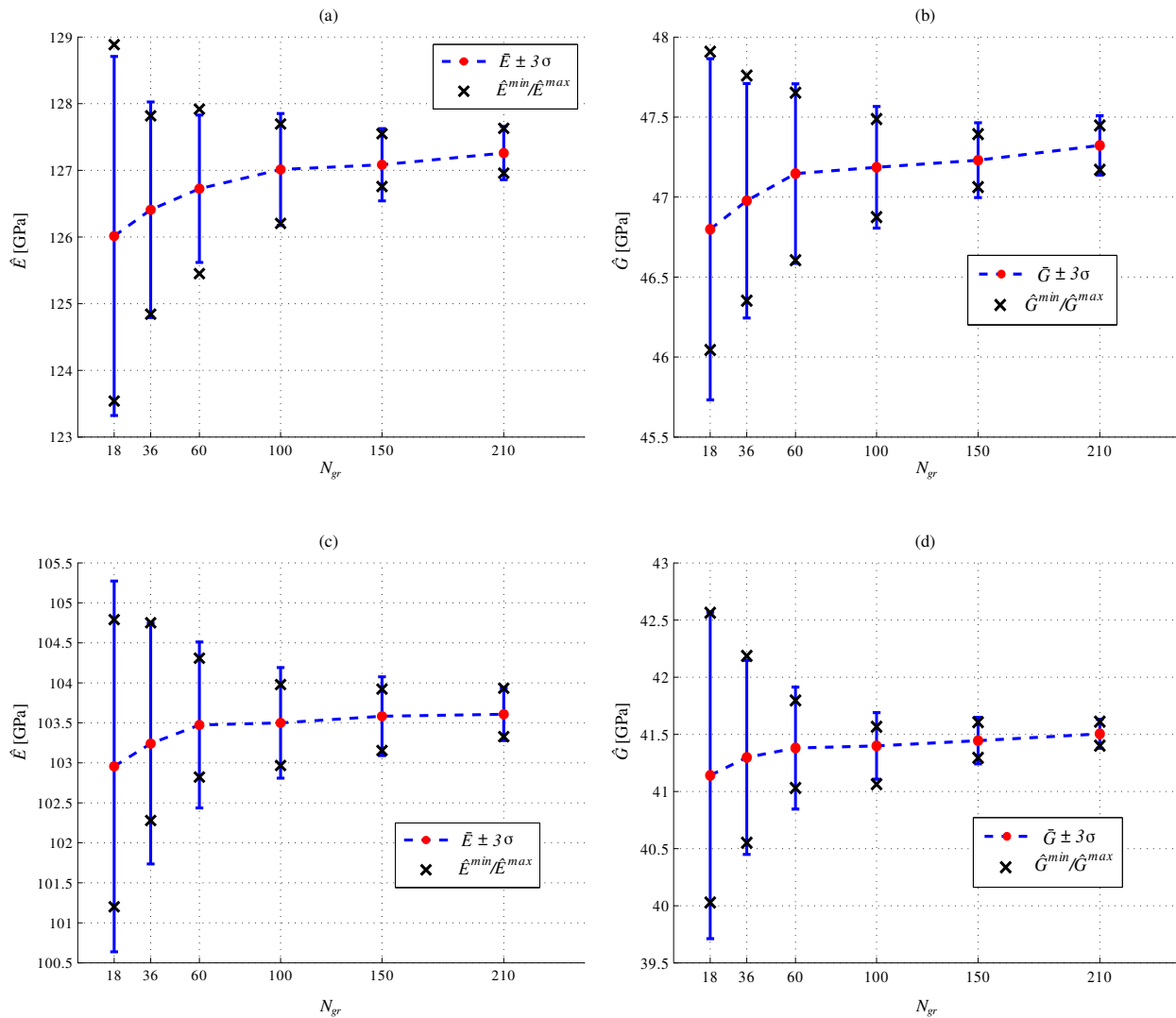


Figure 4.3: Macroscopic properties: (a) Young's modulus of Cu, (b) shear modulus of Cu, (c) Young's modulus of Zn and (d) shear modulus of Zn.

Increasing the number of grains and DOF, the dispersion over the 100 realizations decrease.

Moreover, the dashed curve obtained by the mean values will take an expected asymptotic tendency. Figure 4.4, shows the comparison between the \hat{E} and \hat{G} values, the curves are based on 100 realization values for each case. A Gaussian probability function is also shown when the specimen contains 210 grains of Cu and Zn.

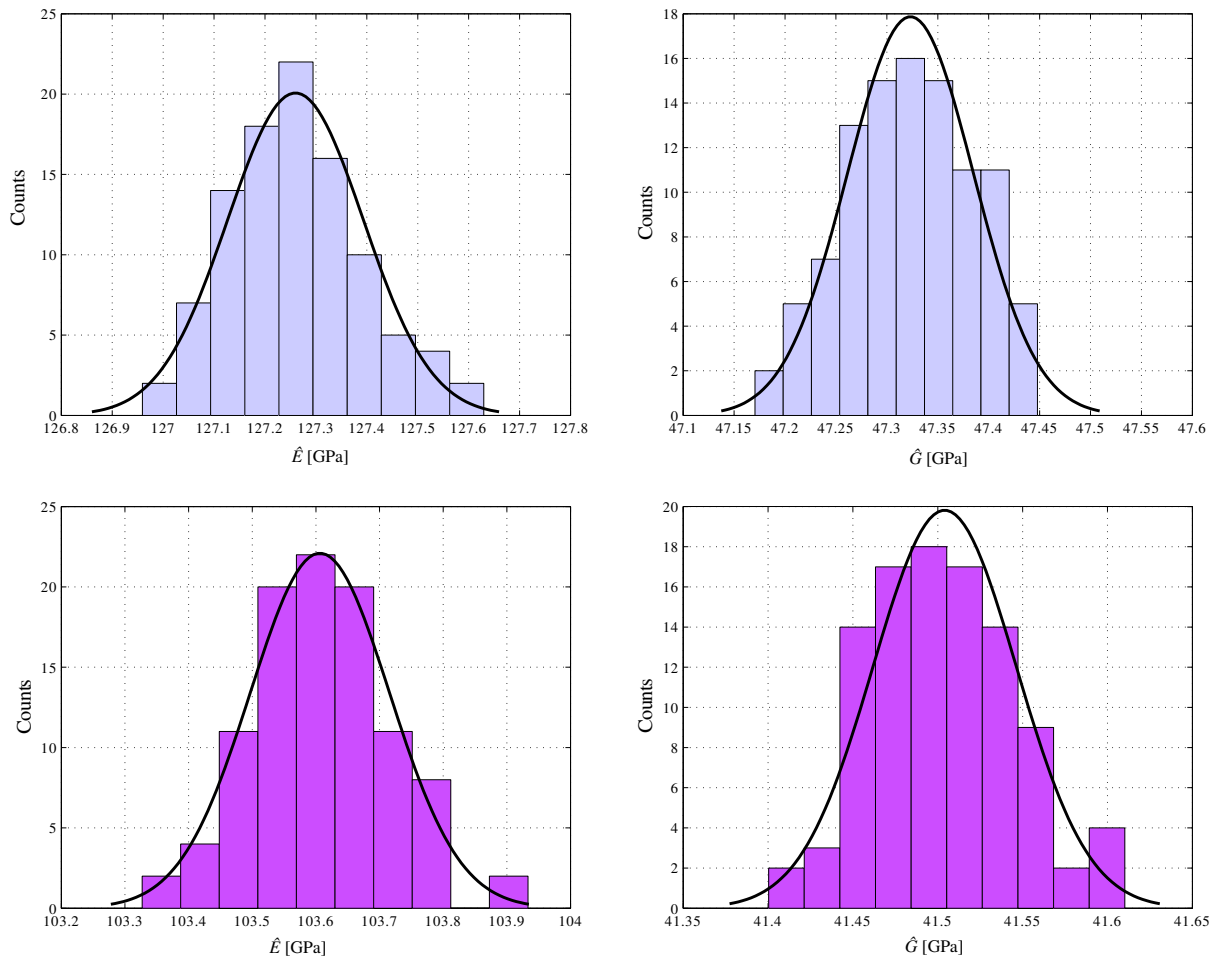


Figure 4.4: Histogram and normal distribution: (a) Young's modulus of Cu, (b) shear modulus of Cu, (c) Young's modulus of Zn and (d) shear modulus of Zn. For a 210 grains specimen.

The trend to a mean value of \hat{E} and \hat{G} are exposed in the histograms presented in Figure 4.4. The response from the realizations can be adjusted to a probability curve with the shape of a normal distribution. Numerical values of mean and deviation of Young's modulus of both materials in all aggregate tests are shown in Table 4.4.

N_{gr}	$\bar{E} \pm 3\sigma(\bar{E})$	
	Cu	Zn
18	126.01 ± 2.693	102.95 ± 2.317
36	126.40 ± 1.616	103.24 ± 1.505
60	126.72 ± 1.105	103.47 ± 1.037
100	127.01 ± 0.839	103.49 ± 0.691
150	127.08 ± 0.542	103.58 ± 0.493
210	127.25 ± 0.399	103.60 ± 0.270

Table 4.4: Effective and confidence interval of Young's modulus in [GPa], based on different numbers of grains per aggregate.

Numerical values of mean and deviation of shear modulus of both materials in all aggregate tests are shown in Table 4.5.

N_{gr}	$\bar{G} \pm 3\sigma(\bar{G})$	
	Cu	Zn
18	46.79 ± 1.066	41.14 ± 1.428
36	46.97 ± 0.732	41.29 ± 0.849
60	47.14 ± 0.560	41.37 ± 0.533
100	47.18 ± 0.380	41.39 ± 0.291
150	47.23 ± 0.233	41.44 ± 0.203
210	47.32 ± 0.185	41.50 ± 0.120

Table 4.5: Effective and confidence interval of shear modulus in [GPa], based on different numbers of grains per aggregate.

Results present a decreasing deviation when the number of grains increase, showing a more accurate response of the homogenization process to obtain the macroscopic isotropic behavior of the polycrystal aggregate. The effective stiffness tensor $\bar{\mathbf{C}}$ for Cu after 100 realizations using a 210 grains aggregate in the simulation is

$$\bar{\mathbf{C}} = \bar{C}_{ijkl} = \begin{bmatrix} 201.13 & 104.33 & 105.36 & -0.28 & 0.30 & 0.34 \\ 104.33 & 201.59 & 104.82 & -0.34 & -0.41 & -0.62 \\ 105.36 & 104.82 & 200.56 & 0.72 & 0.17 & 0.38 \\ -0.28 & -0.34 & 0.72 & 46.92 & 0.45 & -0.48 \\ 0.30 & -0.41 & 0.17 & 0.45 & 47.29 & -0.28 \\ 0.34 & -0.62 & 0.38 & -0.48 & -0.28 & 46.41 \end{bmatrix} \text{ GPa} , \quad (4.16)$$

and the effective stiffness tensor for Zn after 100 realizations of 210 grains aggregate in the simulation is

$$\bar{\mathbf{C}} = \bar{C}_{ijkl} = \begin{bmatrix} 123.63 & 41.22 & 40.76 & 0.07 & 0.24 & 0.11 \\ 41.22 & 126.83 & 41.16 & 0.11 & -0.09 & -0.04 \\ 40.76 & 41.16 & 122.90 & 0.06 & 0.48 & -0.06 \\ 0.07 & 0.11 & 0.06 & 41.73 & -0.13 & 0.05 \\ 0.24 & -0.09 & 0.486 & -0.13 & 40.40 & 0.18 \\ 0.11 & -0.04 & -0.06 & 0.05 & 0.18 & 41.96 \end{bmatrix} \text{ GPa} . \quad (4.17)$$

Both tensors tend to isotropic behavior, due to the large number of grains used for these specimens. Resulting in the higher values of components that correspond to an isotropic elastic tensor.

At first stage, when results of these two materials are compared, it is easy to perceive that all numerical dispersion values $3\sigma(\hat{E})$ and $3\sigma(\hat{G})$ for Zn are less than values of Cu, Tables 4.4 and 4.5, respectively. According to the values presented in Table 4.3 for Cu and Zn of the anisotropic A^L index, it can be inferred that Cu results more anisotropic than Zn. This fact is observed in the dashed curves in Figure 4.3.

For validation purposes, the effective elastic constants of both materials shown in Equations (4.16) and (4.17) for 210 grains and 100 realization, are compared with different values from the literature in Tables 4.6 and 4.7. In case of Cu, Benedetti and Aliabadi (2013b) present in their

work the average assembly stiffness $\hat{\mathbf{C}}$ tensor for 20 grains and 100 realizations. This is not a useful comparison, due to the difference in the grain numbers. Thus, the calculated error in the third column shown in Table 4.6 is apparently large. Small errors were obtained when compared with the average V - R bound analysis and the experimental results presented by Beran et al. (1996).

\bar{C}_{ijkl}	Results		Benedetti and Aliabadi (2013b)		Beran et al. (1996)			
	210 grains	20 grains	Error(%)		V - R	Error(%)	Exp.	Error(%)
\bar{C}_{1111}	201.13	205.9	2.31		201.0	0.06	199.0	1.07
\bar{C}_{2222}	201.59	206.4	2.33		202.15	0.27	200.7	0.44
\bar{C}_{3333}	200.56	206.7	2.97		201.95	0.68	200.9	0.16
\bar{C}_{1212}	46.41	51.5	9.88		47.25	1.77	46.42	0.02
\bar{C}_{1313}	47.29	51.3	7.81		47.53	0.50	47.36	0.14
\bar{C}_{2323}	46.92	50.7	7.45		46.42	1.07	47.66	0.54

Table 4.6: Comparison of elastic constants of Cu in [GPa].

Numerical results of Zn were compared with the V - R average analysis presented by Tromans (2011), showing the independent elastic constants and the respective errors in Table 4.7.

\bar{C}_{ijkl}	Results		Tromans (2011)	
	210 grains		V - R	Error(%)
\bar{C}_{1111}	123.63		120.59	2.52
\bar{C}_{2222}	126.83		120.59	5.17
\bar{C}_{3333}	122.90		120.59	1.91
\bar{C}_{1122}	41.22		38.67	6.59
\bar{C}_{1133}	40.76		38.67	5.40
\bar{C}_{2233}	41.16		38.67	6.43
\bar{C}_{1212}	41.96		40.96	2.44
\bar{C}_{1313}	40.40		40.96	1.36
\bar{C}_{2323}	41.73		40.96	1.14

Table 4.7: Comparison of elastic constants of Zn in [GPa].

Now, results of \bar{E} and \bar{G} for both materials presented in Tables 4.4 and 4.5 are compared with different references. A comparison with results reported by Fritzen et al. (2009) for 100 grains and 200 realizations are shown in Table 4.8. Acceptable results of mean values and deviation were obtained, despite the difference between the number of grains of the specimens tested. Furthermore, values given by Kiewel et al. (1996) from Kröner (1977) and V - R analysis are presented for Cu with its respective errors, showing expected numerical results for mean values, see Table 4.8.

	Results		Fritzen et al. (2009)		Kiewel et al. (1996)			
	210 grains		100 grains	Error(%)	V - R	Error(%)	Kröner	Error(%)
\bar{E}	127.25		129.47	1.71	127.35	0.266	129.7	2.07
$3\sigma(\bar{E})$	0.399		0.816					
\bar{G}	47.32		48.23	1.88	47.4	0.46	48.3	2.31
$3\sigma(\bar{G})$	0.185		0.339					

Table 4.8: Comparison of Young's, shear moduli and deviation of Cu in [GPa].

Similar to the last case, results of Zn are also compared with reference values presented by Kiewel et al. (1996) from Kröner (1977) and V - R results in (TROMANS, 2011). For this case, there are not available deviation values from other numerical results to compared with values in Table 4.4 and 4.5. Again reference values and errors are shown in Table 4.9 for hexagonal Zn polycrystals.

	Results		Ref. (KIEWEL ET AL., 1996)		Ref. (TROMANS, 2011)	
	210 grains		Kröner	Error(%)	V - R	Error(%)
\bar{E}	103.60		104.5	0.86	101.8	1.76
\bar{G}	41.50		41.9	0.95	41.0	1.21

Table 4.9: Comparison of Young's, shear moduli and deviation of Zn in [GPa].

In summary, validations of all results from numerical simulations were presented and compared for two materials with different lattice structures, results in Tables 4.8 and 4.9 show less error in simulations of Zn than Cu in terms of mean \bar{E} and \bar{G} values. This confirms the concept given by the calculated values of A^L for both materials.

4.2 Dynamic behavior

The dynamic time dependent responses of displacement $\mathbf{u}_{\tau+\Delta\tau}$ and traction $\mathbf{t}_{\tau+\Delta\tau}$ of polycrystalline materials are evaluated. First, for step, ramp, and harmonic dynamic loads, a total of 150 tests are carried out. Therefore, 50 simulations are run for each material using different polycrystal aggregates and distribution of the crystalline orientations. Second, a mesh and time step dependency is analyzed with a total of 90 simulations using Cu and step load. In order to provide accurate numerical results, the time step is $\Delta\tau = 20$ ns for all simulations. The specification of each test is listed in Table 4.10.

	N_{times}	Simulation time	Load
Zn	200	4 μ s	Harmonic
Cu	100	2 μ s	Ramp
Fe	85	1.7 μ s	Step

Table 4.10: Simulations.

The dynamic model is validated evaluating \bar{E} given in Tables 4.4 and 4.5 and rewritten in Table 4.11, within the analytical isotropic solutions. In addition to the materials presented in Table 4.1, bcc iron (Fe) will be also used in the simulations. The three independent elastic constant of Fe are $C_{11} = 230$ GPa, $C_{12} = 135$ GPa and $C_{44} = 171$ GPa (HUNTINGTON, 1958). The value of the effective Young's modulus is 210 GPa, given by Kiewel et al. (1996). This procedure offers an approximate framework to compare anisotropic dynamic responses to analytical solutions due to the lack of anisotropic direct analytical models.

	$\bar{E} \pm 3\sigma(\bar{E})$
Cu	127.25 \pm 0.399
Zn	103.60 \pm 0.270

Table 4.11: Effective Young's modulus in [GPa] evaluated in a 210 grain specimen.

A cantilever prismatic bar is used for the simulations. The geometrical dimensions and dynamic loads are shown in Figure 4.5. In these three cases, the maximum stress (σ_o) is 100 MPa

applied in the y -axis.

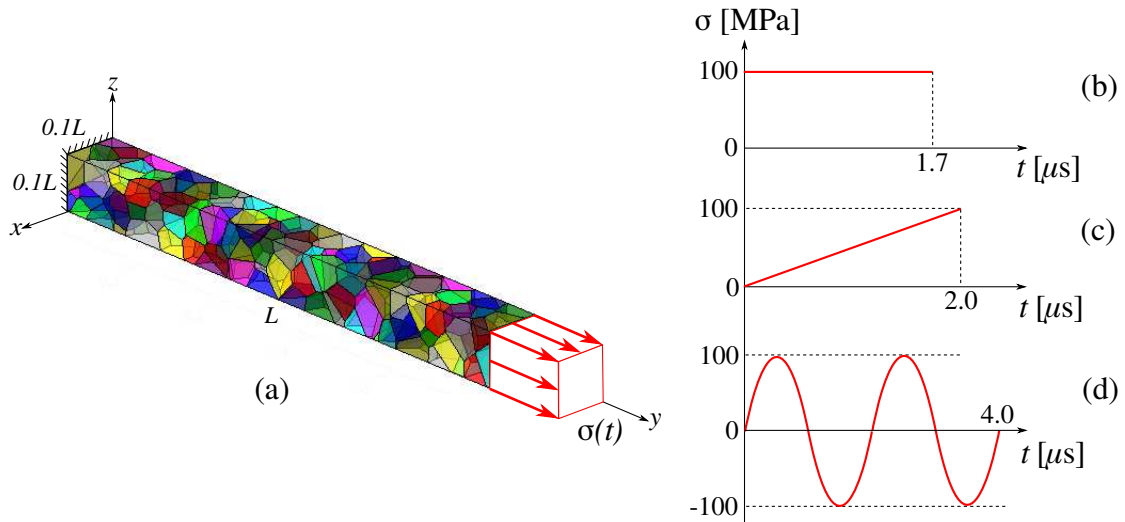


Figure 4.5: (a) Physical model of 180 grains, $L = 1$ mm and boundary conditions: (b) step, (c) ramp and (d) harmonic loads.

Figure 4.5 illustrates the fixed surface at $y = 0$ and the application load surface at $y = L$ with $L = 1$ mm. The number of DOF and boundary elements of all specimens of 180 grains used in the simulations are shown in Table 4.12.

	Max	$Mean$	Min
$Elements$	27,620	26,120	24,568
DOF	248,580	235,086	221,112

Table 4.12: Elements and DOF of 180 grains polycrystal aggregate.

The implementation algorithm of these simulations starts with the input user parameters as the number of time steps N_{times} , the size of time step $\Delta\tau$, the applied load in function of the time $\sigma_a(\tau)$, the constraint displacements \mathbf{u}_a and the material properties, see Figure 4.6. Basically, The computation of the \mathbf{M}^g matrix is also implemented in a MPI module, where the data load is distributed from the master process to the remaining process taking care of an adequate balance to gain computational processing time. Finally, the displacement and traction evaluated in each time step are stored in a directory to be imported by the post-processing, while the BEM application is still running.

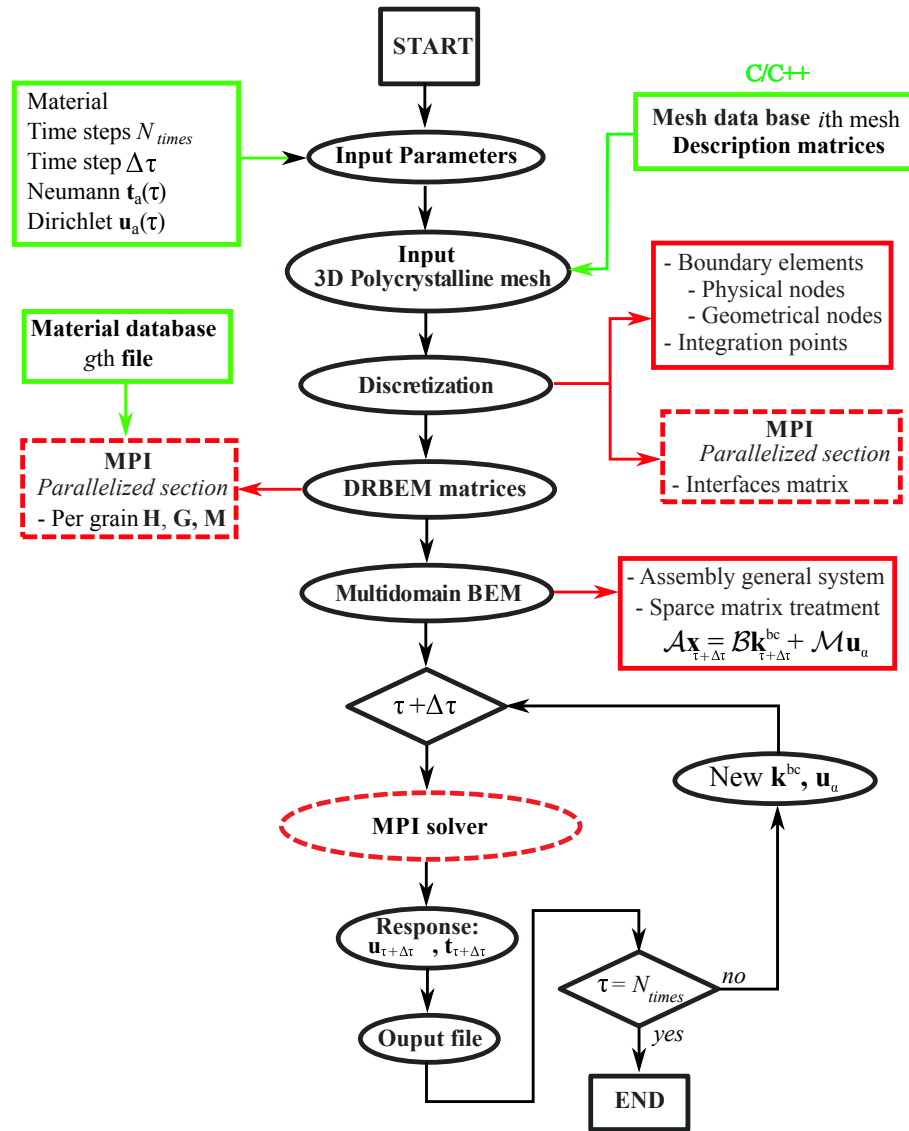


Figure 4.6: Algorithm to evaluate dynamic time-dependent $u_y(t)$ response.

The general system of equations is computed before the loop of time steps. Matrices \mathcal{A} , \mathcal{B} and \mathcal{M} are kept constant. The load σ_a change through the time depending of the type of load. Therefore, the vector $\mathbf{k}_{\tau+\Delta\tau}^{bc}$ and \mathbf{u}_a have to be updated. The solution of the final system of equations requires a high computational performance due to the large number of DOF.

4.2.1 Analytical isotropic models

The dynamic response of a prismatic bar under axial step load $\sigma(t) = \sigma_o$ in Figure 4.5(b), is obtained using the mode-superposition analysis, as shown in detail by Clough and Penzien (2003). The displacement analytical response is

$$u(y,t) = \frac{8P_o}{\pi^2} \frac{L}{EA} \sum_{n=1}^{\infty} \left\{ (-1)^{n+1} \left(\frac{1 - \cos \omega_n t}{(2n-1)^2} \right) \sin \left[\frac{(2n-1)\pi y}{L} \right] \right\} \quad n = 1, 2, \dots, \quad (4.18)$$

where P_o is the applied force, E is the Young's modulus, L and A are the length and cross-sectional area respectively, y is the position from the point to be analyzed, n is the number of vibration modes and ω_n is the natural frequency of the n th vibration mode expressed as

$$\omega_n = (2n-1) \frac{\pi}{2} \sqrt{\frac{EA}{mL^2}} \quad n = 1, 2, \dots, \quad (4.19)$$

being m the mass per unit length. Analogously, when a ramp load is applied as $\sigma(t) = \sigma_o t$, Figure 4.5(c), the analytical solution is obtained as

$$u(y,t) = \frac{8P_o}{\pi^2} \frac{L}{EA} \sum_{n=1}^{\infty} \left\{ \frac{(-1)^{n+1}}{(2n-1)^2} \left(t - \frac{1}{\omega_n} \sin \omega_n t \right) \sin \left[\frac{(2n-1)\pi y}{L} \right] \right\} \quad n = 1, 2, \dots \quad (4.20)$$

In case of harmonic load applied as $\sigma(t) = \sigma_o \sin \omega t$, where ω is the frequency of the wave, as shown in Figure 4.5(d), the analytical solution is obtained as

$$u(y,t) = \frac{2P_o}{mL} \sum_{n=1}^{\infty} \left\{ \frac{(-1)^{n+1}}{\omega_n(\omega_n^2 - \omega^2)} (\omega_n \sin \omega t - \omega \sin \omega_n t) \sin \left[\frac{(2n-1)\pi y}{L} \right] \right\} \quad n = 1, 2, \dots \quad (4.21)$$

As it was shown in Figure 4.4, the effective properties of polycrystalline aggregates converge to the isotropic constitutive behavior. Accordingly, the dynamic anisotropic model, is validated by substituting the effective macroscopic Young's modulus \bar{E} into the Equations (4.18), (4.20) and (4.21). The values of effective Young's moduli used for the different materials employed in this work are presented in Table 4.11.

4.2.2 Dynamic time-dependent results

For each material and boundary condition, 50 simulations were carried out. The same statistical analysis is used with a Gaussian distribution of confidence interval 3σ corresponding to a probability of 99.7%. Curves are generated with the mean value of the average displacement \bar{u}_y in the $y = L$ surface and its corresponding 3σ deviation for each current time instant $\tau + \Delta\tau$. The Fe simulations are shown in Figure 4.7.

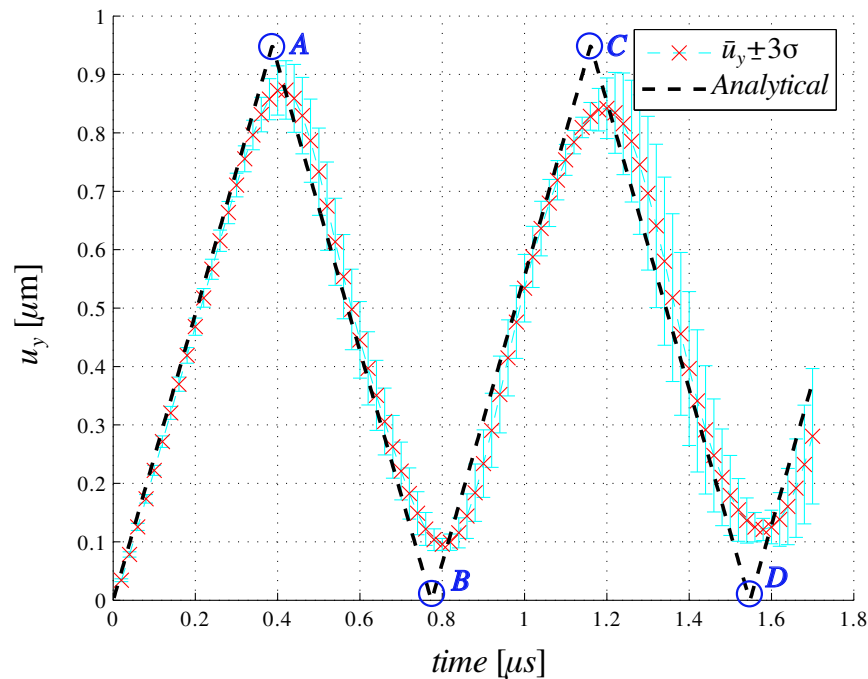


Figure 4.7: Fe under step load. The analytical solution is given in (CLOUGH AND PENZIEN, 2003).

where the u_y displacement illustrates the wave characteristic behavior of this non-damped model under a dynamic high-rate step load. As expected, the mean values of \bar{u}_y are consistent with the

analytical values. It is observed that, there are solution gradient discontinuities at points A , B , C , and D in Figure 4.7. At these points, the evaluation of an accurate response using this model is a difficult task. The simulations of Cu by applying a ramp load are shown in Figure 4.8.

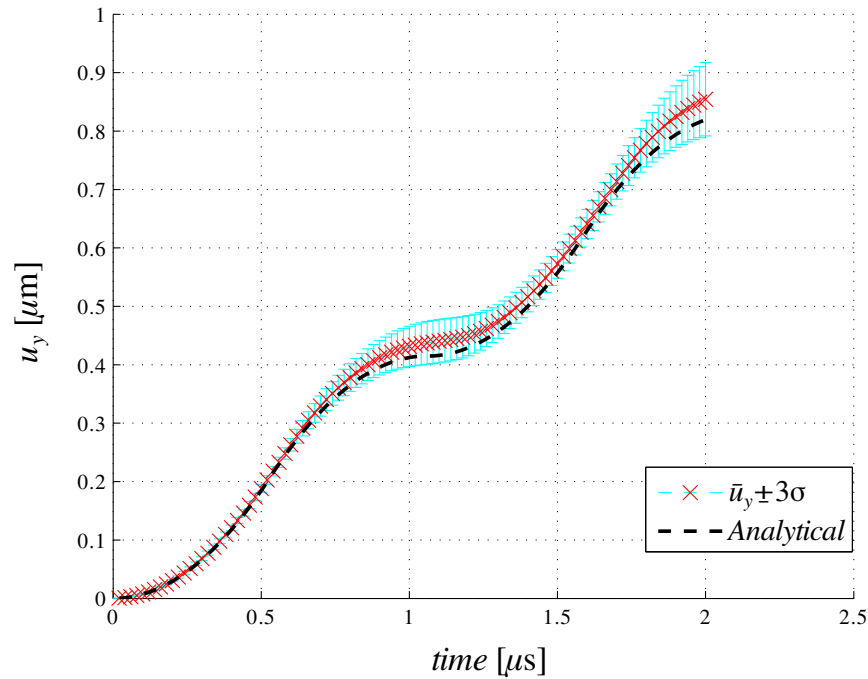


Figure 4.8: Cu under ramp load. The analytical solution is given by the Equation (4.20).

In the ramp case, a smooth wave travels through the body leading to continuous increments of the displacement u_y . This effect is distinct from the step load case. The curve does not have gradient discontinuities, being numerically feasible for the model to obtain accurate results with small deviations. An additional case is presented in Figure 4.9, where the harmonic load is applied. In this case, the resonance condition is reached when the frequency ω is equal to the first natural frequency ω_1 , Equation (4.21). Results of \bar{u}_y are consistent with the analytical values. However, a high deviation 3σ is obtained after $150\Delta\tau$ ($3 \mu\text{s}$). The harmonic analytical solution shows abrupt changes in the u_y direction. In contrast to the step load case, this analytical solution has a continuous gradient in the entire domain. The resonance condition leads to an incremental unstable behavior.

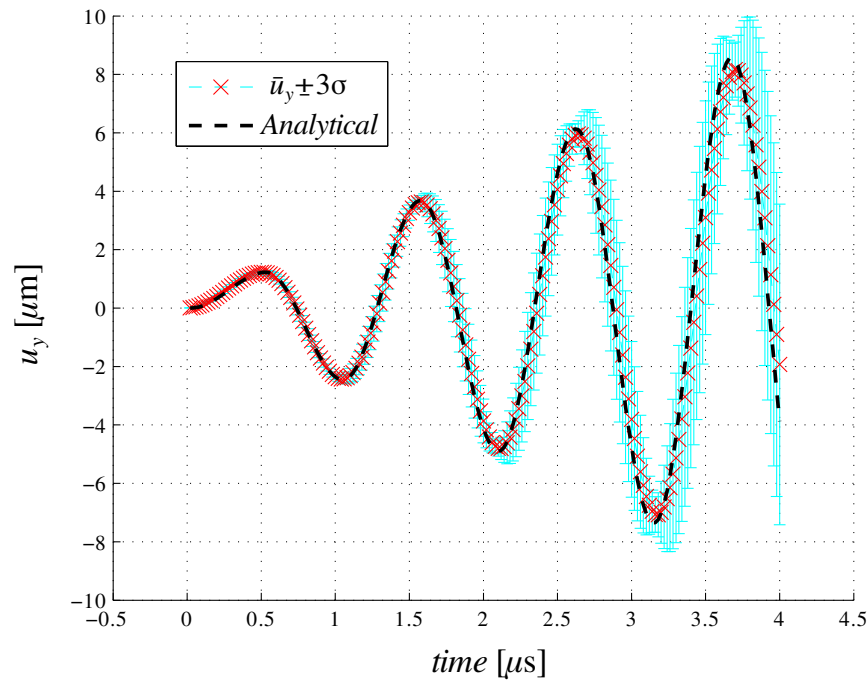


Figure 4.9: Zn under harmonic load. The analytical solution is given by the Equation (4.21).

Results are described by absolute errors $Er(\bar{u}_y)$ and 3σ deviations. It is observed that the dynamic wave produced by the step load contains sudden changes as shown in Figure 4.7 at points A , B , C and D . The undetermined derivatives of the analytical function at these points causes ill conditioning in the BEM matrices. The evaluation of the second derivative of the displacement $\ddot{\mathbf{u}}_{\tau+\Delta\tau}$ is enforced by the BEM model at these simulation points. In contrast, the ramp and harmonic loads produce smooth analytical responses. The absolute error is evaluated by $Er(\bar{u}_y) = |\bar{u}_y - u_a|$, where \bar{u}_y is the numerical average and u_a is the analytical solution.

Comparisons can be made to evaluate the capability of the BEM model under these boundary conditions considering that each test is performed N_{times} . All the three cases exhibit a similar trend, the accuracy of the mean value of displacement \bar{u}_y decreases and the deviation 3σ increases over time. According to the results shown in Figure 4.7, the main differences between the numerical and analytical models are at the instants at which the solution has gradient discontinuities, as in the A , B , C , and D points shown in Figure 4.7. Table 4.13 gives the numerical results at these specific points.

	$\Delta\tau$	$19\Delta\tau$ (A)	$39\Delta\tau$ (B)	$58\Delta\tau$ (C)	$77\Delta\tau$ (D)	$85\Delta\tau$
<i>Time</i> [μs]	0.02	0.38	0.78	1.16	1.54	1.7
$Er(\bar{u}_y)$ [μm]	0.013	0.074	0.089	0.1198	0.1187	0.0926
3σ [μm]	0.0024	0.035	0.018	0.023	0.038	0.1195

Table 4.13: Instants of sudden changes of for Fe simulation with step load.

As listed in Table 4.13, the absolute error $Er(\bar{u}_y)$ increases until point *C*. Hence, the 3σ deviation presents an irregular path that increases from the first $\Delta\tau$ to the point *A* and from *B* to *D* but decreases in the interval *A-B*. Therefore, at $85\Delta\tau$, as expected, the highest value of deviation is observed. In the simulation results of Cu, smooth curves of error and deviation follow the expected forms such as its response Figure 4.8. Initially, the error and deviation are closed until $0.74\ \mu\text{s}$ ($37\Delta\tau$), where $Er(\bar{u}_y) \approx 0.012\ \mu\text{m}$ and $3\sigma = 0.02\ \mu\text{m}$. After this instant, the deviation increases by almost twice the error value. In the case of the harmonic load in Zn, as shown in Figure 4.9, the simulation is longer than that of Fe and Cu, as $200\Delta\tau$ is used. Therefore, the values of error and deviation are higher at $4\ \mu\text{s}$. In this case, the analytical solution also contains abrupt changes. However, this is a differentiable function in its entire domain, and the BEM model can evaluate the solution more accurately. For illustrative purposes, Table 4.14 gives the maximum and minimum values of $Er(\bar{u}_y)$ and 3σ for the three materials in each simulated time interval.

	$Er(\bar{u}_y)_{max}$	$Er(\bar{u}_y)_{min}$	$3\sigma_{max}$	$3\sigma_{min}$
Fe	0.1197	0.00244	0.143	0.002427
Cu	0.0241	0.00013	0.062	0.000041
Zn	0.1471	0.00091	5.547	0.001

Table 4.14: Maximum and minimum values of $Er(\bar{u}_y)$ and 3σ in [μm].

As mentioned above, the numerical responses become worse as the time increases. An adequate comparison can be made in the same interval time for all the tests. From Table 4.14, the smoothest solution of the BEM model obtained with the ramp load is more accurate with a maximum error of $0.0241\ \mu\text{m}$ and a maximum deviation of $0.062\ \mu\text{m}$ in a time interval of $2\ \mu\text{s}$. The most difficult approximation is observed with the harmonic load with a maximum error of $0.1471\ \mu\text{m}$ and a critical deviation of $5.547\ \mu\text{m}$ at $4\ \mu\text{s}$ after $200\Delta\tau$. Direct comparisons between the errors

and deviations are made in the interval time from $0 \mu\text{s}$ to $1.7 \mu\text{s}$ equivalent to $85\Delta\tau$ for these three cases. The partial error at $1.7 \mu\text{s}$ for the harmonic case is $0.15 \mu\text{s}$, which is the highest error between all the cases. The ramp load shows smaller values and slower variations of errors and deviations compared with the other two boundary conditions.

4.2.3 Mesh and time step dependency

The simulations presented in the subsection 4.2.2, the number of dual reciprocity points (DRPs) coincides with the number of physical nodes used in the problem. In this work, internal points are not included in the model. The dynamic BEM formulation is sensitive to the mesh refinement and time step. Therefore, it is useful to analyze the changes in numerical response for different number of boundary elements in the discretization and time step values. It is considered the 45 grain specimen shown in Figure 4.10, where $L = 0.5 \text{ mm}$ and a step load is applied with $\sigma(t) = 100 \text{ MPa}$ Figure 4.10(b).

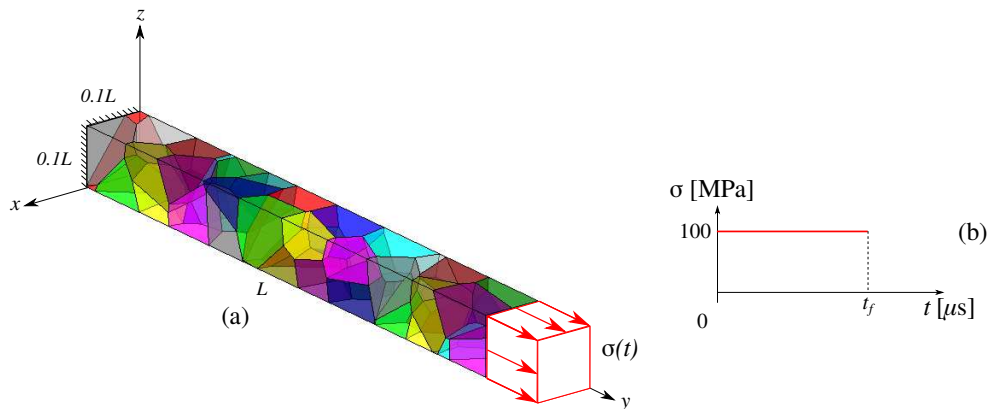


Figure 4.10: (a) Physical model of 180 grains, $L = 0.5 \text{ mm}$ and (b) step load.

The mesh dependency, in terms of elements and DRPs is evaluated for three 45 grain specimens generated with different mesh refinement levels, Figure 4.11.

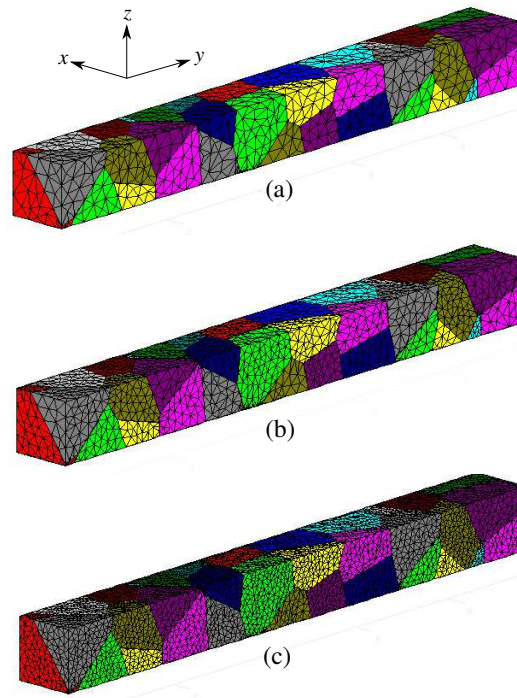


Figure 4.11: Number of elements: (a) mesh I: 4,775, (b) mesh II: 8,332, and (c) mesh III: 14,922.

The time step dependency is also observed using three different time steps for each mesh Table 4.15.

$\Delta\tau$ [ns]	<i>Time steps</i>
40	25
30	33
20	50

Table 4.15: Simulation times.

In this case, Cu is used for all the simulations. A set of 10 distributions of crystalline planes is assigned for each mesh in order to guarantee feasible comparisons with the same constitutive material. Thus, for each specimen, 10 values of y -displacement at $L = 0.5$ mm are obtained. The mean values of y -displacement (\bar{u}_y) are computed and compared with the analytical solution, Equation (4.18).

Figures 4.12, 4.13, and 4.14 present results of \bar{u}_y for $\Delta t = 40\text{ns}$, $\Delta t = 30\text{ns}$, and $\Delta t = 20\text{ns}$, respectively. These tests are developed only to analyze the behavior and convergence. In order to improve them compared with the exact solution, more samples must be considered for this analysis.

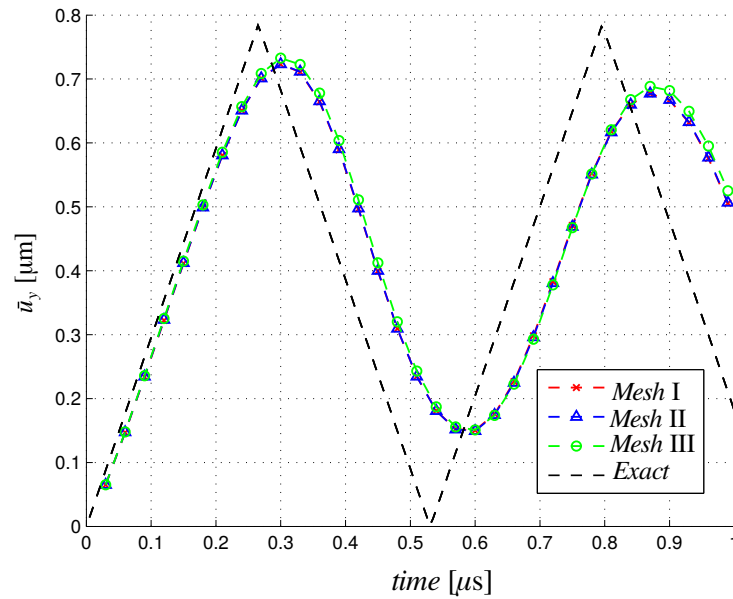


Figure 4.12: Comparison among y -displacements of meshes I, II, and III with $\Delta\tau = 40\text{ ns}$.

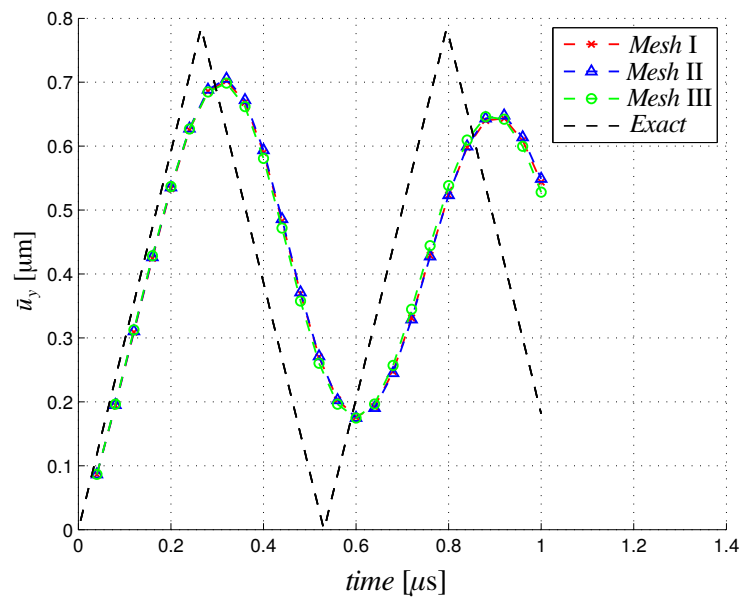


Figure 4.13: Comparison among y -displacements of meshes I, II, and III with $\Delta\tau = 30\text{ ns}$.

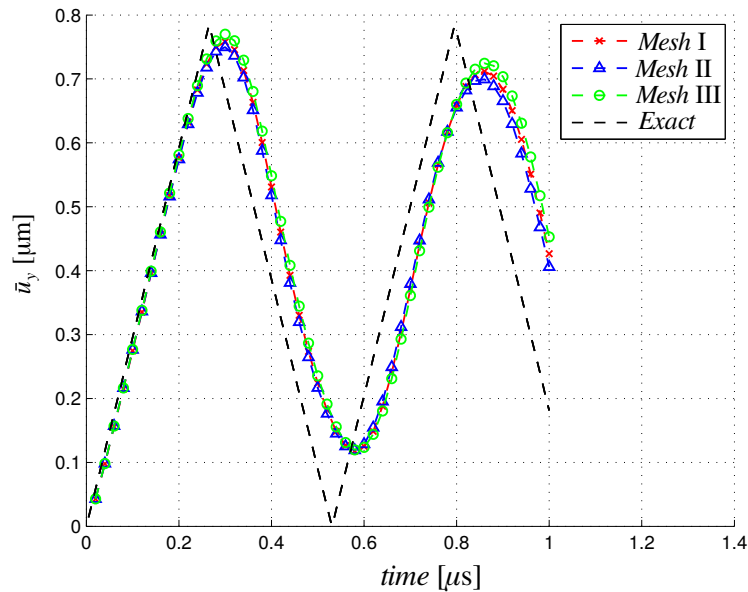


Figure 4.14: Comparison among y -displacements of meshes I, II, and III with $\Delta\tau = 20$ ns.

From these tests, the response does not change when the number of elements increases from 4,775 to 3,557 in mesh II and to 10,147 elements in mesh III. The change in time step has a more significant influence on the response. When the time step decreases Figure 4.14, the \bar{u}_y is closer to the analytical solution than the case when the time step increases Figure 4.12.

4.3 Computational aspects

The computational simulations were carried out on a distributed architecture memory platform using MPI-Fortran. As mentioned before, the main BEM implementation requires some parallelized sections, such as the evaluation of the matrix of interfaces, the computation of the incidence BEM matrices and the solver of the linear system of equations. All simulations were executed in the *Kahuna cluster* from the Center for Computational Engineering and Science at the University of Campinas (CCES/UNICAMP), for details of the cluster composition, see http://www.escience.org.br/computing_resources.

In total, 1450 simulations were executed, 1200 for the analysis of the effective macroscopic properties, and 240 in the dynamic behavior study. The number of the available simultaneous three-

ads is 256. In the simulations of the macroscopic properties: i) specimens of 18, 36 and 60 grains were run using groups of 32 threads with 40 GB of memory, each one for a specimen sample, being possible to run eight samples simultaneously. ii) For specimens with 100 and 150 grains, more memory were required, being necessary to run each sample in a group of 128 threads with 120 GB of memory each group, where two simultaneous samples are executed at the same time. ii) The most critical case is the specimen of 210 grains. The samples were executed in a single machine with high RAM. For these simulations, a 64 threads machine was used, being possible only the execution of one sample at the same time. For this last case, the time for run one realization (six boundary conditions) were approximately 6 h 29 min 26 s. The mean time spent by MUMPS to solve the system of equations according to the DOF given in Table 4.2 were approximately 3893 s. Finally, the mean time required for computing the 210 the \mathbf{H}^g and \mathbf{G}^g matrices was around of 899s.

The 240 dynamic behavior simulations were run on a group of 32 threads with 40 GB. These dynamic simulations required a small computational source for 180 grains compared with the simulations of the effective macroscopic properties. The reason is the shape of the long cantilever bar used, Figure 4.5. The final system of equation for the dynamic behavior simulations is more sparse than the system for the macroscopic properties. Hence, it was possible to run 8 samples simultaneously.

5 Grain boundary model

The failure analysis of GBs in the polycrystal aggregates has been the object of study through continuum, atomistic or multiscale approaches. The modeling of this failure condition requires a complex and detailed analysis of GBs that represents the transition region between two grains with distinct crystalline orientations. In this chapter, the atomistic modeling of GBs is presented using LAMMPS, where the GBs are analyzed for several configurations. First, the MD formulation implemented in LAMMPS is described. Then, as a validation, the evaluation of the GB energy as function of the crystalline orientation angle is presented for bcc materials.

5.1 Molecular dynamics

The atomistic simulations consist in the description of the positions and thermodynamic state of a system composed by thousand of atoms in a specific instant of time. The system is generally solved by molecular dynamics, that is a deterministic method to evaluate the positions $\{\mathbf{x}_i, \dots, \mathbf{x}_N\}$ and the velocities $\{\mathbf{v}_i, \dots, \mathbf{v}_N\}$ of the system, where both are known at the initial time t_i . In order to evaluate the time evolution and following the descriptions presented in (GRIEBEL ET AL., 2010; LEIMKUHNER AND MATTHEWS, 2015), the Hamiltonian of the system is expressed as

$$\mathcal{H} = E_k + U \quad . \quad (5.1)$$

In Equation (5.1), E_k and U are the kinetic and potential energies of the system respectively. The evolution can be described by the Hamilton's equation of motion expressed in terms of generalized coordinates \mathbf{q}_i and conjugate momenta \mathbf{p}_i given by

$$\dot{\mathbf{q}}_i = \nabla_{\mathbf{p}_i} \mathcal{H}, \quad \dot{\mathbf{p}}_i = -\nabla_{\mathbf{x}_i} \mathcal{H}, \quad i = 1, \dots, N \quad , \quad (5.2)$$

where the “ (\cdot) ” denotes the partial derivative with respect to the time. There are distinct mathematical ways to derive the relations shown in Equation (5.2), see (GOLDSTEIN ET AL., 2002). Generally, it is considered the interactions between atoms as characterized by the gradient of a con-

servative potential $U = U(\mathbf{x}_1, \dots, \mathbf{x}_N)$, which is not explicitly dependent on the time. If cartesian coordinates and velocities are used, the Hamiltonian is

$$\mathcal{H}(\mathbf{x}_1, \dots, \mathbf{x}_N, \mathbf{p}_1, \dots, \mathbf{p}_N) = \sum_{i=1}^N \frac{\mathbf{p}_i^2}{2m_i} + U(\mathbf{x}_1, \dots, \mathbf{x}_N) \quad . \quad (5.3)$$

The momenta is given by $\mathbf{p}_i = m_i \mathbf{v}_i$, where m_i is the atomic mass. From the Equation (5.2) the Newton's equation of motion can be derived as

$$\dot{\mathbf{x}}_i = \dot{\mathbf{v}}_i, \quad m_i \ddot{\mathbf{x}}_i = \mathbf{F}_i, \quad i = 1, \dots, N \quad , \quad (5.4)$$

where the forces \mathbf{F}_i , only depend on the coordinates and are given by $\mathbf{F}_i = -\nabla_{\mathbf{x}_i} U_i(\mathbf{x}_1, \dots, \mathbf{x}_N)$. The evolution of the atomistic system is accomplished by solving the differential Newton's equation in a discrete time, using integration methods to find the new values of the position and velocity vectors at t_{i+1} after one time step δt . Frequently, the atomistic 3D domain of these models is assumed as a box with dimensions L_x , L_y and L_z . The periodicity of crystalline materials offers the advantage to imposed periodic boundary conditions to the system. This allows to compensate the computational limitations of the numerical simulation. A representation of periodic boundary conditions is illustrated in Figure 5.1.

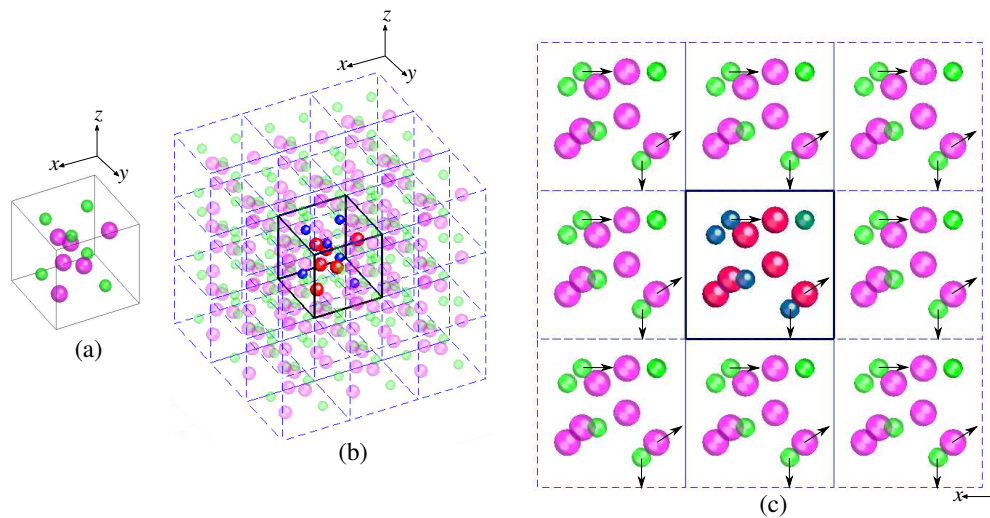


Figure 5.1: Periodic boundary conditions: (a) cell, (b) super cell and (c) simulation domain.

The cell shown in Figure 5.1(a), is replicated in its all three dimensions as shown in Figure 5.1(b). Hence, surface effects are avoided and better interactions between the domain and the surrounding media are reproduced applying periodic boundary conditions. The atoms that leave the domain by one site enter by the opposite and also atoms located close to the opposite sites of the domain interact with each other, Figure 5.1(c). Other types of boundary conditions are described in (GRIEBEL ET AL., 2010).

5.1.1 Energy minimization

The energy minimization is an important task to reach the structural relaxation and stable equilibrium of the atomistic system. Commonly, atomic arrangements are generated from its equilibrium configuration after the fitting process of the interatomic potential. This situation occurs in case of absence of defects or discontinuities in the domain of the system. Realistic atomic systems in the nature are not perfect, e.g. the discontinuities and broken bounds presented in the grain boundaries of polycrystalline materials. Owing to the dependency of the potential energy on the atomic positions, the imperfections in the structure configuration can cause specific atomic positions where the evaluation of the potential energy results in very high values.

In order to find the minimum ground state of the atomistic system, several computational methods were proposed in the literature to optimize the potential energy function. Methods such as, the steepest descents, Quick-min, Fast inertial relaxation engine, conjugate gradient, Broyden-Fletcher-Goldfard-Shanno (L-BFGS) and the global L-BFGS (GL-BFGS). These methods are force-based optimizers. Sheppard et al. (2008), presents in a review an extensive comparison between the mentioned methods for finding minimum energy paths. Additionally, more classical methods can be mentioned to carry out energy minimization such as Newton-Raphson, quasi-Newton or truncated-Newton methods (BITZEK ET AL., 2006). The most commonly method used for energy minimization of atomistic systems is the conjugate gradient (CG) using the Polak-Ribière formula (POLAK AND RIBIÈRE, 1969; PRESS ET AL., 1992), due to its efficiency to convergence.

Considering that the coordinates \mathbf{r}_i of the N atoms in the system are contained in a vector \mathbf{x} of $3N$ components, as

$$\mathbf{x} = (\mathbf{r}_1, \mathbf{r}_2, \dots, \mathbf{r}_N) \quad . \quad (5.5)$$

The function to be minimize is the potential energy $U(\mathbf{x})$, the most rapidly change in the function is determined by the gradient. The approximation of the potential function by a Taylor series around the point \mathbf{P} , as the origin of the coordinate system with coordinates \mathbf{x} is, written as

$$U(\mathbf{x}) = U(\mathbf{P}) + \nabla U(\mathbf{P}) \cdot \mathbf{x} + \frac{1}{2} \mathbf{x}^T \cdot \mathbf{H}(\mathbf{P}) \cdot \mathbf{x} + \dots \quad , \quad (5.6)$$

where $\mathbf{H}(\mathbf{P}) = \nabla \nabla U(\mathbf{P})$ is the Hessian matrix. If $c \equiv U(\mathbf{P})$ and $\mathbf{b} \equiv -\nabla U(\mathbf{P})$, the Equation (5.6) takes the following form

$$U = c - \mathbf{b} \cdot \mathbf{x} - \frac{1}{2} \mathbf{x}^T \cdot \mathbf{H} \cdot \mathbf{x} \quad . \quad (5.7)$$

The gradient of the potential function is calculated from Equation (5.7), as

$$\nabla U = \mathbf{H} \cdot \mathbf{x} - \mathbf{b} \quad . \quad (5.8)$$

The minimization implies that the gradient will vanish, being the function goes to an extreme. The change in the gradient over some direction is $\delta \nabla U(\mathbf{x}) = \mathbf{H} \cdot \delta \mathbf{x}$. Now, supposing that the direction where the function previously moved to a minimum is \mathbf{u} and it is perpendicular to the gradient, then $\nabla U(\mathbf{x}) \cdot \mathbf{u} = 0$. The next movement is over some direction \mathbf{v} . It indicates that the change of the gradient is expressed by $\delta \nabla U(\mathbf{x}) \cdot \mathbf{v} = 0$. In order to maintain an efficient minimization, it is required that, for the new direction vector \mathbf{v} the gradient of the potential function remains perpendicular to \mathbf{u} , hence $\mathbf{u}^T \cdot \mathbf{H} \cdot \mathbf{v} = 0$. The vectors \mathbf{u} and \mathbf{v} that follows the last properties are conjugate. The CG method initializes the search in the direction of the force, $\mathbf{d}_0 = \mathbf{F}_0$. Furthermore, two vectors are defined as $\mathbf{g}_0 = \mathbf{d}_0$ and $\mathbf{h}_0 = \mathbf{d}_0$ where \mathbf{h}_0 is the actual direction. In order to calculate the new direction in which to move, it is used the equations presented in (PRESS ET AL., 1992) as follows

$$\mathbf{g}_{i+1} = \mathbf{g}_i - \lambda_i(\mathbf{H} \cdot \mathbf{h}_i) \quad \text{and} \quad \mathbf{h}_{i+1} = \mathbf{g}_{i+1} + \gamma_i \mathbf{h}_i \quad , \quad (5.9)$$

these vectors satisfy the orthogonality and conjugacy conditions

$$\mathbf{g}_i \cdot \mathbf{g}_j = 0 \quad \mathbf{h}_i^T \cdot \mathbf{H} \cdot \mathbf{h}_j = 0 \quad \mathbf{g}_i \cdot \mathbf{h}_j = 0 \quad \text{for } j < i \quad . \quad (5.10)$$

In the Equation (5.9) the scalars λ_i and γ_i are equal to

$$\lambda_i = \frac{\mathbf{g}_i \cdot \mathbf{h}_i}{\mathbf{h}_i^T \cdot \mathbf{H} \cdot \mathbf{h}_i} \quad , \quad (5.11)$$

$$\gamma_i = \frac{\mathbf{g}_{i+1} \cdot \mathbf{g}_{i+1}}{\mathbf{g}_i \cdot \mathbf{g}_i} \quad . \quad (5.12)$$

For atomistic simulations, it is no recommended to evaluate the Hessian matrix, due to its N^2 order. Therefore, there is a variation of the CG method that works without the evaluation of the Hessian matrix \mathbf{H} . This is, if the potential function U is minimized in the direction of \mathbf{h} to some point $\mathbf{x}_{i+1} = \mathbf{r}_i + \alpha \mathbf{d}_i$, the new \mathbf{g} can be obtained as

$$\mathbf{g}_{i+1} = -\nabla U(\mathbf{r}_i + \alpha \mathbf{d}_i) \quad . \quad (5.13)$$

Hence, the algorithm starts with the initial state \mathbf{r}_0 , $U^0 = U(\mathbf{r}_0)$, $\mathbf{F}_0 = -\nabla U(\mathbf{r}_0)$, $\mathbf{g}_0 = \mathbf{F}_0$ and $\mathbf{h}_0 = \mathbf{F}_0$. Then, the algorithm is defined by the following steps

- 1** First, the minimization of $U(\mathbf{r}_i + \alpha \mathbf{F}_i)$ is carried out respect to the scalar α , then $U^{i+1} = U(\mathbf{r}_{i+1})$.
- 2** If $U^{i+1} - U^i < \text{error}$, quit.
- 3** Calculate $\mathbf{F}_i = -\nabla U(\mathbf{r}_{i+1})$ and $U^i = U(\mathbf{r}_{i+1})$.

4 Set $\mathbf{g}_{i+1} = \mathbf{F}_i$ and evaluate γ using the Polak Rebière definition

$$\gamma = \frac{(\mathbf{g}_{i+1} - \mathbf{g}_i) \cdot \mathbf{g}_{i+1}}{\mathbf{g}_i \cdot \mathbf{g}_i} . \quad (5.14)$$

5 Evaluate $\mathbf{h}_{i+1} = \mathbf{g}_{i+1} + \gamma \mathbf{h}_i$ and set $\mathbf{F}_{i+1} = \mathbf{h}_{i+1}$.

6 Return to 1 for the next iteration.

If the minimization is carried out along a set of conjugate directions, the above algorithm will be very efficient to find a local minimum.

5.1.2 Time integration method

The solution of the Newton's equation of motion is carried out by discretization of the continuum problem into a finite number of time steps δt to transform the differential equation into a system of equations. Thus, the solution consists on the evaluation of the state of the system at the specific time t_n from the initial condition at t_0 , through subintervals with the same size up to t_N , where $n = 1, 2, \dots, N$. Methods to integrate the differential equation are generally based on finite differences. An efficient and stable scheme for the time discretization of the Newton's equation is the Verlet algorithm (VERLET, 1967) some other methods were also proposed in (TUCKERMAN AND BERNE, 1992; HUMPHREYS ET AL., 1994).

The integration methods require some characteristics for the analysis of atomistic systems, such as: i) the accuracy when large time steps δt are used, ii) the computational speed needed to carry out the integration over the thousand of atoms, iii) the energy conservation that depends on the reversibility of equation of motion and the constant volume. In MD simulations, the energy conservation could be affected by the arithmetic operations performed with finite accuracy (typically in double precision with relative accuracy of the order 10^{-16}). Furthermore, the calculation of the interatomic forces, which usually ignores interactions beyond a cutoff. Hence, the forces are not accurate. These problems can affect the energy conservation in MD simulations. An extensive study of energy conservation was presented by Toxvaerd et al. (2012).

In order to derive the Verlet algorithm, consider the first derivative of the atomic position \mathbf{x}_i

of the i th atom respect to the time, expressed in terms of the central difference operator at the grid point t_n as

$$\dot{\mathbf{x}}_i(t_n) = \frac{\mathbf{x}_i(t_n + \delta t) - \mathbf{x}_i(t_n - \delta t)}{2\delta t} . \quad (5.15)$$

The Taylor expansion of the right-hand side terms in Equation (5.15) around both instants $t_n + \delta t$ and $t_n - \delta t$ up to the second order gives

$$\mathbf{x}_i(t_n + \delta t) = \mathbf{x}_i(t_n) + \delta t \dot{\mathbf{x}}_i(t_n) + \frac{1}{2} \delta t^2 \ddot{\mathbf{x}}_i(t_n) + \mathcal{O}(\delta t^3) , \quad (5.16)$$

$$\mathbf{x}_i(t_n - \delta t) = \mathbf{x}_i(t_n) - \delta t \dot{\mathbf{x}}_i(t_n) + \frac{1}{2} \delta t^2 \ddot{\mathbf{x}}_i(t_n) - \mathcal{O}(\delta t^3) . \quad (5.17)$$

By substituting the Equations (5.16) and (5.17) into the Equation (5.15) the order of accuracy of the discretization is $\mathcal{O}(\delta t^2)$ in the approximation of the first derivative. This approximation using the central difference operator compared with the forward or backward differences results in a discretization error of $\mathcal{O}(\delta t)$. Applying the Equation (5.15) for the first derivative of the terms $\mathbf{x}_i(t_n + \delta t)$ and $\mathbf{x}_i(t_n - \delta t)$, the second derivative $\ddot{\mathbf{x}}$ around the instant t_n is expressed by

$$\ddot{\mathbf{x}}_i(t_n) = \frac{\mathbf{x}_i(t_n + \delta t) - 2\mathbf{x}_i(t_n) + \mathbf{x}_i(t_n - \delta t)}{\delta t^2} . \quad (5.18)$$

A similar analysis can be used for the second derivative $\ddot{\mathbf{x}}$, by the Taylor expansion up to the third order of both instants $t_n + \delta t$ and $t_n - \delta t$, then substituting into the Equation (5.18), the order of accuracy in this case is also $\mathcal{O}(\delta t^2)$, see (GRIEBEL ET AL., 2010). Now, using the Equations (5.18) and (5.4), the positions at time t_{n+1} from the positions at time t_n and t_{n-1} and the forces at time t_n can be evaluated. Defining $\mathbf{x}_i^n = \mathbf{x}_i(t_n)$ and also for \mathbf{v}_i and \mathbf{F}_i , the motion equation in terms of positions and forces is

$$m_i \frac{1}{\delta t^2} (\mathbf{x}_i^{n+1} - 2\mathbf{x}_i^n + \mathbf{x}_i^{n-1}) = \mathbf{F}_i^n , \quad (5.19)$$

where, an expression for the positions at time t_{n+1} is written as

$$\mathbf{x}_i^{n+1} = 2\mathbf{x}_i^n - \mathbf{x}_i^{n-1} + \frac{\delta t^2}{m_i} \mathbf{F}_i^n . \quad (5.20)$$

The velocity can be evaluated as the derivative of the position at time t_{n+1} using the Equation (5.15) as follows

$$\mathbf{v}_i^n = \frac{\mathbf{x}_i^{n+1} - \mathbf{x}_i^{n-1}}{2\delta t} . \quad (5.21)$$

This version of the Verlet method has disadvantages, due to the necessity of the initial \mathbf{x}^0 and the first \mathbf{x}^1 time positions. Furthermore, the possibility of large rounding errors in the addition of quantities with very different size such as presented in Equation (5.20) because the computation of the very small quantity δt^2 (GRIEBEL ET AL., 2010). There are variants of the original Verlet method (VERLET, 1967) to reduce the rounding errors, and the requirement of two last time steps into one. The leapfrog scheme (HOCKNEY, 1970) considers the calculation of the velocities at time $t_n + 1/2$ from the velocities at time $t_n - 1/2$ and the forces at t_n , Equation (5.22).

$$\mathbf{v}_i^{n+1/2} = \mathbf{v}_i^{n-1/2} + \frac{\delta t}{2m_i} \mathbf{F}_i^n . \quad (5.22)$$

Here, the positions are given at time $t + \delta t$ Equation (5.23), in terms of the positions at the current time step t_n and the velocities computed by Equation (5.22).

$$\mathbf{x}_i^{n+1} = \mathbf{x}_i^n + \delta t \mathbf{v}_i^{n+1/2} . \quad (5.23)$$

Applying the last two equations, it is observed the minimization of the presence of rounding errors compared to the Equation (5.20). This second version of the Verlet method has a disadvantage to evaluate the kinetic and potential energies at the same time t_n . A second variant is the so-called velocity Verlet method (SWOPE ET AL., 1982). This algorithm eliminates the half-step velocity problem. Substituting the acceleration field $\mathbf{x}_i^n = \mathbf{F}_i^n / m_i$ into the Equation (5.16), the following

equation is obtained

$$\mathbf{x}_i^{n+1} = \mathbf{x}_i^n + \delta t \mathbf{v}_i^n + \delta t^2 \frac{\mathbf{F}_i^n}{2m_i} . \quad (5.24)$$

Analogously, the Taylor expansion for the velocity up to the second order is

$$\mathbf{v}_i^{n+1} = \mathbf{v}_i^n + \delta t \dot{\mathbf{v}}_i^n + \frac{1}{2} \delta t^2 \ddot{\mathbf{v}}_i^n . \quad (5.25)$$

Substituting the second derivative of the velocity $\ddot{\mathbf{v}}_i^n$ by its expression in terms of the forward differences into the Equation (5.25) yields

$$\mathbf{v}_i^{n+1} = \mathbf{v}_i^n + \frac{1}{2} (\dot{\mathbf{v}}_i^n + \dot{\mathbf{v}}_i^{n+1}) , \quad (5.26)$$

and then

$$\mathbf{v}_i^{n+1} = \mathbf{v}_i^n + \frac{(\mathbf{F}_i^n + \mathbf{F}_i^{n+1}) \delta t}{2m_i} . \quad (5.27)$$

The velocity Verlet method uses the half time step as a predictor-corrector step. This is, first the force field is evaluated at t_0 using the reference positions \mathbf{x}_i^0 , thus the next positions \mathbf{x}_i^1 are calculated by Equation (5.24). Now, the velocity for a predictor stage can be computed for a half time step $\mathbf{v}_i^{1/2}$ using the following equation

$$\mathbf{v}_i^{n+1/2} = \mathbf{v}_i^n + \frac{\mathbf{F}_i^n \delta t}{2m_i} , \quad (5.28)$$

hence, the new \mathbf{F}_i^1 force field can be evaluated. Finally, the correction for the velocity in a complete time step \mathbf{v}_i^1 is given by

$$\mathbf{v}_i^{n+1} = \mathbf{v}_i^{n+1/2} + \frac{\mathbf{F}_i^{n+1} \delta t}{2m_i} . \quad (5.29)$$

For illustrative purposes, the velocity Verlet algorithm is presented step by step in the next table

1 st	$\mathbf{F}_i^n = -\nabla_{\mathbf{x}_i} U_i(\mathbf{x}_i^n)$
2 nd	$\mathbf{x}_i^{n+1} = \mathbf{x}_i^n + \delta t \mathbf{v}_i^n + \frac{\mathbf{F}_i^n \delta t^2}{2m_i}$
3 rd	$\mathbf{v}_i^{n+1/2} = \mathbf{v}_i^n + \frac{\mathbf{F}_i^n \delta t}{2m_i}$
4 th	$\mathbf{F}_i^{n+1} = -\nabla_{\mathbf{x}_i} U_i(\mathbf{x}_i^{n+1})$
5 th	$\mathbf{v}_i^{n+1} = \mathbf{v}_i^{n+1/2} + \frac{\mathbf{F}_i^{n+1} \delta t}{2m_i}$

Table 5.1: Velocity Verlet algorithm.

All three variants for the Verlet algorithm needs almost the same amount of memory $9N$.

5.1.3 Interatomic potentials

The atomistic modeling considers the evaluation of the force field in an instant of time in the system. The force field is characterized by the gradient of a potential energy $U(\mathbf{x})$ that is a function of the atomic positions. Initially, the potential energy was based only on the interaction between two atoms called pair potential $V(\mathbf{x})$. Some classical pair potentials can be found in the literature, such as the Lennard-Jones and Morse or the van der Waals potentials as described in (GRIEBEL ET AL., 2010). In pair potentials, atomistic bonds are treated independently from each other, which is an approximation with the advantage of simple expressions. For metallic materials, it is not recommended to use basic pair potentials to evaluate the force field, owing to the lack of considerations of additional physical effects. Comparisons of simulations based on realistic N -body potentials with simple pair potentials are presented by Ziegenhain et al. (2009), for the analysis of nano-indentations.

The most common N -body potentials used for metallic materials are the embedded atom method (EAM) (DAW AND BASKES, 1983) and the Finnis-Sinclair (FS) (FINNIS AND SINCLAIR, 1984) potentials. These potentials are composed by a repulsive pair potential $V(\mathbf{x})$ and an attractive function f , that contemplates the surrounding effects at the i th atom. The total potential energy of the system is expressed as

$$U = \sum_{i=1}^{N-1} \sum_{j=i+1}^N V(r_{ij}) + \sum_{i=1}^N f(\rho_i) \quad , \quad (5.30)$$

where f is an embedded function and ρ_i is the local electronic charge density at i th atom. Hence, it is constructed as the summation over its all corresponding neighbor j th atoms, then

$$\rho_i = \sum_j \phi(r_{ij}) \quad . \quad (5.31)$$

The form of the embedded function depends on the type of N -body potential. As shown in Equations (5.30) and (5.31), both $V(r_{ij})$ and $\phi(r_{ij})$ are dependent on the interatomic distance $r_{ij} = |\mathbf{r}_{ij}| = |\mathbf{r}_j - \mathbf{r}_i|$. The electronic density ρ_i is defined as the rigid superposition of the atomic charge densities ϕ . The energy of the atom at site i is then assumed to be, the same as if it would be inside of a uniform electron gas of that density. The attractive part of the FS potential was based on the results of tight-binding theory (FINNIS AND SINCLAIR, 1984), while the EAM potential regards the Hartree-Fock calculations, this is the reason on the difference of the function f in each potential. In this work, a bcc Fe material is considered in the analysis using the EAM potential proposed by Mendeleev et al. (2003). The functional form of the pair potential part is shown in Equation (5.32).

$$V(r) = k \frac{Z^2 q_e^2}{r} \varphi \left(\frac{r}{r_s} \right) H(r_1^* - r) + \exp^{(B_0 + B_1 r + B_2 r^2 + B_3 r^3)} H(r - r_1^*) H(r_2^* - r) + \sum_{k=1}^{15} a_k (r_k - r)^3 H(r_k - r) H(r - r_2^*) \quad , \quad (5.32)$$

where k is the Coulomb's constant, Z is the atomic number and q_e is the atomic charge on an electron. Details of these pair potential functions are explained in (BIERSACK AND ZIEGLER, 1982; ACKLAND ET AL., 1997). The remaining terms r_s and φ are

$$r_s = 0.88534 \frac{r_B}{2^{1/2} Z^{1/3}} \quad , \quad (5.33)$$

and

$$\begin{aligned} \varphi(x) = & 0.1818 \exp(-3.2x) + 0.5099 \exp(-0.9423x) + \\ & 0.2802 \exp(-0.4029x) + 0.02817 \exp(-.2016x) \quad , \quad (5.34) \end{aligned}$$

being r_B the Bohr radius. This EAM potential uses the form for the density function as shown in Equation (5.35).

$$\phi(r) = \sum_{k=1}^{15} A_k (R_k - 1)^3 H(R_k - r) \quad . \quad (5.35)$$

The embedded function takes the form as follows

$$f(\rho_i) = -\sqrt{\rho_i} + a^* \rho_i^2 \quad . \quad (5.36)$$

In this case, $r_1 < r_2 < \dots < r_{15}$ and $R_1 < R_2 < R_3$. The cut-off radii for V and ϕ are r_{15} and R_3 respectively. Furthermore, this potential considers the ion-ion interaction as shown in Equation (5.32), when $r < r_1^*$ for $r_1^* = 0.95 \text{ \AA}$, using the screened-Coulomb potential (BIERSACK AND ZIEGLER, 1982). For the second interval $r_1^* < r < r_2^*$, where $r_1^* = 1.95$ an exponential function is used. Finally, for $r > r_2^*$, a cubic spline function is employed. The coefficients a_k , r_k , A_k , R_k , B_k and a^* are given in the Appendix C.1. As mentioned, the gradient of the potential function gives the force between two individual atoms. According to the Equation (5.30), the atomistic force can be computed by

$$\mathbf{F}_i = \sum_{j=1, i \neq j}^N \left\{ \frac{dV(r_{ij})}{dr} + [f'(\rho_i) + f'(\rho_j)] \frac{d\rho_i(r_{ij})}{dr} \right\} \frac{\mathbf{r}_{ij}}{r_{ij}^2} . \quad (5.37)$$

The resulting force on the i th atom is obtained by the summation over all j th neighbor atoms inside the cutoff radius defined by the potential. The evaluation of this force regards the effects of the electronic density between the two atoms. Then, the force on the i th atom depends on the surrounding atoms. It requires a previous computation of the electronic density for each atom ρ_i and ρ_j . Due to the N -body character of these potentials and according to the radii presented in Table C.1.1, the behavior can be plotted in terms of the ratio r/a , where a is the lattice parameter. The maximum ratio r/a is 2.101 working up to the sixth nearest neighbor atoms. Figure 5.2 presents the corresponding potential of an i th atom U_i given in eV in terms of the ratio r/a .

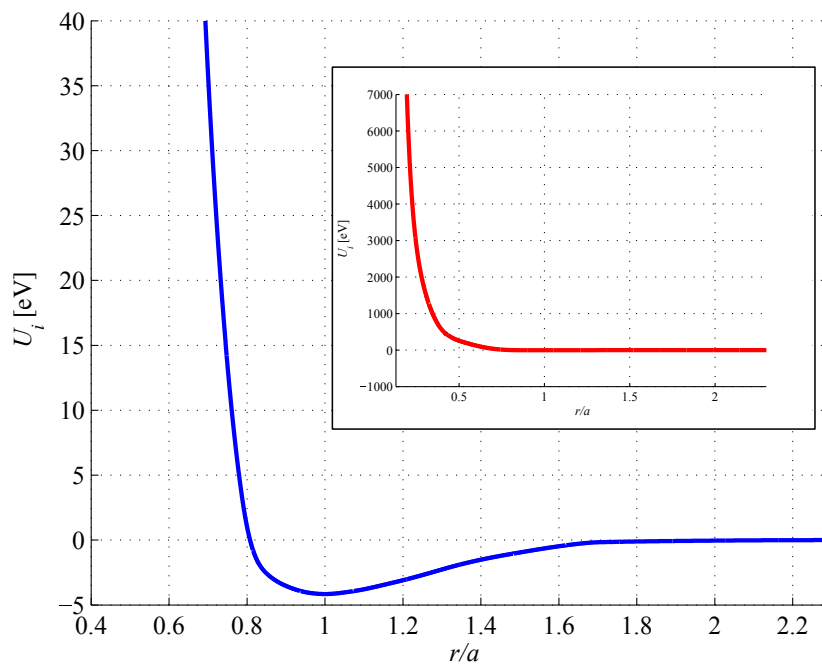


Figure 5.2: EAM Potential for Fe.

As results from the fitting process (MENDELEV ET AL., 2003), the lattice parameter a is 2.855 Å and the cohesive energy E_c is 4.1341 eV. This energy occurs when the ratio a/r is 1, that corresponds with the equilibrium state of a perfect structure. The potential energy between atoms when the ratio a/r is less than the equilibrium lattice distance, is reasonable evaluated by

the screened-Coulomb and exponential potentials shown in Equation (5.32). This fact presents an advantage when compared to more basic interatomic potentials.

5.1.4 Stress tensor

The evaluation of the macroscopic stress tensor takes into account the conjunct of microstates, positions \mathbf{x}_i and velocities \mathbf{v}_i , computed by the MD simulation. These microstates are related to the macroscopic thermodynamic variables such as the temperature and pressure of the physical problem, evaluated using statistical mechanics. For a system with a large number of atoms, regarding the canonical thermodynamical ensemble (NVT), where the number of atoms N , temperature T and the volume V remain constant in the system. The global stress tensor \mathbf{S} can be established as

$$\mathbf{S} = \frac{1}{V} \left\langle \sum_{i=1}^N m_i \mathbf{v}_i \otimes \mathbf{v}_i + \mathbf{W}(\mathbf{r}) \right\rangle , \quad (5.38)$$

where the brackets “ $\langle \dots \rangle$ ” denote the average of the canonical ensemble (NOSÉ, 1984) to evaluate the macrostate from the all microstates. In the first term, m_i and \mathbf{v}_i are the mass and instant velocity of the i th atom respectively. Furthermore, the kinetic energy term is derived from the corresponding thermodynamic average using the state equation (GOLDSTEIN ET AL., 2002). The second term of the Equation (5.38) is the global Virial tensor, that quantifies the contribution of the forces acting between atoms. The Virial tensor can be derived from different schemes depending on the application. For the case of periodic systems, the Virial tensor is related to the change on the volume V of the atomic super cell, Figure 5.1. This means, from (HÜNENBERGER, 2002; OLIVA AND HÜNENBERGER, 2002) the Virial can be expressed as

$$W(\mathbf{r}) = -3V \frac{dU}{dV} . \quad (5.39)$$

The Virial depends only on the instantaneous atomistic positions $\mathbf{r} = \mathbf{r}_1, \dots, \mathbf{r}_N$ and the interaction between them. In this derivation, the interatomic potential represents the contribution to the pressure or stress tensor. Following the analysis presented by Hummer and Gronbech-Jensen (1998), the potential energy U does not only depend on the volume. The dependence arises from

the volume scaling of the particle positions as

$$\begin{aligned} \frac{d\mathbf{r}_i}{dV} &= \frac{\mathbf{r}_i}{3V} , \\ \frac{\partial U}{\partial V} &= \sum_i \frac{\partial U}{\partial \mathbf{r}_i} \cdot \frac{\partial \mathbf{r}_i}{\partial V} = \frac{1}{3V} \sum_i \frac{\partial U}{\partial \mathbf{r}_i} \cdot \mathbf{r}_i . \end{aligned} \quad (5.40)$$

Combining the Equations (5.39) and (5.40), the expression for the stress tensor in terms of the interatomic force field and velocity is obtained as

$$\mathbf{S} = \frac{1}{V} \left\langle \sum_{i=1}^N m_i \mathbf{v}_i \otimes \mathbf{v}_i - \sum_{i=1}^N \sum_{j>i}^N \mathbf{F}_{ij} \otimes \mathbf{r}_{ij} \right\rangle . \quad (5.41)$$

Details of how LAMMPS computes the Virial for individual atoms for either pairwise or N -body potentials, including the effects of periodic boundary conditions is discussed in (THOMPSON ET AL., 2009).

5.2 Grain boundary energy

Grain boundaries have an important role in the behavior and failure analyses of polycrystalline materials, owing to the influence on the physical macroscopic properties of the material. The importance of the study of the GBs from an atomistic view is to capture the effects on different GB properties such as segregation, that contemplates the changes of concentration of additional elements as impurities in the interface. Similar to segregation, the diffusion phenomenon considers the movement of atoms in the GB (CABANÉ-BROUTY AND BERNARDINI, 1982). Other important GB processes for motion is the sliding, when the rigid translation of one grain over another parallel to the boundary interface occurs. Furthermore, the GB migration, which is the motion of the interface in the direction perpendicular to the boundary plane (BALLO, 2001). Phenomena such as the formability and fracture behavior of polycrystalline materials are influenced by the presence of second phase precipitation at the grain boundaries (STEELE ET AL., 2007). Several works in the literature (LI AND REYNOLDS, 1998; BRIANT, 2001) defined that, as the level of precipitation increases in the GBs, the fracture toughness and formability decrease affecting the overall behavior

of the material respect to the intergranular fracture. The GBs are formed during the grain growth and represent the discontinuity from the perfect crystal, being a region separating two grains of different phase. The orientations of these two grains differ from each other producing the grain boundary as a transition region, where the periodic character remains with distinct atomic position compared to the grain interior (LEJCEK, 2010).

5.2.1 GB categories

As mentioned, the mesoscale model a polycrystalline structure is built, where each grain is considered as a continuous anisotropic body with defined crystalline orientation. This fact leads to a generation of infinite oriented GBs. Therefore, it is useful to employ the crystallographic description of the two adjacent grains of the interface. Generally, the grain boundary is modeled as a bicrystal, Figure 5.3(a). A mixed GB is defined by a specimen containing the crystals *A* and *B* with the random crystalline orientation $(h_A k_A l_A)$ and $(h_B k_B l_B)$ respectively, Figure 5.3(b).

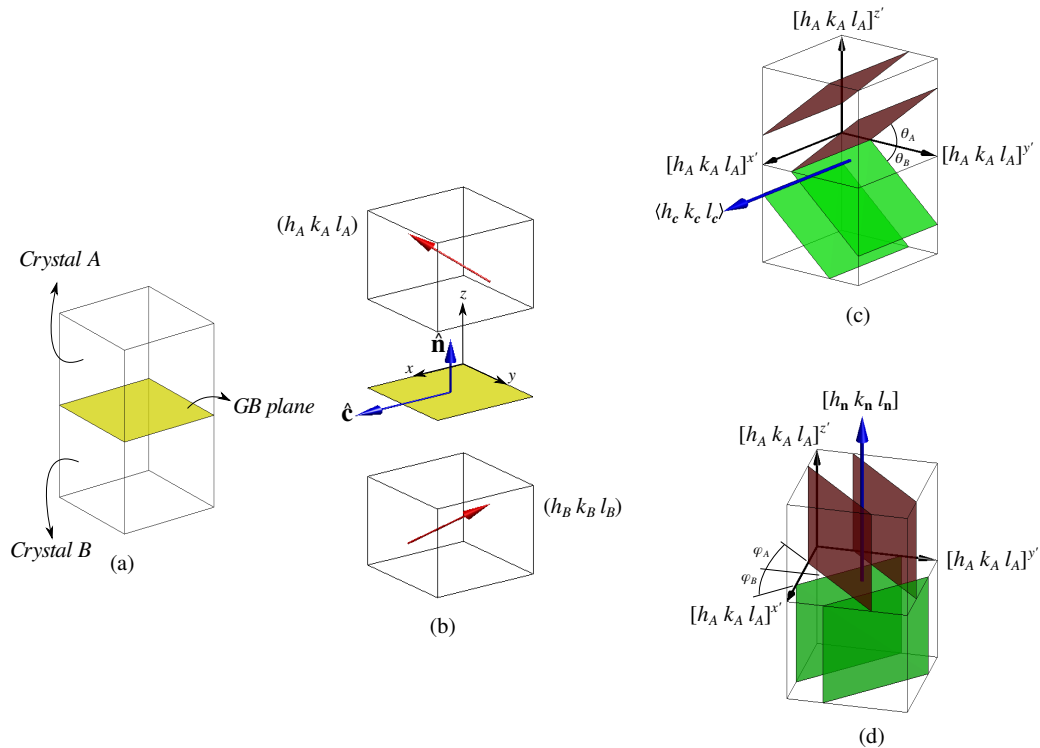


Figure 5.3: Bicrystal: (a) description, (b) mixed, (c) tilt and (d) twist GBs.

The GBs are fully characterized by the grain misorientation $\hat{c} = \langle h_c k_c l_c \rangle$ axis, which is identical in both grains. Over the \hat{c} axis, the tilt rotations θ_A and θ_B are defined in the crystals *A* and *B* respectively, Figure 5.3(c). Additionally, the GB is also described by the normal $\hat{n} = [h_n k_n l_n]$ axis, Figure 5.3(b). Over the \hat{n} axis, the twist rotations φ_A and φ_B are defined, Figure 5.3(d). All these variables completed the five DOF needed for the description of the GBs, four of them from the \hat{c} and \hat{n} axes and one given by θ or φ . The GBs are classified into, mixed, tilt and twist GBs, as presented in Figure 5.3(b-d) (LEJCEK, 2010). These three types of GBs can be also divided into five groups distinguished as follows

Symmetric tilt (STGB)	$\{h_A k_A l_A\} = \{h_B k_B l_B\}$	$\varphi_A = 0$	$\varphi_B = 0$	
Asymmetrical tilt (ATGB)	$\{h_A k_A l_A\} \neq \{h_B k_B l_B\}$	$\varphi_A = 0$	$\varphi_B = 0$	
Symmetric twist (STwGB)	$\{h_A k_A l_A\} = \{h_B k_B l_B\}$	$\varphi_A \neq 0$	$\varphi_B \neq 0$	$\varphi_A = \varphi_B$
Asymmetrical twist (ATwGB)	$\{h_A k_A l_A\} = \{h_B k_B l_B\}$	$\varphi_A \neq 0$	$\varphi_B \neq 0$	$\varphi_A \neq \varphi_B$
Mixed GB	$\{h_A k_A l_A\} \neq \{h_B k_B l_B\}$	$\varphi_A \neq 0$	$\varphi_B \neq 0$	$\varphi_A \neq \varphi_B$

Table 5.2: GB categories.

In summary, from Table 5.2, the GBs are completely described implying the existence of a large number of different GBs. In a general way, the GB can be defined by using the following notation $\theta[h_c k_c l_c](h_{nA} k_{nA} l_{nA}) / (h_{nB} k_{nB} l_{nB})$. This representation can be reduced more specifically by the relationship between the DOF, e.g. tilt GBs will occur with $\hat{c} \perp \hat{n}$ and in case of twist when $\hat{c} \parallel \hat{n}$. For symmetrical GBs the notation can be simplified as $\theta[h_c k_c l_c]\{h_n k_n l_n\}$.

5.2.2 Coincidence-Site Lattice

The CSL is a geometrical model for the identification of different types of GBs. The GBs are divided into low-angle and high-angle interfaces. It is considered the low-angle GBs as the interfaces with a misorientation angle less than 15° . Several works reported low-angle GBs, such as Rouvierea et al. (2000) that simulated twist interfaces from 0.5° to 12° . Also Gao and Jin (2017) used 3.4° tilt angle analysis of dislocation in Ni using MD simulations. Additionally, the energy of the low-angle GBs can be calculated through various analytical techniques as presented in (SHI ET AL., 1989). For both cases low and high angle GBs, the atomic arrangement of the GB maintains its different periodic character from the atomic structure inside the grains. Therefore, the GB energy

is considered higher than the energy in the crystal interior.

The CSL contemplates that the grain boundary energy is low when the coincidence of atomic positions in both adjacent grains is high, because the number of bonds that are broken across the boundary is small (FLETCHER, 1971). Other definitions consider that the state of the minimum energy occurs when the atomistic arrangement is perfect without any discontinuity, the grain boundary energy is low when more atoms coincide with the positions of the perfect crystal than in a non-coincident state. The number of coincident-sites is determined by the simply superposition of the two crystals where some atoms will coincide, this process can represent a difficult task. In the literature, the GBs are identified by the reciprocal value (Σ) of the density of coincidence sites that is important to characterize the CSL. An extended explanation of how to evaluate the Σ parameter is presented by Lejcek (2010). At first instance, the Σ values will be higher for low angle GBs.

Owing to the geometrical nature of the CSL model, some situations are observed from this concept, e.g. for 0° misorientation angle, the perfect crystal has all of its atomic positions as coincident. Therefore, in this case the description assumes the value of $\Sigma 1$ and its corresponding grain boundary energy is 0 mJ/m^2 . Another case is referred to the twin grain boundaries, that are considered as very symmetrical interfaces with low or high angles. In the bcc Fe material, almost 0 mJ/m^2 minimum energy occurs for $\Sigma 3$ when $\theta = 70.53^\circ$ while a maximum value occurs when $\theta = 109.47^\circ$, in this case its GB energy takes an approximated value of 1300 mJ/m^2 (TSCHOPP ET AL., 2012). From the literature, several tilt and twist GB energy analyses can be found for different materials, where the energy is evaluated in terms of the tilt θ or the twist φ angles (TSCHOPP ET AL., 2015; RUNNELS ET AL., 2016).

In the MD simulation of GB energy, the bicrystal model considers periodic boundary conditions. These conditions will allow to simulate the interfaces as an infinite media in all directions. Depending on the misorientation angle of each grain, the final bicrystal structure must guarantee the exactly periodicity in the x , y and z axes. In this work, the CSL bicrystal is built using the *GBstudio* available in <https://staff.aist.go.jp/h.ogawa/GBstudio/indexE.html>. This is a software developed by Ogawa (2006) for generating atomic coordinates in periodic GB models composed by two crystals. Hence, using *GBstudio* a set of STGB, ATGB, STwGB and ATwGB can be generated, where the input parameters are the lattice of the crystal structure, the mentioned five DOF of the bicrystal and the number of rotated unit cells along each axis. An illustration of a generated GB is shown in Figure 5.4. This structure represents an example of a STGB bicrystal for a cubic bcc Fe.

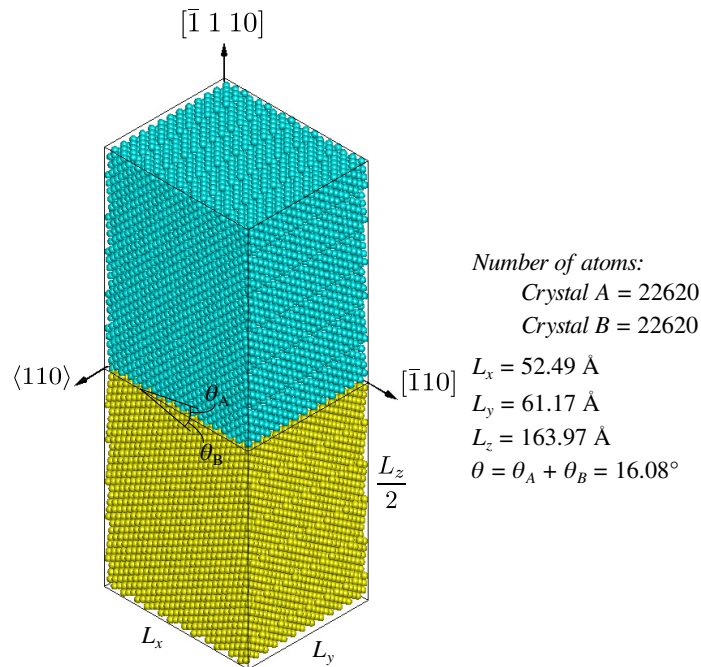


Figure 5.4: Bicrystal structure of a STGB $\Sigma 51\{1 \bar{1} 10\}$ in the $\langle 110 \rangle$ direction.

In the STGB $\Sigma 51\{1 \bar{1} 10\}$ depicted in Figure 5.4, the new axes of coordinates are $x = \langle 110 \rangle$, $y = [1\hat{1}0]$ and $z = [1 \bar{1} 10]$. In this GB, the misorientation angles are the same as $\theta_A = 8.04^\circ$ and $\theta_B = 8.04^\circ$. The normal vector of the GB plane is the same as z , $\mathbf{n} = [1 \bar{1} 10]$. After the application of the misorientation angles in both crystals, the resulting new unit cell has a modified lattice size to guarantee the periodicity. In this case, the size of the resulting unit cell is $a_x = 4.04 \text{ \AA}$, $a_y = 2.039 \text{ \AA}$ and $a_z = 0.283 \text{ \AA}$. Hence, in the example presented in Figure 5.4 the unit cell is repeated in each direction as indicated by the following three values $N_x = 13$, $N_y = 3$ and $N_z = 29$ for each crystal. More details of the STGB $\Sigma 51\{1 \bar{1} 10\}$ are presented in Figure 5.5. A section is selected from the bicrystal, Figure 5.5(a), where the perfect periodicity in the x and y axes is shown. The final crystalline structure is composed by two layers repeated along the $[1\bar{1}0]$ axis, Figure 5.5(b) and shown in detailed in the Figure 5.5(c) from the standard cubic bcc unit cell of Fe.

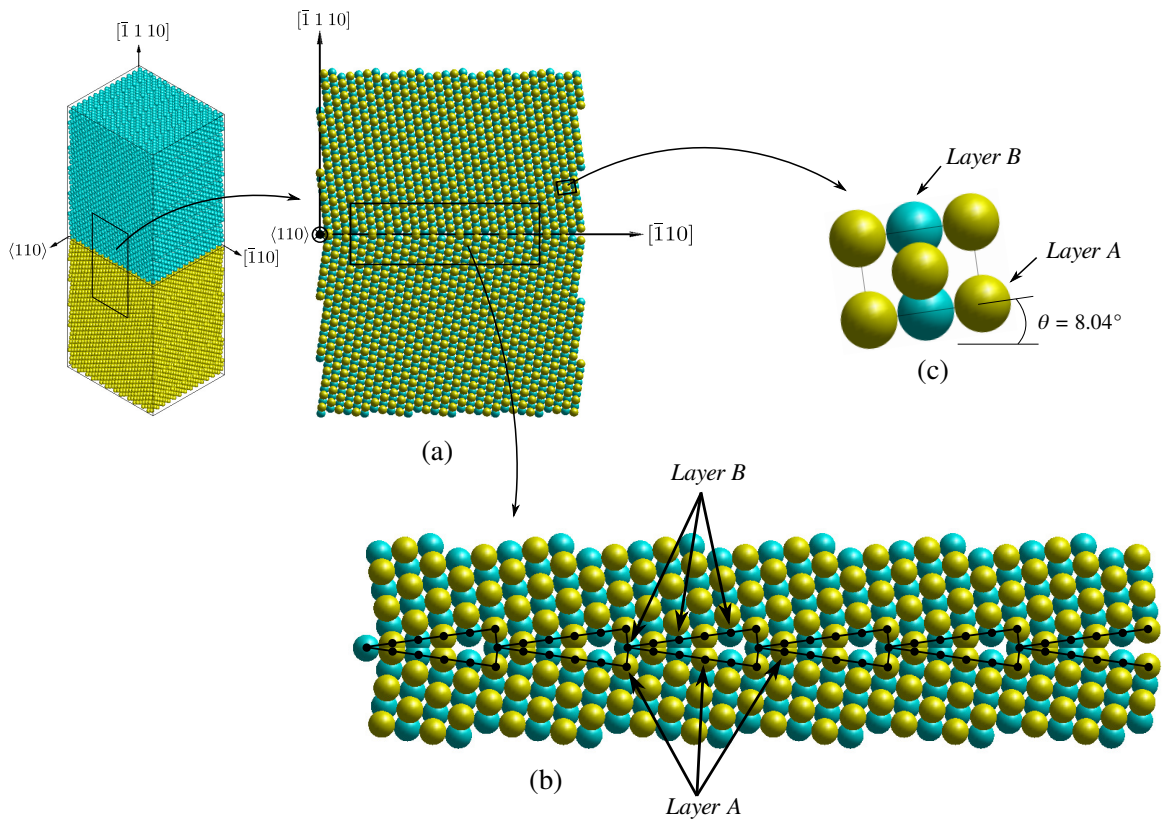


Figure 5.5: Detailed description of the STGB $\Sigma 51\{1 \bar{1} 10\}$ bicrystal.

The computational cell must be large enough to prevent interaction between the parallel boundaries and other finite-size effects (RITTNER AND SEIDMAN, 1996). In this work, the size of the bicrystal with dimensions L_x , L_y and L_z is considered as suggested by (SANGID ET AL., 2010) as $L_x, L_y \geq 5$ nm and $L_z \geq 8$ nm. Owing to the periodicity, the structure is repeated and perfectly matched over the three axes.

In the literature, many studies have been carried out to identify the predominant type of GBs presented in metals and ceramics. It is known that interfaces with high coincident site density or low values of Σ are energetically favorable and frequently found in existing materials, commonly presented in asymmetrical GBs (WOLF, 1991; OGAWA, 2006). Extensive analyses over a large amount of GBs for different materials were presented by Watanabe et al. (1989). They studied the type and frequency of GBs in a rapidly solidified and annealed Fe-6.5 mass%Si alloy, high frequencies of low-angle boundaries and coincident boundaries were observed with $\Sigma 3$, $\Sigma 9$, $\Sigma 11$, $\Sigma 17$ and $\Sigma 19$ in the $\langle 110 \rangle$ rotation axis. Using the same alloy, some additional studies to control the grain

character distribution and its effects on the deformation using directional recrystallization were presented by Zhang et al. (2015). The authors reproduced elongated grain structures, high frequency of both low angle and low Σ values. An analysis in hot-rolled Fe-6.5 mass%Si was carried out by Zhang et al. (2018). They investigated the effects of annealing on GBs texture evolution. Their results were also compatibles with the last two references, the authors obtained a large percentage of $\Sigma 3$, $\Sigma 9$, $\Sigma 13$ and $\Sigma 27$. At 800°C annealing temperature, the mean frequencies of misorientation angles were for 5° and 30°. In case of 650°C annealing temperature, the found higher frequencies were from 0° to 30°. From the conclusions presented by the mentioned works, it is feasible to considerate a large number of STGB, ATGB, STwGB and ATwGB to statistically characterize a representative quantity of interfaces presented in a polycrystalline Fe material, in order to derive an intergranular failure criterion from the atomistic scale to be applied in the mesoscale.

5.2.3 GB Simulations

Molecular dynamic simulations using LAMMPS are carried out to evaluate the GB energy on Fe of a set of STGBs and STwGBs, for a tilt angle varying from 0° to 180° and twist angle varying from 0° to 60°. The GB structures are built with the *GBstudio* using the lattice parameter a and according to the mentioned box size requirements. The STGBs and STwGBs structures are listed in Table C.3.1. As described in the subsection 5.1.3, the EAM (MENDELEV ET AL., 2003) potential is used for Fe. The input file of the potential is available in the *Interatomic Potentials Repository Project*, <https://www.ctcms.nist.gov/potentials/>.

In the minimization of the GB energy, the system is previously annealed to 800 K and then quenched to 10 K (SANGID ET AL., 2010). From an initial temperature T_i and using the time step $dt = 0.001$ ps, the system is stabilized during 1000 time steps at T_i using the *NVE* ensemble. In this model, the pressure remains constant at 0 bar in the whole thermal process. Thus, the annealing and quenching procedures begin: i) the temperature is increased to from T_i to 800 K, ii) the temperature is steady at 800 K, iii) the temperature is reduced to 10 K, iv) the temperature is steady at 10 K. This thermal process is achieved using the *NPT* ensemble. It allows to control the temperature and pressure through the integration over time. The *NPT* is implemented in LAMMPS based on the isothermal-isobaric ensemble presented by Tuckerman et al. (2006). Each process is simulated during 10,000 time steps. At this stage, the structure is ready to be relaxed using the conjugant gradient method. The box is allowed to relax in all directions first, and then only in the normal

direction to the GB in a second minimization to alleviate any GB pressure. The GB energy γ_{GB} is calculated comparing the final energy obtained by the simulation $E_{Bicrystal}$ and the energy of a perfect crystal with the same number of atoms $E_{perfect}$ as follows

$$\gamma_{GB} = \frac{E_{Bicrystal} - E_{perfect}}{2(L_x L_y)}, \quad (5.42)$$

where $A = L_x L_y$ is the GB area, the factor of two, is because the system contains two interfaces owing the periodic boundary conditions in the z -axis. The corresponding energy to a perfect crystal is computed as $E_{perfect} = N E_c$, where E_c is the cohesive energy and N the total number of atoms in the system. The completed algorithm is shown in Figure 5.6.

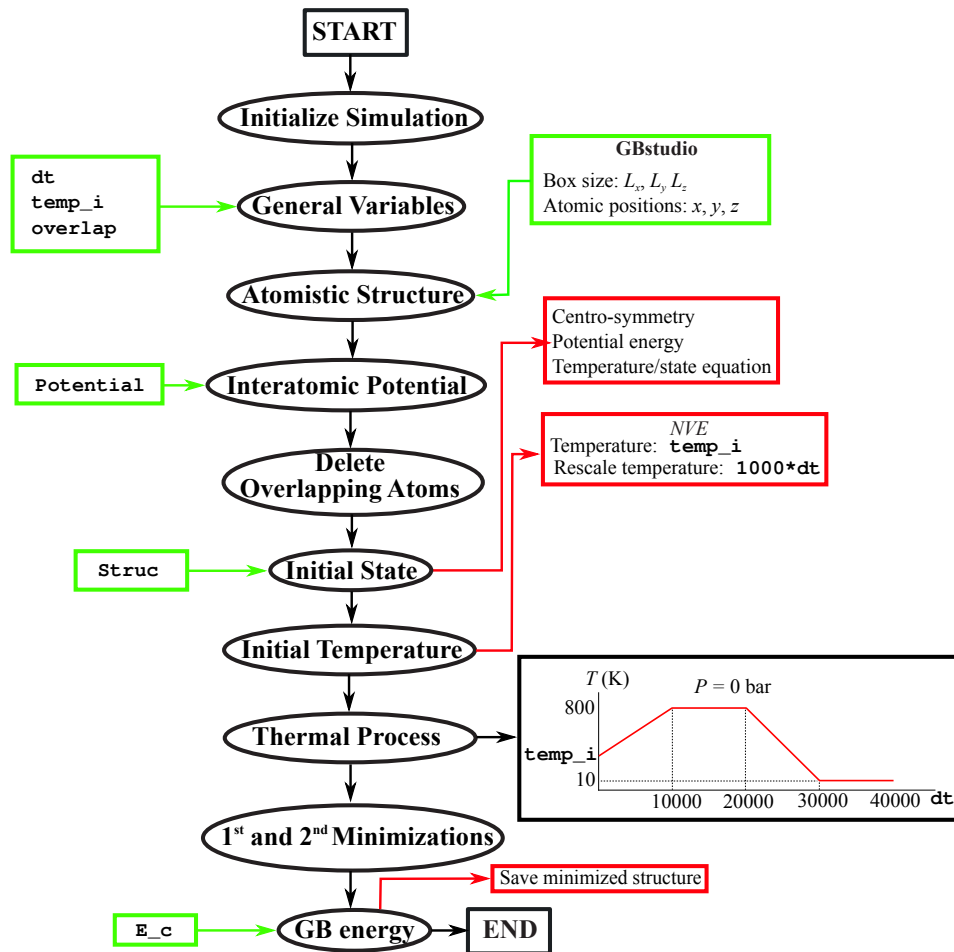


Figure 5.6: Algorithm to evaluate the GB energy using LAMMPS.

This algorithm represents the LAMMPS script implemented in this work, see Appendix C.2. The evaluation of the GB energy is quite similar to the methodology used by (TSCHOPP AND MCDOWELL, 2007A; TSCHOPP AND MCDOWELL, 2007B)³.

In the bicrystal construction, the resulting GB plane is composed by a periodic atomistic arrangement with distinct crystalline orientation compared with the grain interior. This special arrangement in the interface can produce overlap atomic sites, where the distance between atoms is less than the equilibrium lattice parameter a . The overlap effect produces very high values of the potential energy and the interatomic force calculations. Therefore, there are two variables to be fitted, the initial temperature `temp_i` and `overlap`, as shown in the LAMMPS script in the Appendix C.2. By fitting the `overlap` parameter, the atomic sites that cause the superposition effects are deleted. According to the maximum temperature defined in the thermal process and the lattice parameter a , in Table 5.3 the selected intervals to evaluate the GB energy as function of the `temp_i` and `overlap` are presented.

<i>Variable</i>	<i>Interval</i>
<code>temp_i</code> [K]	10 – 650
<code>overlap</code> [Å]	1.5 – 2.70

Table 5.3: Variables to be fitted.

The temperature interval is divided into 10 values and the overlap interval into 8. In total, this results in 80 simulations for each bicrystal listed in Table C.3.1. Hence, it is considered in this work to fit the `temp_i` and `overlap`, only to the first tilt low angle GB $\Sigma 99\{1\bar{1}14\}$ with $\theta = 11.59^\circ$ in the direction $\langle 110 \rangle$ and twist low angle $\Sigma 91\{10\bar{1}\bar{9}\}$ with $\varphi = 10.4^\circ$ in the rotation axis $\langle 111 \rangle$. For the tilt case, the structure has 41184 atoms and in case of twist GB 54208 atoms.

The tilt GB results are presented in Figure 5.7. For a small value of overlap, the GB energy is high in the whole interval of temperatures. Thus, the GB energy is gradually decreasing when the overlap increase, the minimum GB energy is 942.42 mJ/m² at a temperature of 142.92 K and overlap of 2.58 Å.

³https://icme.hpc.msstate.edu/mediawiki/index.php/LAMMPS_Help3

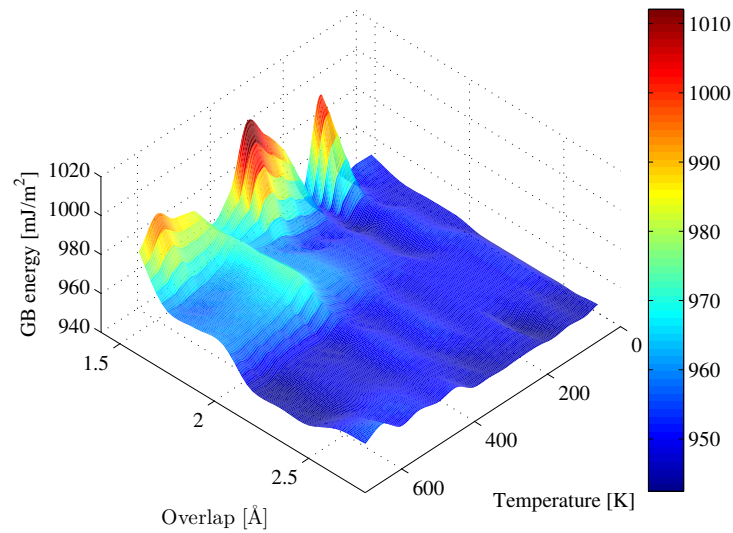


Figure 5.7: GB energy of the tilt $\Sigma 99\{1\bar{1}14\}$ in terms the initial temperature and the overlap parameters.

In case of twist GB, results are presented in Figure 5.8. There is a uniform behavior of high GB energy values for the whole temperature interval with the overlap between 2 \AA and 2.5 \AA . The minimum GB energy is 907.79 mJ/m^2 , at temperature of 526.92 K and 2.01 \AA .

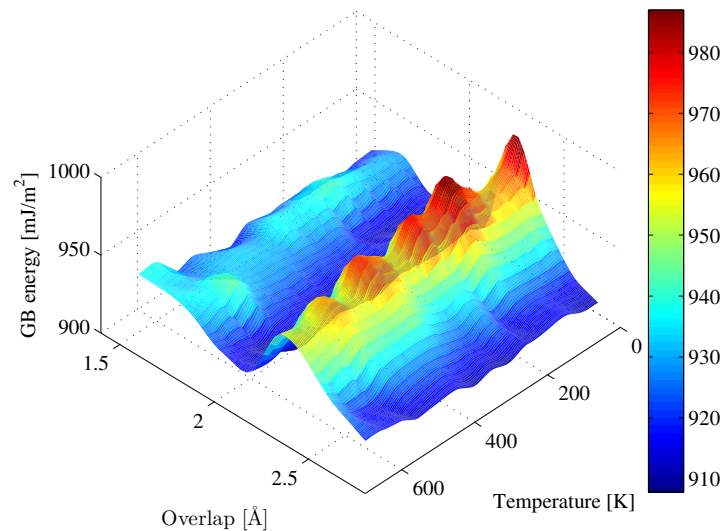


Figure 5.8: GB energy of the twist $\Sigma 91\{10\bar{1}\bar{9}\}$ in terms the initial temperature and the overlap parameters.

Using the fitted values, the GB energy is evaluated for a set of STGBs and STwGBs where the maximum, mean and minimum number of atoms are presented in Table 5.4.

	<i>Tilt</i>	<i>Twist</i>
<i>Max</i>	61,776	74,256
<i>Mean</i>	43,537	50,055
<i>Min</i>	27,872	31,824

Table 5.4: Number of atoms used to model the STGBs and STwGBs, from the structures presented in Table C.3.1.

The GB energy given in terms of the tilt angle θ is shown in Figure 5.9, these results are compared to the values presented by Tschopp et al. (2012) using the same EAM potential. Results shown to be close to the reference values, especially for misorientation angles greater than 60° . Furthermore, two deep values are identified for $\Sigma 3(1\bar{1}2)$ and $\Sigma 11(3\bar{3}2)$. Additionally, it can be observed the strongly variation of the GB energy depending on the misorientation angle.

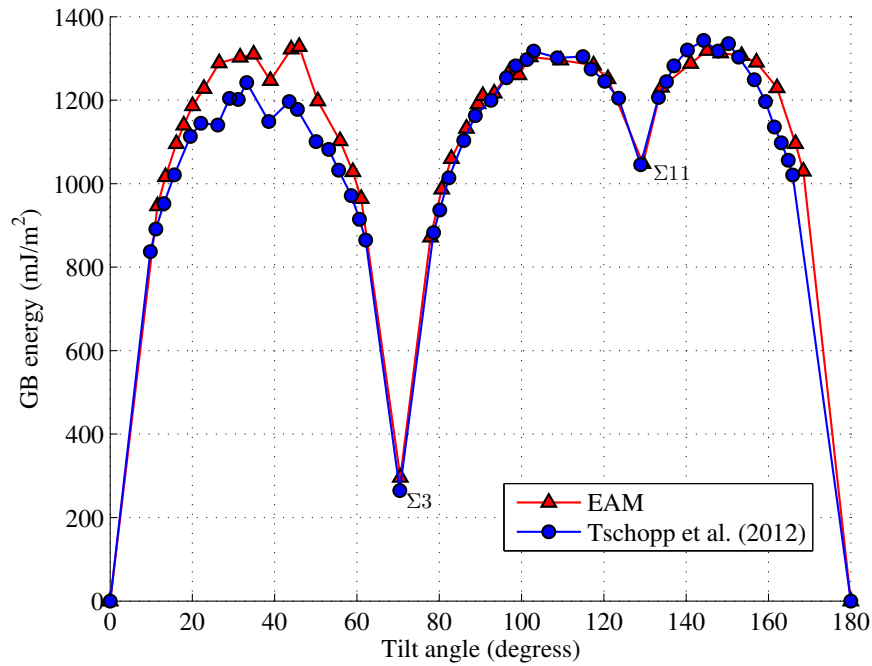


Figure 5.9: GB energy of STGBs $\langle 110 \rangle$ in terms of the tilt angle θ .

Results for the twist case are shown in Figure 5.9. Comparisons are carried out with the values given by Wolf (1991) and Runnels et al. (2016). They used different approaches for the analysis, Wolf (1991) used an iterative minimization algorithm at zero temperature with a Johnson-type pair potential. Runnels et al. (2016) proposed a relaxation method using the EAM and Lennard-Jones potentials.

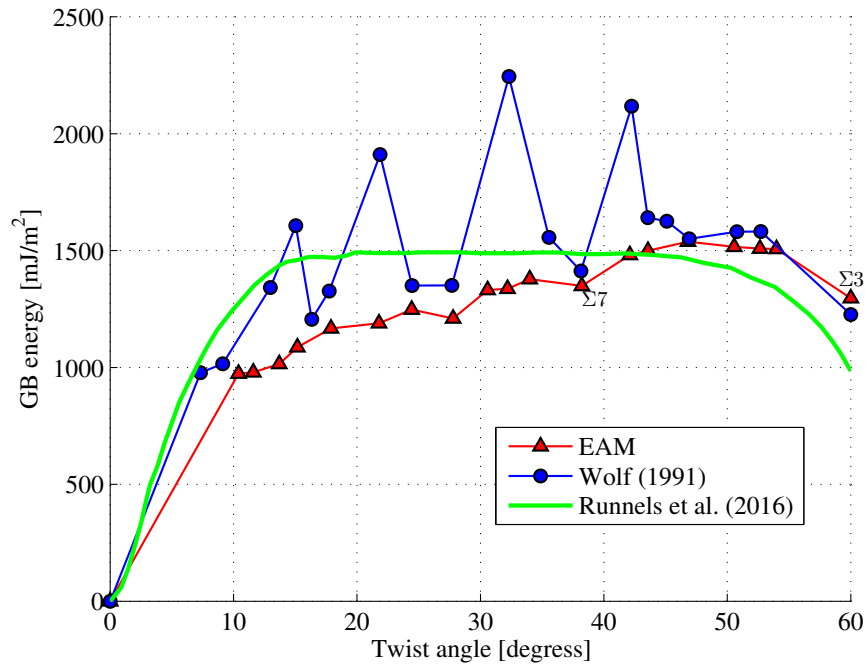


Figure 5.10: GB energy of STwGBs $\langle 111 \rangle$ in terms of the twist angle φ .

A steadier behavior of the GB energy was obtained compared to the two references in Figure 5.10. In this case, there are not deep characteristic values, that mean the STwGB structures contain large defects from the perfect crystal. Even for low values of the reciprocal density $\Sigma 3$ and $\Sigma 7$, the CSL fails from its basic definition. The GB energies evaluated from the STwGBs result in higher values compared with the evaluated from the STGBs. Otherwise, the values of the misorientation angle of the STwGB show to be more regular than the GB energy for STGB.

The computational simulations were carried using the *Kahuna cluster* with a group of 192 threads. In total 223 simulations were performed to obtain results from Figures 5.7 to 5.10.

6 Multiscale model

This chapter presents the multiscale approach between the meso- and atomistic scales. After the GB energy evaluation, the MD algorithms to obtain the stress-strain constitutive tensile and shear relationships are shown. The multiscale bridging is carried out applying the asymptotic scaling analysis to calculate the critical energy densities. The failure condition is analyzed using the generalized energy failure criterion, considering the variation of the lattice structure in each GB. Finally, under dynamic boundary conditions, intergranular failure paths propagate through the polycrystalline structure are exposed.

6.1 Critical energy densities

Molecular dynamic simulations using LAMMPS are carried out to evaluate the tensile and shear failure of the minimized Fe GB structures. The important fact in these simulations is to capture the variation of the critical tensile E_{nc} and shear E_{sc} energy densities depending on the GB orientations. This atomistic model offers a more realistic behavior of the failure process at the interfaces, taking into account the brittle and ductile levels of each GB. For this purpose, a set of 101 STGB, ATGB, STwGB and ATwGB is generated varying the reciprocal of the density coincident-sites from $\Sigma 3$ to $\Sigma 81$, see Appendix C.4. The bicrystal contains an initial central crack to get a more brittle failure and also to reduce the plastic deformation regime. The dimensional specifications are shown in Figure 6.1, this configuration is similar to the model used by Dingreville et al. (2017) and in references (YAMAKOV ET AL., 2008; BARROWS ET AL., 2016).

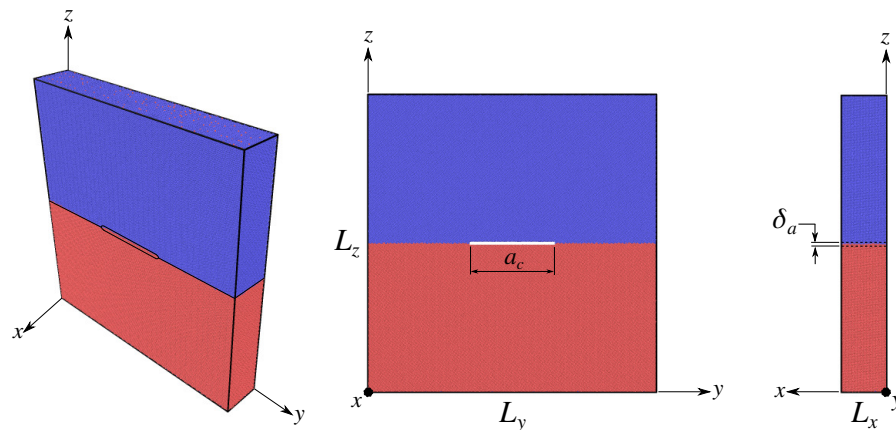


Figure 6.1: Nanoscale specimen for failure simulations.

where a_c is defined as $0.3L_y$ and δ_a is equal to $3a$, being a the lattice parameter. This is to avoid the interaction between atoms in the crack surfaces during the energy minimization process. Furthermore, $L_x/L_y < 1$ being L_x large enough to avoid an interference on the free surface effect produced by the periodic boundary conditions between the walls at $x = 0$ and $x = L_x$. In Table 6.1, the statistical information of the number of atoms, dimensional details and the GB energies of the nanoscale specimens are presented.

	<i>Atoms</i>	L_x	L_y	L_z	γ_{GB}
<i>Max</i>	2,754,000	74.18	755.09	758.44	3,288.40
<i>Mean</i>	623,367	25.42	541.62	541.43	1,478.62
<i>Min</i>	199,680	10.68	346.91	377.67	781.96

Table 6.1: Details of the nanoscale specimens, GB energy expressed in [mJ/m²] and length values in [Å].

It can be observed in Table 6.1 that there is a huge variation in the specimen size from 199680 to 2,754,000 atoms. This is due to the minimum size of a unit GB cell defined by the *GBstudio* package, that guarantees the perfect periodicity in the x , y and z axes. In addition, the GB energy γ_{GB} gives an idea of the defect fluctuation caused by the misorientation. The transition lattice structure produced in the GBs, makes it necessary to contemplate the shear analysis in both x and y axes and also in the positive and negative directions. Then, in total, five simulations are developed for each bicrystal, one for tensile and four for shear loads. In case of shear in the x -direction, the initial crack is fitted on the x -axis and $L_x/L_y > 1$. Dynamic boundary conditions are applied through a deformation rate $\dot{\epsilon}$ applying the following definitions:

	$z = 0$	$z = L_z$
<i>Tensile</i> (n)	$\dot{\epsilon}_{zz}$	$-\dot{\epsilon}_{zz}$
<i>Shear</i> (xz^\pm)	$\pm\dot{\epsilon}_{xz}$	$\mp\dot{\epsilon}_{xz}$
<i>Shear</i> (yz^\pm)	$\pm\dot{\epsilon}_{yz}$	$\mp\dot{\epsilon}_{xz}$

Table 6.2: Dynamic boundary conditions for tensile and shear tests.

A high deformation rate is applied to the GB after the energy minimization process, where the structure is stored at a temperature of 10K. First, the initial variables are defined, where the time

step dt is 0.001ps, the temperature $temp$ is 296K and the deformation rate $erate$ is equal to 0.001 and 0.01 for tensile and shear analyses, respectively. The $erate$ values mean that $\dot{\epsilon}_{zz} = 10^9/s$ and $\dot{\epsilon}_i = 10^{10}/s$, $i = yz, yz$ are used in these simulations according to Table 6.2. Then, the minimized GB structure is read from a database. Before the application of the deformation rate, the temperature is increased from 10 K to 296 K allowing the box to contract or expand in all directions during 10,000 time steps. This process is achieved applying a Langevin thermostat (SCHNEIDER AND STOLL, 1978) and the canonical isenthalpic–isobaric (*NPH*) ensemble (PARRINELLO AND RAHMAN, 1981; MARTYNA ET AL., 1994; SHINODA ET AL., 2004)⁴. This initial part of the algorithm is common for both tensile and shear loads as illustrated by the flowchart shown in Figure 6.2.

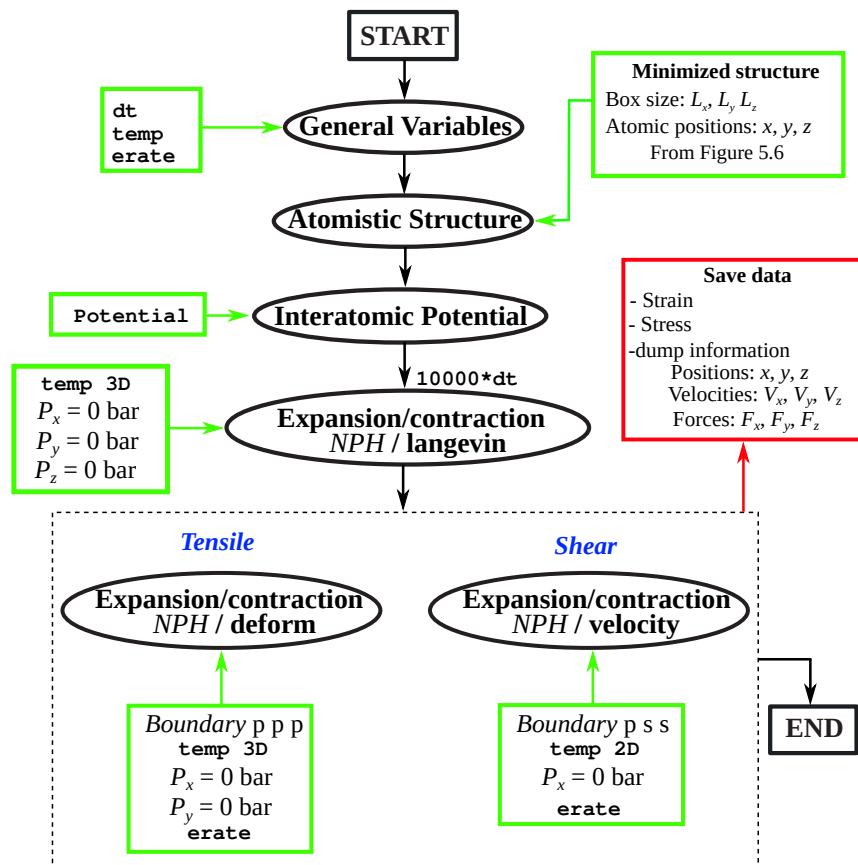


Figure 6.2: Algorithms for tensile and shear LAMMPS scripts.

In order to impose the tensile load, the z expansion is applied on the box using the *fix deform* command⁵. Moreover, while the x and y contraction effects result by *NPH* ensemble, using the pe-

⁴http://lammps.sandia.gov/doc/fix_nh.html

⁵http://lammps.sandia.gov/doc/fix_deform.html

riodic boundary conditions in the three axes. In case of shear deformation, e.g. (yz^\pm), the boundary conditions must be changed on the y and z axes to non-periodic conditions, the x keeps periodic. The deformation is imposed using the *velocity* command⁶. Notice that, this process is developed at a constant temperature of 296 K, and it is calculated using the total kinetic energy of the group of atoms. Hence, the temperature must be computed partially after excluding y -component⁷. These procedures are depicted inside the dashed region in Figure 6.2 and the detailed LAMMPS scripts are presented separately in Appendix C.5.

Results of these MD models are shown in Figure 6.3, for five GB structures under tensile (n) and shear (yz^+) loading cases. Initially, the variation in the constitutive behavior and mechanical properties such as the yield and ultimate strength of these GBs can be appreciated, expressed by the Virial stress definition of the macrostate and the applied strain rate.

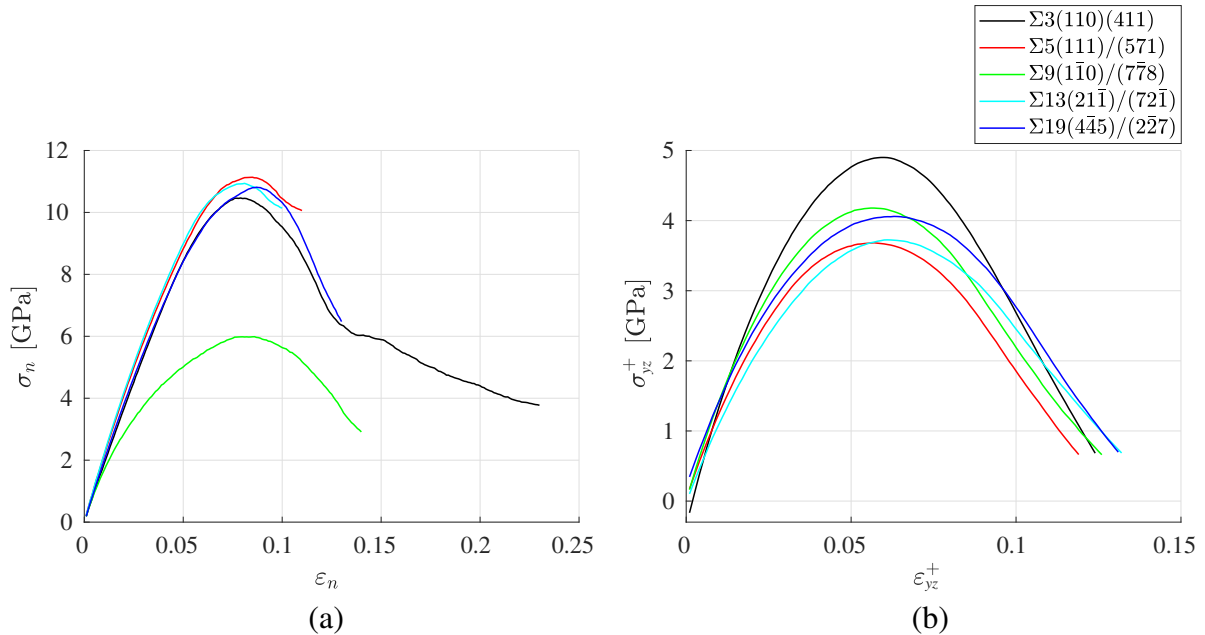


Figure 6.3: Stress-strain constitutive behavior for different GB structures: (a) tensile and (b) shear.

In Table 6.3, numerical values of the maximum stress and GB energy γ_{GB} for each GB are given for both cases presented in Figure 6.3. In the structures $\Sigma 5$, $\Sigma 9$, $\Sigma 13$ and $\Sigma 19$ ductile failure is predominant under shear load. The opposite situation appears for $\Sigma 3$, where a high deformation level is required to fail under tensile load. Hence, from the energy point of view, some conclusions

⁶<https://lammps.sandia.gov/doc/velocity.html>

⁷https://lammps.sandia.gov/doc/compute_temp_partial.html

could be defined. According to the CSL model, the $\Sigma 3(110)/(411)$ structure is closest to a perfect GB, owing to the high number of coincident sites that means its energy is at the lowest value as $1,160.90 \text{ mJ/m}^2$. This concept can fail sometimes, due to the geometrical character of the CSL model. An explanation can be made analyzing the tilt angle θ , e.g. between the $\Sigma 3\{1\bar{1}2\}$ and $\Sigma 3\{111\}$ structures, in which the tilt angles are 70.52° and 109.5° respectively. Despite these structures having the same number of coincident sites $\Sigma 3$, the $\Sigma 3\{111\}$ GB has more defects with respect to the perfect structure. Moreover, the $\Sigma 3\{1\bar{1}2\}$ represents a low energy value according to the behavior presented in Figure 5.9.

<i>GB structure</i>	σ_n^{max}	σ_{yz}^{+max}	γ_{GB}
$\Sigma 3(110)/(411)$	10.46	4.90	1,160.90
$\Sigma 5(111)/(571)$	11.13	3.68	1,377.61
$\Sigma 9(1\bar{1}0)/(7\bar{7}8)$	5.98	4.17	3,163.04
$\Sigma 13(21\bar{1})/(72\bar{1})$	10.93	3.72	1,267.35
$\Sigma 19(4\bar{4}5)/(2\bar{2}7)$	10.81	4.05	1,381.11

Table 6.3: Critical stress values expressed in [GPa] and GB energy in [mJ/m^2].

Considering the last definitions, it is worth noting that the $\Sigma 9(1\bar{1}0)/(7\bar{7}8)$ structure has the highest GB energy of $3,163.04 \text{ mJ/m}^2$. This fact reflects more sensibility to fail specially under tensile load. Results also show the difference on the stress level between the models as expected. The nucleation of defects such as dislocations caused by the shear load might cause the slip failure mechanisms to be more susceptible to fail. A complete analysis of the relationship between tensile and shear modes in grain boundaries was presented by Paliwal and Cherkaoui (2013). They found the a drastic increment on the maximum shear stress caused by the application of boundary conditions defined by $0^\circ < \theta < 85^\circ$ being $\theta = \arctan(\dot{\epsilon}_{zz}/\dot{\epsilon}_{yz})$, contrary to the tensile stress that presents a slower variation in its magnitude.

Failure instants are presented in Figure 6.4, for tensile from 50 ps to 90 ps and in Figure 6.5 for shear from 50 ps to 110 ps, on the $\Sigma 37(2\bar{2}\bar{1})/(2\bar{2}1)$ structure with 1417248 atoms. In these figures, the blue color represents the bcc structures and the red color, the transition lattices in the interface structures. In the left figures, the 3D model is depicted. The central and right figures show in detail the separation process.

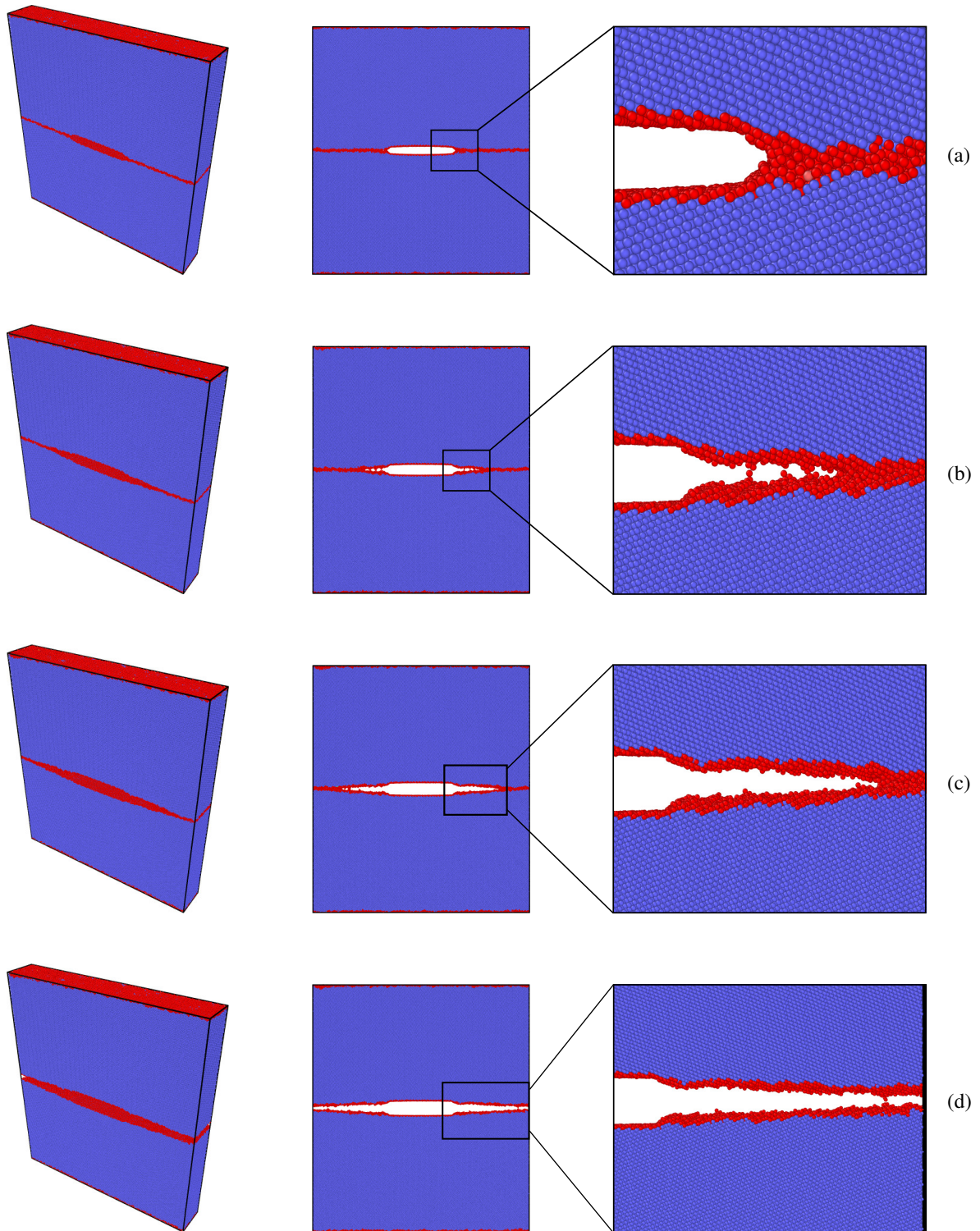


Figure 6.4: Tensile failure of $\Sigma 37(2\bar{2}\bar{1})/(2\bar{2}1)$ structure: (a) $t = 50$ ps, $\sigma_n = 9.28$ GPa, $\varepsilon_n = 5\%$; (b) $t = 70$ ps, $\sigma_n = 10.26$ GPa, $\varepsilon_n = 7\%$; (c) $t = 80$ ps, $\sigma_n = 10.16$ GPa, $\varepsilon_n = 8\%$; (d) $t = 90$ ps, $\sigma_n = 9.39$ GPa, $\varepsilon_n = 9\%$.

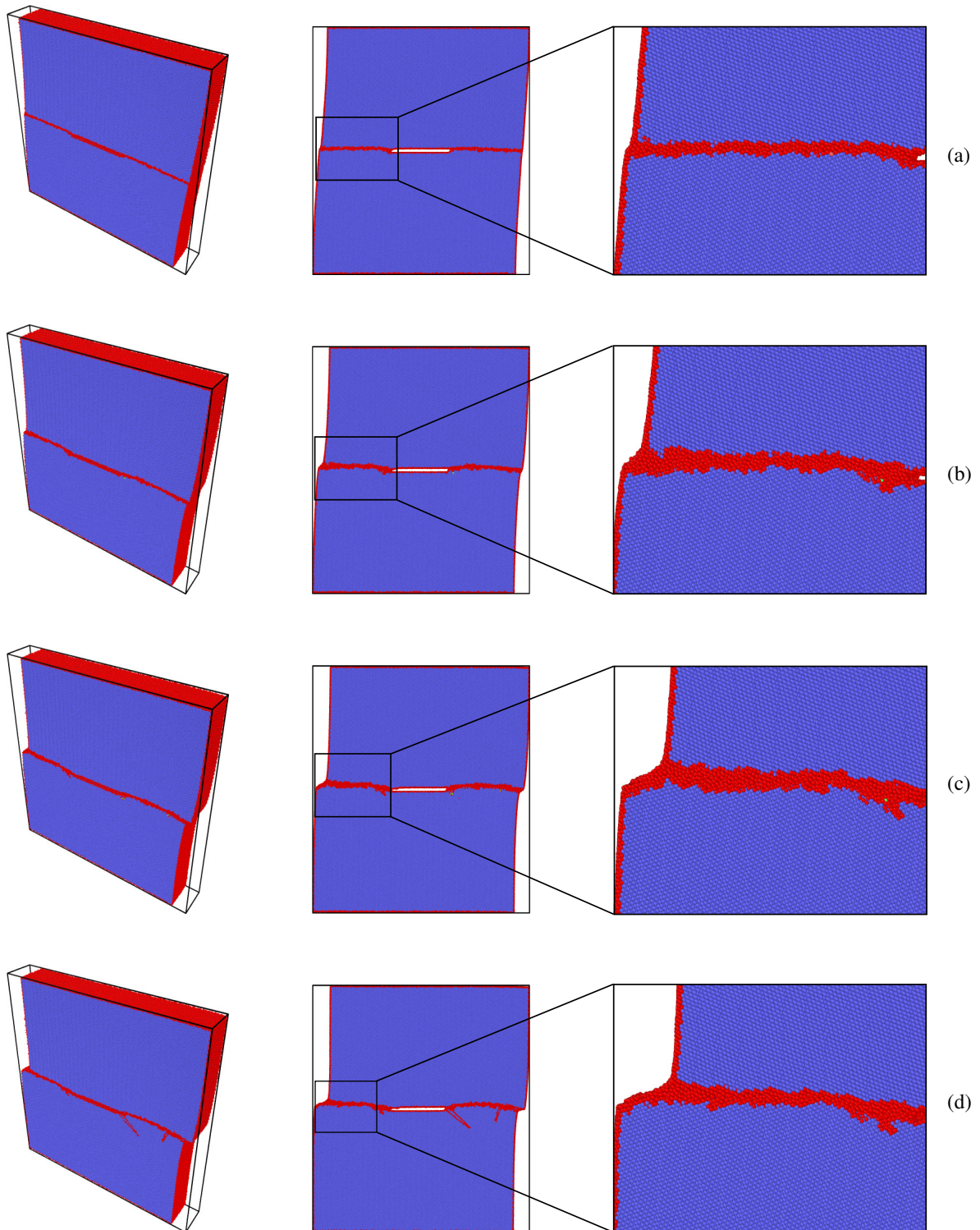


Figure 6.5: Shear failure of $\Sigma 37(2\bar{2}\bar{1})/(2\bar{2}1)$ structure: (a) $t = 50$ ps, $\sigma_{yz}^+ = 3.38$ GPa, $\varepsilon_{yz}^+ = 5\%$; (b) $t = 70$ ps, $\sigma_{yz}^+ = 2.61$ GPa, $\varepsilon_{yz}^+ = 7\%$; (c) $t = 80$ ps, $\sigma_{yz}^+ = 1.31$ GPa, $\varepsilon_{yz}^+ = 9\%$; (d) $t = 110$ ps, $\sigma_{yz}^+ = 0.45$ GPa, $\varepsilon_{yz}^+ = 11\%$.

These results show failure under different modes. Owing to the inclusion of the initial crack, it can be inferred that the separation of the effective GB area is easy to be captured. As mentioned, the trend for both models is to fail on the interface GB plane, with the shear stress being approximately 30% of the tensile stress.

The computational simulations were also carried out using the *Kahuna cluster* with a group of 192 threads. In total 707 simulations were performed.

6.1.1 Asymptotic scaling

The material behavior presents an increment in its mechanical properties when the scale length tends to be small, and also in case of imposition of high deformation rate. This effect can be observed in results shown in Figure 6.3, where the level of the yield strength reaches up to 11 GPa approximately in the nanoscale under tensile strain. It is evidently much higher than the well-known strength values in microscopic scales of MPa order. Hence, the scaling effects represent a challenge in the multiscale modeling where several approximations have been developed to attempt the scaling of mechanical properties such as yield and rupture limits. Some numerical models were treated before and can be found in the literature such as (CHEN ET AL., 2005; GUO ET AL., 2007; CHEN ET AL., 2007). In these investigations, several efforts were presented, in order to find functions to represent the scaling change in terms of size and deformation rate for pure metals like copper. More related to the work presented here, Hammami and Kulkarni (2017) showed the rate dependence of grain boundary sliding via atomistic simulations.

Due to the number of GBs regarded in this approach, and the range of atoms used in their construction, Table 6.1, it would take a large processing time for simulating both the length and rate dependencies. Hence, as a first approximation, it is proposed to adopt the asymptotic scaling analysis presented by Chen et al. (2007) applied for different size length of geometrically similar structures. They proposed a simple formulation that could represent the size effect on the strength, based on the asymptotic relationship between the nominal strength and sizes widely exposed before in (BAZANT, 2002). Then, Equation (6.1) is applied to scale the yield strength between the nominal parameters, σ_{na} and σ_m , that correspond to the yield stress in the nano and micro scales respectively:

$$\left\{ \begin{array}{ll} \sigma_o = \sigma_{na} & D \leq D_{na} \\ \log \sigma_o = \log \sigma_m + (\log \sigma_{na} - \log \sigma_m) \cdot \\ \left[1 - \sin \left(\frac{\pi}{2} \frac{\log D - \log D_{na}}{\log D_m - \log D_{na}} \right) \right] & D_{na} < D < D_m \\ \sigma_o = \sigma_m & D_m \leq D \end{array} \right. , \quad (6.1)$$

where σ_o and D are the nominal strength and size to be found respectively. In this work, the D_{na} term is considered as the nanoscale size, in which any smaller size $D \leq D_{na}$ produces a constant strength $\sigma_o = \sigma_{na}$. The opposite effect is considered if $D_m \leq D$ being D_m the microscale size limit. Some assumptions have been taken owing to the lack of experimental data from these scales. As indicated by Bazant (1993), the characteristic dimension D_{na} can be chosen arbitrarily. Hence, if the characteristic size of each GB is defined by the average of the GB plane, the D_{na} term can be evaluated by the average dimension over all 101 GBs planes as follows

$$D_{na} = \frac{1}{N_{GB}} \sum_{k=1}^N \frac{L_x^{na,k} + L_y^{na,k}}{2}, \quad \left\{ \begin{array}{ll} L_x^{na} = L_x & \rightarrow \text{shear } (xz^\pm) \text{ mode} \\ L_y^{na} = L_y & \rightarrow \text{shear } (yz^\pm) \text{ mode} \end{array} \right. . \quad (6.2)$$

where N_{GB} is the number of GBs. As mentioned before, there are two defined specimens according to the xz^\pm or yz^\pm shear tests, in which $L_x/L_y < 1$ and $L_x/L_y > 1$ are satisfied, respectively. Note in Equation (6.2) that D_{na} takes into account the main lengths used in the shear failure. The σ_{na} limit remains constant if $D \leq D_{na}$, according to this hypothesis, it is possible to evaluate σ_{na} as the average of the maximum stress over all GBs, depending on the failure test. In conclusion, the nanoscale limits (D_{na}, σ_{na}) reflect an approximation of an average material that can represent the assembly of all nanoscale GBs.

For the definition of the macroscopic limits (D_m, σ_m), the stress value is taken from the investigation presented by Sakui and Sakai (1972). The authors studied the effect of strain rate, temperature and grain size on the lower yield stress and flow stress of polycrystalline pure iron. Then, for a $10.3 \mu\text{m}$ grain size at 290 K under 10^0 of deformation rate, they found a lower yield stress of 490MPa. Due to the size length not being reported by the authors, in accordance with the grain size, the macroscopic length limit is assumed as $100 \mu\text{m}$. Ideally, with this value, the microscopic polycrystalline structure will contain about 1,000 grains, that is enough to guarantee the convergence for elastic and mechanical properties.

Now, the asymptotic limits were defined, the scaling procedure can be applied on the maximum stress over all previous results of nanoscale failure. Using as a desired transitional scale size D equal to $1 \mu\text{m}$, this value corresponds to the average length of all boundary elements used in the discretization of the polycrystal aggregate, Figure 2.2. In summary, the required scaling values for the tensile test are shown in Table 6.4:

D_{na}	σ_{na}	$\parallel D \parallel$	D_{m}	σ_{m}
0.0529	10.90	1	100	0.490

Table 6.4: Limit scaling values for tensile test, length expressed in $[\mu\text{m}]$ and stress in $[\text{GPa}]$.

Thus, the complete set of tensile critical energy density E_{nc} is presented in Figure 6.6. These values are obtained from the area under the scaled curve of the stress-strain constitutive relationship.

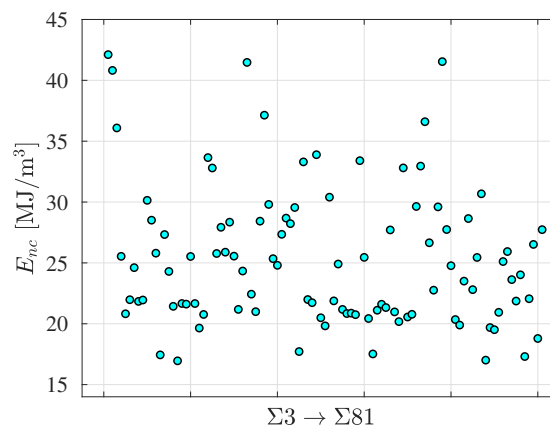


Figure 6.6: Critical tensile E_{nc} energy density depending on the GB structure.

The maximum critical tensile energy density is $42.11 \text{ MJ}/\text{m}^3$ and the minimum is $16 \text{ MJ}/\text{m}^3$. From Figure 6.6 it is observed that E_{nc} lies between these two limits, presenting a scattered behavior. For the shear cases, the only difference is the microscopic stress limit. Defining the shear stress limit at nanoscale (σ_{na_s}), being the average over all the maximum shear stress found in the 101 GBs, and the ratio $\eta = \sigma_{\text{na}_s}/\sigma_{\text{na}}$ expressed by

$$\eta = \frac{\sigma_{na_s}}{\sigma_{na}}, \quad \sigma_{na_s} \begin{cases} \frac{1}{N_{GB}} \sum_{k=1}^N \sigma_{xz}^{+max,k}, & \frac{1}{N_{GB}} \sum_{k=1}^N \sigma_{xz}^{-max,k} \\ \frac{1}{N_{GB}} \sum_{k=1}^N \sigma_{yz}^{+max,k}, & \frac{1}{N_{GB}} \sum_{k=1}^N \sigma_{yz}^{-max,k} \end{cases} \quad (6.3)$$

The shear component of the nano and micro scales are σ_{na_s} and σ_{m_s} , respectively. Assuming that the ratio η keeps constant through the scaling, $\sigma_{m_s} = \eta\sigma_m$, where σ_{na_s} is known from the MD model. In Table 6.5, the average values used to scale the data from the shear tests are presented, resulting very similar in the four cases:

	D_{na}	σ_{na_s}	D	D_m	σ_{m_s}	η
$(xz)^+$	0.0529	3.61	1	100	0.162	0.331
$(xz)^-$	0.0529	3.58	1	100	0.161	0.329
$(yz)^+$	0.0529	3.60	1	100	0.162	0.330
$(yz)^-$	0.0529	3.60	1	100	0.161	0.330

Table 6.5: Limit scaling values for shear tests, length expressed in [μm] and stress in [GPa].

After the scaling process, results of the shear loading cases are shown in Figures 6.7 and 6.8. The scattered trend of the energy values caused by the variation of the crystalline orientations of the GBs from $\Sigma 3$ to $\Sigma 81$ can be appreciated.

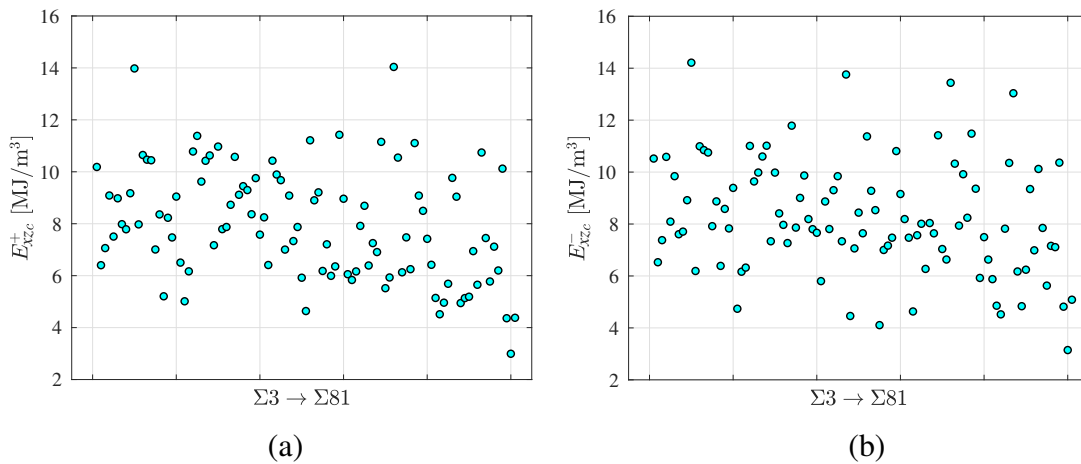


Figure 6.7: Critical shear energy densities: (a) $E_{xz_c}^+$ and (b) $E_{xz_c}^-$, both depending on the GB structure.

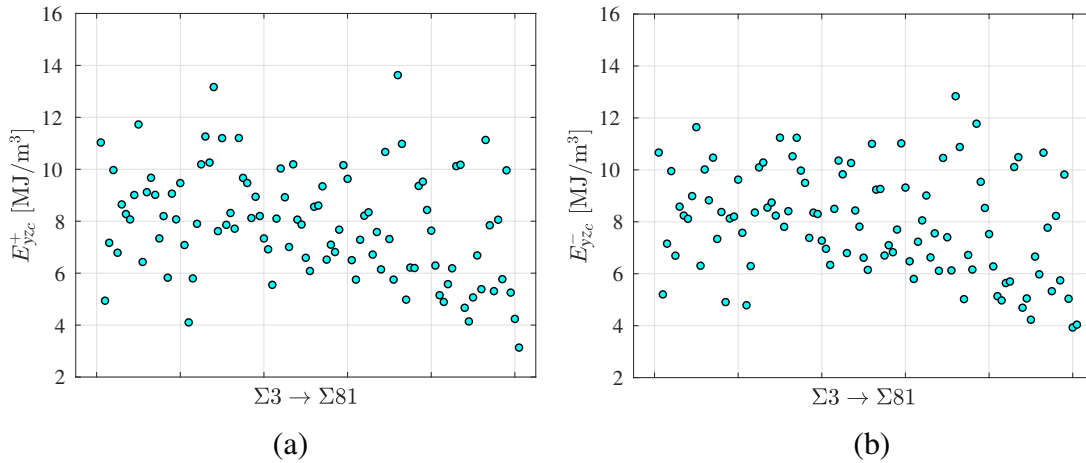


Figure 6.8: Critical shear energy densities: (a) E_{yzc}^+ and (b) E_{yzc}^- , both depending on the GB structure.

Some differences between the specific shear modes in both positive and negative direction of the application load. The maximum shear critical energy found was $E_{yzc}^- = 14.21 \text{ MJ/m}^3$ and the minimum limit is $E_{xzc}^+ = 2.99 \text{ MJ/m}^3$. Comparing these energies to the tensile critical energy, an important fact is captured from these results. The defects caused by the transitional lattice in the interfaces reflects a preference to fail under the slip condition in the GB plane.

6.2 Intergranular failure

The previous atomistic analyses provide a relevant concept of how the lattice structure can influence the local and overall failure behavior from an energy point of view. Now, the generalized energy failure criterion is established using the obtained energy densities. Next, the failure criterion is incorporated on the mesoscale model, showing the additional implementation included in the BEM formulation. Finally, the sudden crack propagation in the polycrystal aggregate is shown, caused by the application of a high-rate ramp load.

6.2.1 Generalized energy failure criterion

The nanoscopic model revealed how the role of the GBs is important for the failure phenomenon, that can affect the overall behavior of the microscopic structure. This aspect is relevant for the intergranular modeling, in which several methods can be used to predict failure in different modes. In this first multiscale approach between BEM and MD, the generalized energy failure criterion recently found by Qu et al. (2016) is adapted to a three-dimensional analysis. This criterion is based on the critical energy densities for tensile and shear modes. The critical energy densities act as threshold properties for each specific GB. This criterion becomes a simple way to evaluate damage at interfaces, if the critical energies are previously known from experiments or numerical simulations. As mentioned, the MD modeling used in this work offers a great advantage in the evaluation of all these threshold material properties, including some additional physics aspects.

Based on the classical Rankine criterion, the cleavage failure requires energy to break the atomic bonds forming new crack surfaces and ideally corresponds to the elasticity limit state or the well-defined brittle failure. Otherwise, in the Tresca criterion, shear deformation also needs energy to activate the plastic regime leading to a ductile failure. Therefore, both Rankine and Tresca criteria might be essentially energy criteria. Hence a simple failure criterion, as shown in Equation (6.4), were proposed and validated by Qu et al. (2016) in order to predict failure considering the shear and cleavage mechanisms.

$$\frac{E_s}{E_{sc}} + \frac{E_n}{E_{nc}} = 1 \quad . \quad (6.4)$$

In Equation (6.4), E_{sc} and E_{nc} represent the previously defined critical energy densities for tensile and shear conditions. In Equation (6.4), it is concluded that the failure process takes into account both modes on the most critical crystalline plane, that in this case correspond to the GB plane. It can be observed in Figure 6.4 that the failure processes are not perfectly linear. Owing to the presence of the central crack, while the loading is imposed the material strength is progressively reduced, this is quantified by the dissipative energy density (E^d) (LI, 2001). Furthermore, for some of the GBs used in this work, plastic regime can appear during the process, being necessary to evaluate the plastic energy density (E^p). Additionally, the quasi-linear behavior from 0 GPa to the σ^{max} corresponds to the elastic energy density (E^e). Considering all these regimes, each energy

density can be represented by

$$E = E^e + E^p + E^d = \int_0^{\varepsilon_{ij}^f} \sigma_{ij} d\varepsilon_{ij} \quad . \quad (6.5)$$

where ε_{ij}^f is the strain field at the instant failure occurs. Hence, the energy densities presented in Figures 6.6, 6.7, and 6.8 contain the elastic, plastic and dissipative regimes in different proportions according to the GB structure. Applying Equation (6.4) for each shear case, the following four failure criteria, Figures 6.9 and 6.10, can be graphically represented.

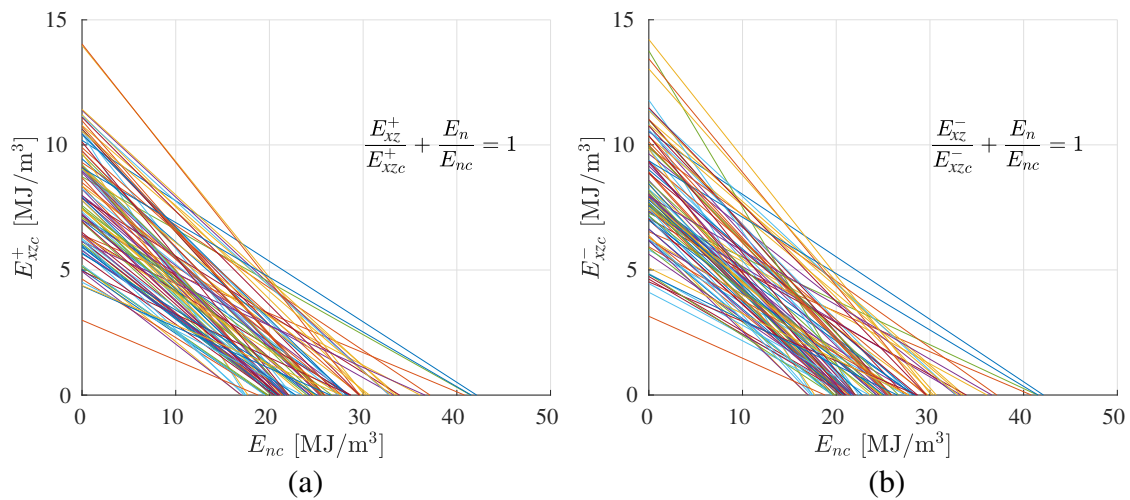


Figure 6.9: Energy failure diagram: (a) *tensile-shear* (xz^+) and (b) *tensile-shear* (xz^-) .

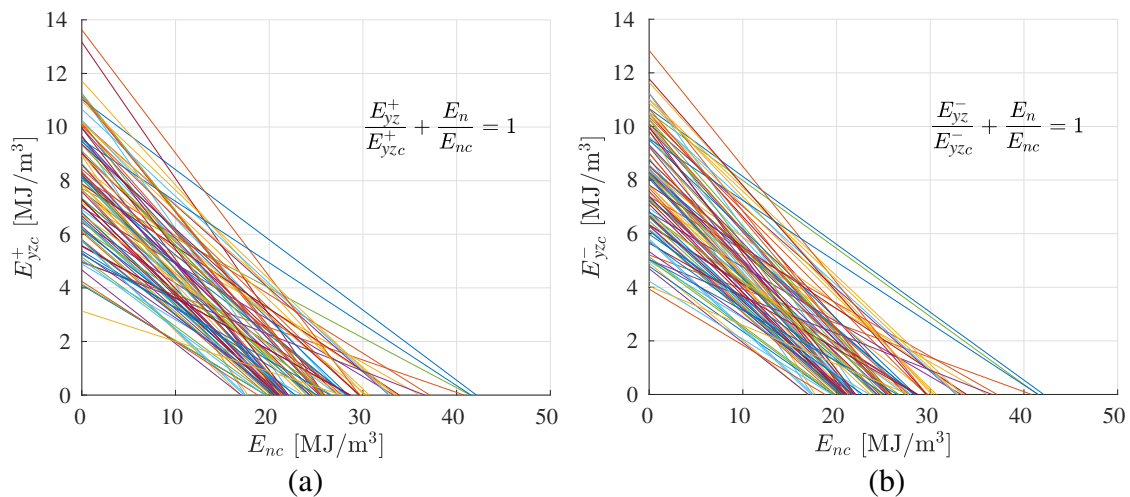


Figure 6.10: Energy failure diagram: (a) *tensile-shear* (yz^+) and (b) *tensile-shear* (yz^-) .

Below each failure line in the energy diagrams the Fe should always be safe. Notice that, some differences can be perceived between the failure lines of the xz or yz cases. Qu et al. (2016) suggest the definition of the ratio $\varphi = E_{sc}/E_{nc}$ as a parameter that determines the inherent failure mechanism of a material. If $\varphi > 1$, failure is mainly governed by cleavage, indicating that the material is more brittle than the contrary case $\varphi < 1$, in which the shear failure is predominant and more deformation must be applied to reach the failure condition. The φ limits obtained in this model are presented in the following table:

<i>Case</i>	φ_{Max}	φ_{Mean}	φ_{Min}
(xz^+)	0.600	0.320	0.156
(xz^-)	0.625	0.334	0.157
(yz^+)	0.554	0.319	0.113
(yz^-)	0.554	0.321	0.127

Table 6.6: Limits of φ ratio.

According to the previous results, the failure of Fe is dominated by shear condition. This agrees with some reference values shown in (QU ET AL., 2016), comparing the ratio φ , e.g. for carbon steel (0.55 wt% C) it varies from 0.18 to 0.61. This criterion shows to be useful to predict failure considering both basic mechanisms. It is worth noting that, for GB structures, it is not necessary to find the most critical crystalline plane, since it is implicitly the same GB plane. Furthermore, a detailed extension was considered here to include the two shear directions in a 3D analysis.

6.2.2 Mesoscale failure

The final stage of the proposed BEM-MD multiscale approach is illustrated to predict the intergranular failure of polycrystalline Fe at the mesoscale. The damage level is assessed in the interfaces of the polycrystal aggregate by the implementation of the energy failure diagrams at every time and load steps. As mentioned before, this is a continuum model with stochastic crystalline orientations and grain shapes. Hence, infinite possibilities of transition lattice structures can appear in the grain boundaries. For this reason, it is a difficult task to identify the exact tilt, twist or mixed type of misorientation. Then, if a very large sample of atomic GB structures is considered, a more significant failure interval can be obtained, which could be statistically applied along the structure.

Reminding the elastic constants of polycrystalline Fe, $C_{11} = 230$ GPa, $C_{12} = 135$ GPa and $C_{44} = 171$ GPa (HUNTINGTON, 1958) in the reference crystalline orientation. The mesoscale failure is studied on an artificial 80 grains polycrystalline structure, using the mesh density parameter ρ_d equal to 1.5 and 163,800 DOF, Figure 6.11. An adequate mesh refinement is required to correctly evaluate the distribution of the stress and strain fields, because the energy failure criterion cannot assess the progressive separation process. This structure contains 373 grain boundaries, being necessary to repeat at least 3 times the 101 failure criteria through the material.

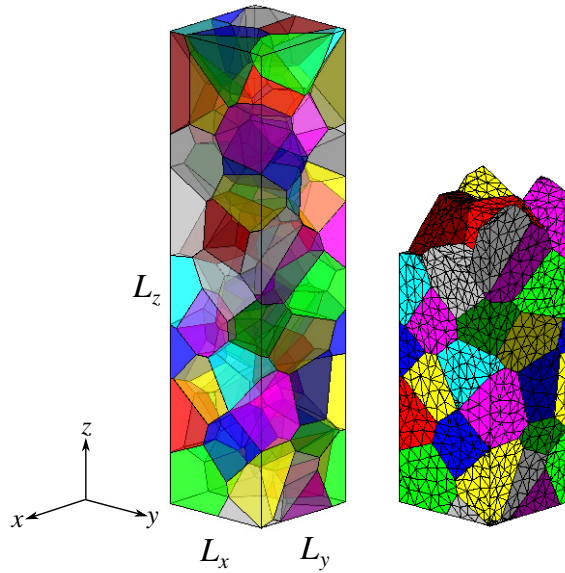


Figure 6.11: Artificial 80 grains polycrystalline structure, discretized with 18,200 boundary elements.

According to physical concepts previously exposed for these materials, some parameters must be established for simulations. As mentioned, the mechanical properties were scaled between nano to microscale limits up to $100 \mu\text{m}$. Then, an adequate intermediate size must be defined for the polycrystal specimen. In the dynamic BEM formulation, the time step $\Delta\tau$ is directly related to the incidence matrices, Equations (3.25), (3.26) and (3.27). Hence, both dimensions and $\Delta\tau$ are fitted simultaneously. After several trials, applying a fully constraint condition at $z = 0$ and a stress-rate of $\dot{\sigma}_{zz}$ at $z = L_z$, the minimum specimen size reached was $L_x = 15 \mu\text{m}$, $L_y = 15 \mu\text{m}$ and $L_z = 65 \mu\text{m}$ with $\Delta\tau = 5$ ns. Using these dimensions, and the mesh density of 1.5, it gives an average length size of each boundary element approximately of $1 \mu\text{m}$, Figure 6.11, as employed in the asymptotic scaling approach. The large number of elements used in this model numerically benefits the reduction of the time step.

As previously discussed, other important factors that contribute to the increment of yield strength are the dynamic boundary conditions. In addition, It can be inferred from the specimen size that the average grain-size will be less than $10 \mu\text{m}$. From the literature, very small grain-sized polycrystalline or nanocrystalline materials exhibit strong mechanical properties and elastic regime (JANG AND ATZMON, 2003; YOUSSEF ET AL., 2005). This is an advantageous fact, because the constitutive model only considers elastic deformation. Although this is not a nanocrystalline model with a yield strength about 5 GPa as simulated by Tong et al. (2015), the elastic regime interval can be assumed high compared to the limit found by Sakui and Sakai (1972) for a $10 \mu\text{m}$ grain-size Fe. Therefore, in the failure process assessment, the use of small grain-sized can justify the imposition of higher deformation, reducing the possibilities to violate the crystal plasticity phenomenon.

Damage is measured at each interface through the simulation time. In order to incorporate the generalized failure criteria shown in Figures 6.9 and 6.10, some additional implementations must be carried out on the overall algorithm presented in Figure 4.6. First, the stress and strain fields are calculated with the surface stress formulation widely explained in (KANE, 1994). It computes these fields directly in the global coordinate system. Next, at each time step, the energy density is evaluated in each node in the local coordinate system. It could be an ambiguous task, because the infinite possibilities to transform the system from local to global and backwards. For that reason, at this stage, it is applied the same $(z - x - z)$ rotation convention that was used for the distribution of the crystalline orientations. Owing to the non-linear elastic behavior caused by the high stress rate, it is not feasible to compute the energy density as usual for quasi-static models. Therefore, an approximation of the storage energy density over time at the k th node is given by

$$E_{ij}^k(t_{n+1}) = \sum_{n=1}^{N_c} E_{ij}^k(t_n) + E_{ij}^k \quad (6.6)$$

where N_c is the number of time steps, and $ij = xz, yz, zz$ at the local coordinates of each interface. The E_{ij}^k term is the current energy assessed by Equation (6.7).

$$E_{ij}^k = \begin{cases} \frac{1}{2} [\sigma_{ij}^k(t_{n+1}) + \sigma_{ij}^k(t_n)] [\varepsilon_{ij}^k(t_{n+1}) - \varepsilon_{ij}^k(t_n)] & \text{if } \begin{cases} \sigma_{ij}^k(t_{n+1}) > \sigma_{ij}^k(t_n) \\ \varepsilon_{ij}^k(t_{n+1}) > \varepsilon_{ij}^k(t_n) \end{cases} \\ E_{ij}^k(t_n) & \text{if other case} \end{cases} \quad (6.7)$$

If the deformation increases through time at the k th node, it is expected a growth in the storage energy that can be interpreted as damage accumulation when the failure criterion Equation (6.4), is applied. For that reason, in order to contemplate the irreversible failure process, if the material point is not deformed at some instant, the stored energy remains constant with its value at the last time step. For illustrative purposes, this simulation procedure can be observed in Figure 6.12.

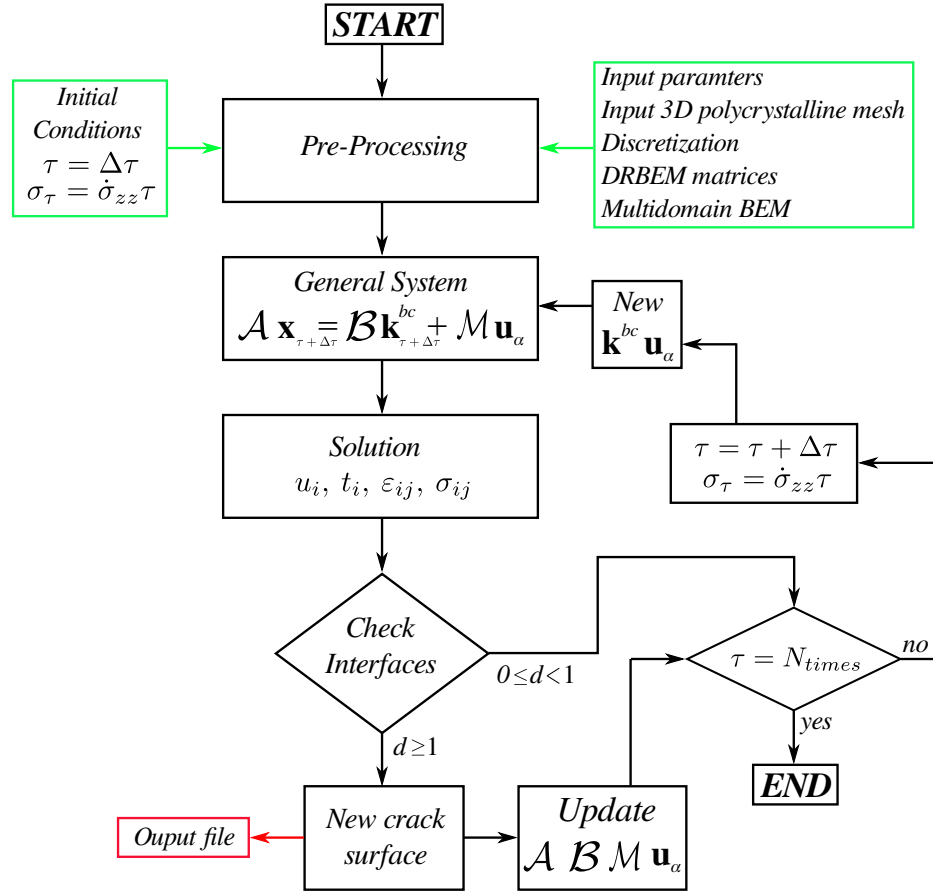


Figure 6.12: Failure algorithm.

After the first step solution, all the interfaces must be checked node by node if it is under traction load, $\sigma_{zz} > 0$. In case of the compressive load $\sigma_{zz} < 0$, it is assumed that $E_n = 0 \text{ MJ/m}^3$. Then, in that case, failure is characterized by the slip condition, because $E_s > 0$. For the shear cases, it is selected the most critical energy between the x^\pm and y^\pm local axes. In this work, the damage d of each pair is measured by

$$d = \frac{E_s}{E_{sc}} + \frac{E_n}{E_{nc}} \quad (6.8)$$

where d lies between 0 and 1. When the pair is totally damaged, the general \mathcal{A} , \mathcal{B} and \mathcal{M} matrices are updated. Owing to the dynamic formulation requiring the displacement response of the last three time steps, the new independent nodes will have the same displacement information for the next time step. Therefore, it is also necessary to update the vector \mathbf{u}_α . Finally, for the new time and load steps, the vectors of boundary conditions \mathbf{k}^{bc} and \mathbf{u}_α are updated.

Now, an intergranular failure simulation is carried out using the 80 grain polycrystal aggregate shown in Figure 6.11. In this case, the stress-rate $\dot{\sigma}_{zz} = 10\text{MPa/ns}$ is imposed at $z = L_z$ and again, the base $z = 0$ is fully constrained. This boundary condition is strong enough to induce the dynamic effects on the specimen with $L_x = 15\ \mu\text{m}$, $L_y = 15\ \mu\text{m}$ and $L_z = 65\ \mu\text{m}$ dimensions. The specimen is subjected to a tensile uniform stress at every time step of 5 ns. In this failure test, a pre-crack was initially created. All interfaces within a defined volume were disconnected forming a weak zone to induce crack propagation, Figure 6.13.

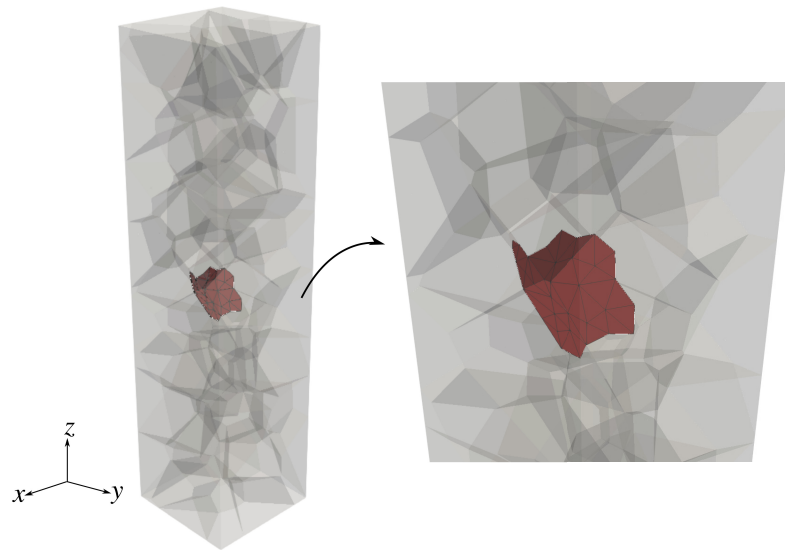


Figure 6.13: Initial cracked model.

For different instants of time, the damage evolution can be appreciated in Figure 6.14.

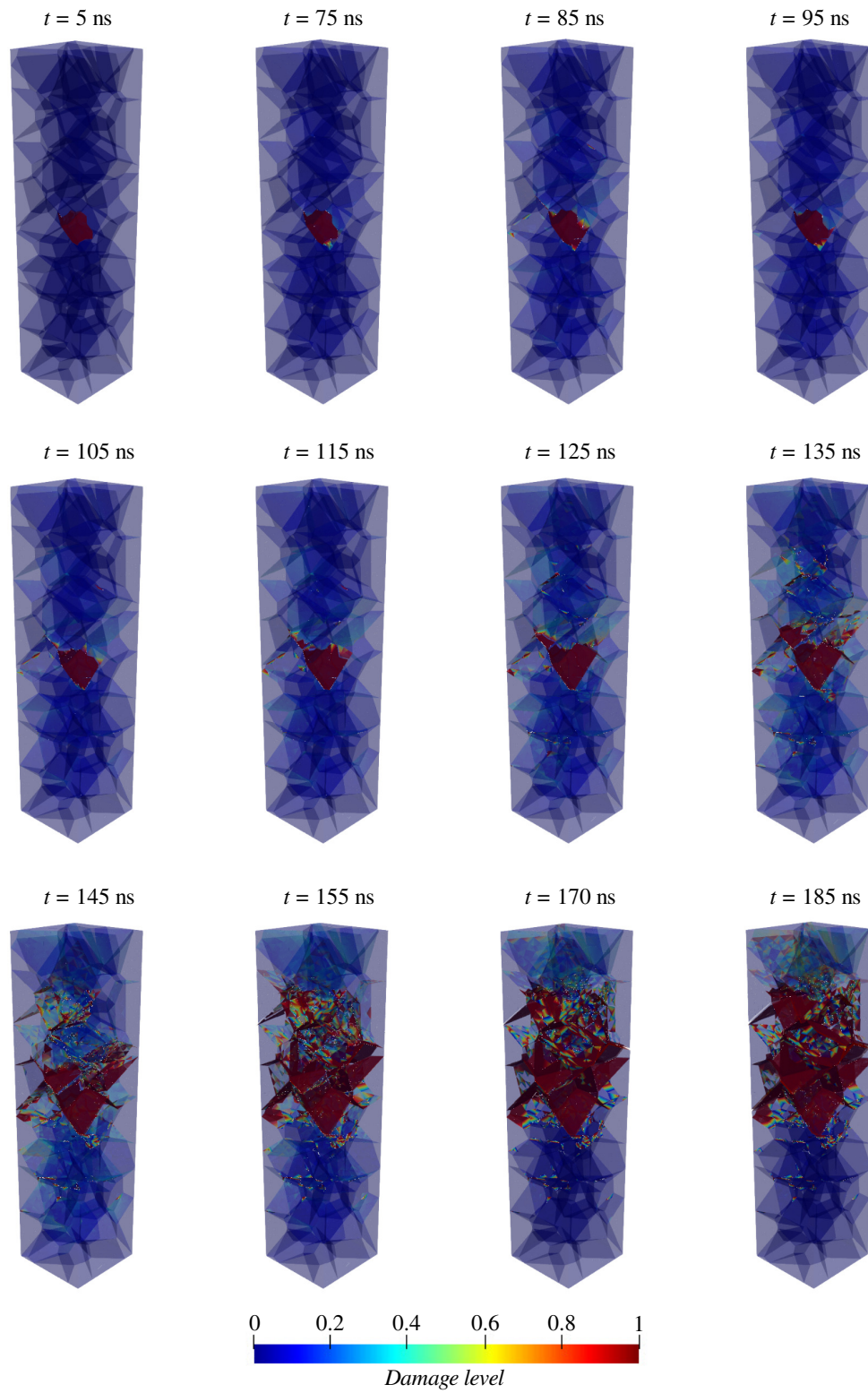


Figure 6.14: Failure propagation and damage evolution.

Despite the linear interpolation of the boundary elements used in the present formulation, the damage variation from 0 to 1 with a color distribution from blue to red is represented for each node. The pre-crack was intentionally located far enough from the boundary, to avoid the influence of the boundary conditions on the failure behavior. It can be observed in Figure 6.14 that the failure initiates at the pre-cracked borders, e.g. at 75 ns. After this time, the failure propagates through the weak zone produced by the initial crack from 75 ns to 105 ns. The deformation level induces failure in additional interfaces for the higher loads and times from 125 ns onwards. Furthermore, the failure criterion established that the failure is more likely to occur under shear loading. This fact was reflected on the obtained results, where the propagation path takes place on tilted interfaces. The sudden failure onsets after 60 ns where the homogenized macro-stress is about 600 MPa, Figure 6.15(a).

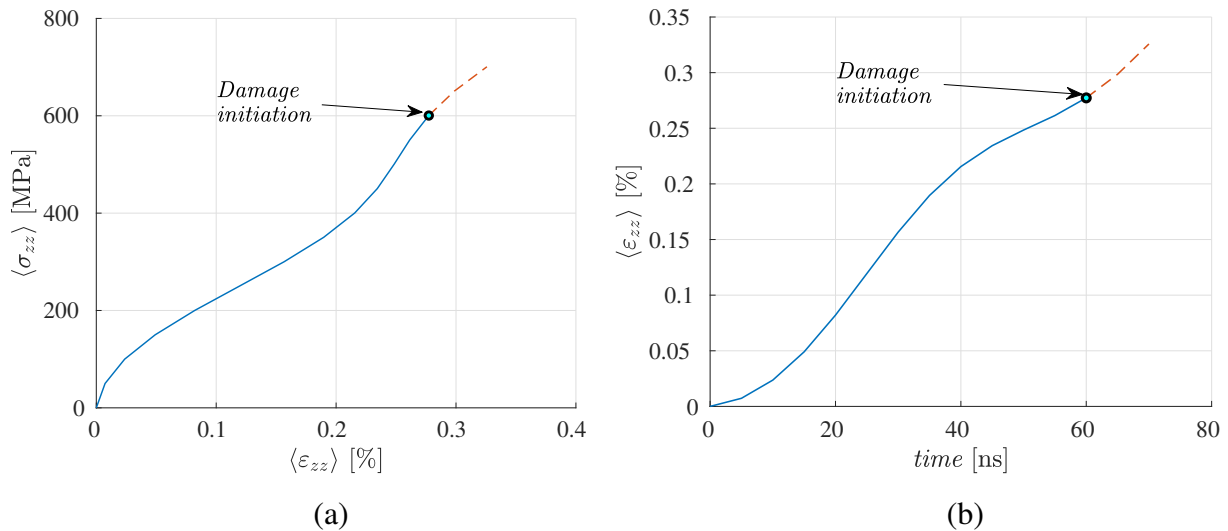


Figure 6.15: Macroscopic behavior: (a) constitutive stress-strain relationship and (b) overall deformation as a function of time.

Due to the application of a very high stress-rate, the inertial effects of mass caused that the elastic regime becomes non-linear. As mentioned, the stress and strain waves progressively propagate through the structure. At the beginning of the time, only a small percentage at the top of the bar is experimenting deformation. If the load is rapidly incremented, the strain wave reflection is not able to comprise the entire specimen length, Figure 6.15(b). The wave propagation can be easily perceived and the total displacement field is observed as illustrated in Figure 6.16.

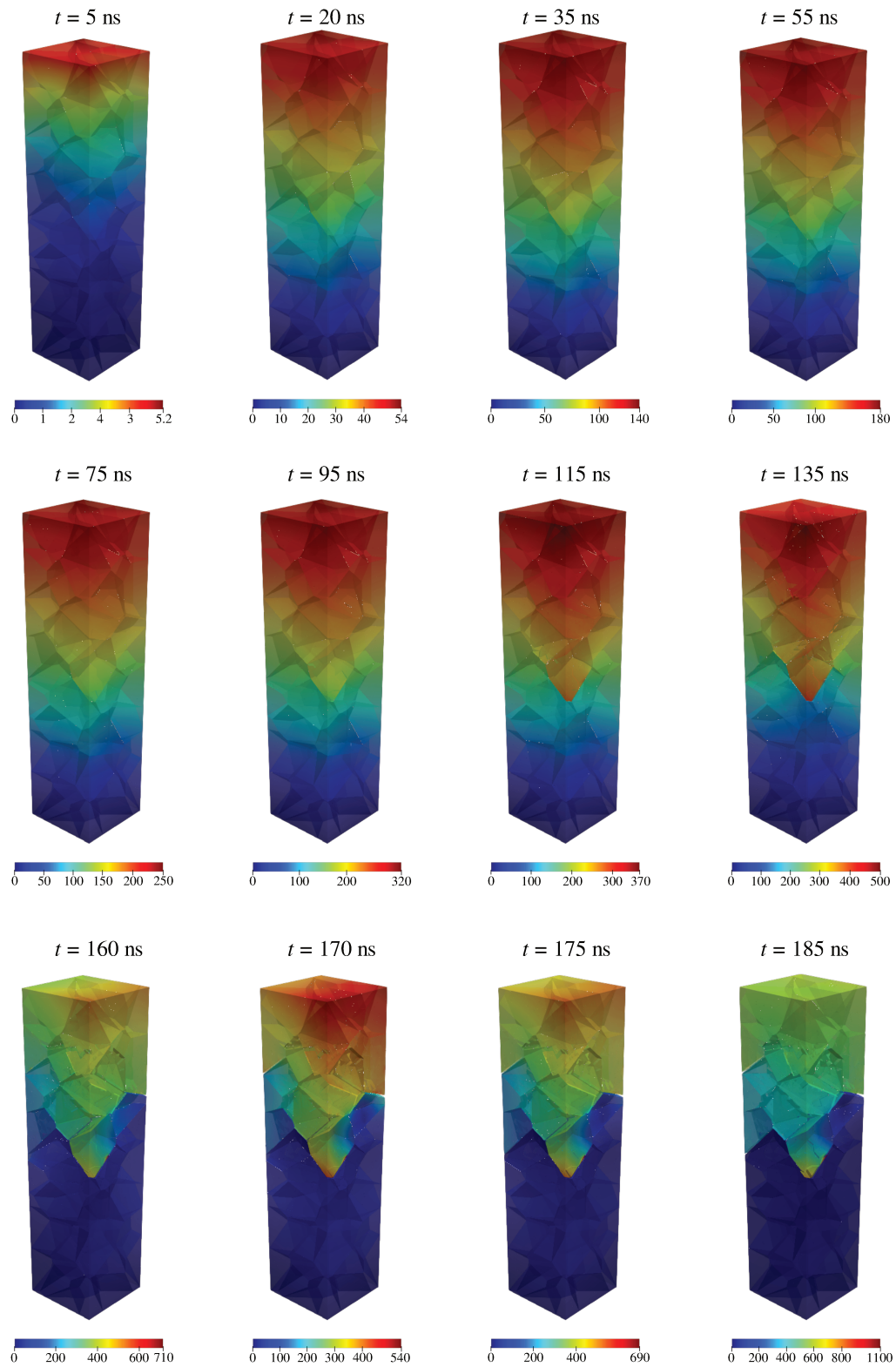


Figure 6.16: Total displacement, units in [nm].

It is worth noting that before 20 ns, the pre-crack is not suffering significant deformation, as the strain wave has not reached that point in the specimen. After 115 ns, specimen separation is more critical owing to the damage level, and also because the stress-rate is not adaptive as commonly used in cohesive analyses. As shown in Figures 6.15(a) and (b), the deformation reached at the damage initiation is 0.3% and the deformation at 185 ns is 0.85%. This deformation interval is high for considering the elastic regime of metallic materials from a quasi-static point of view. Despite the lack of other numerical or experimental results for validation, it can be inferred that the imposition of the stress-rate and length size facilitate the increment of the yield strength, as previously exposed. Moreover, if a small stress-rate is uniformly imposed, the final deformation at e.g. 185 ns will tend to decrease, because of the sudden propagation behavior. In Figure 6.17, the failure is shown at the last simulation time of 185 ns.

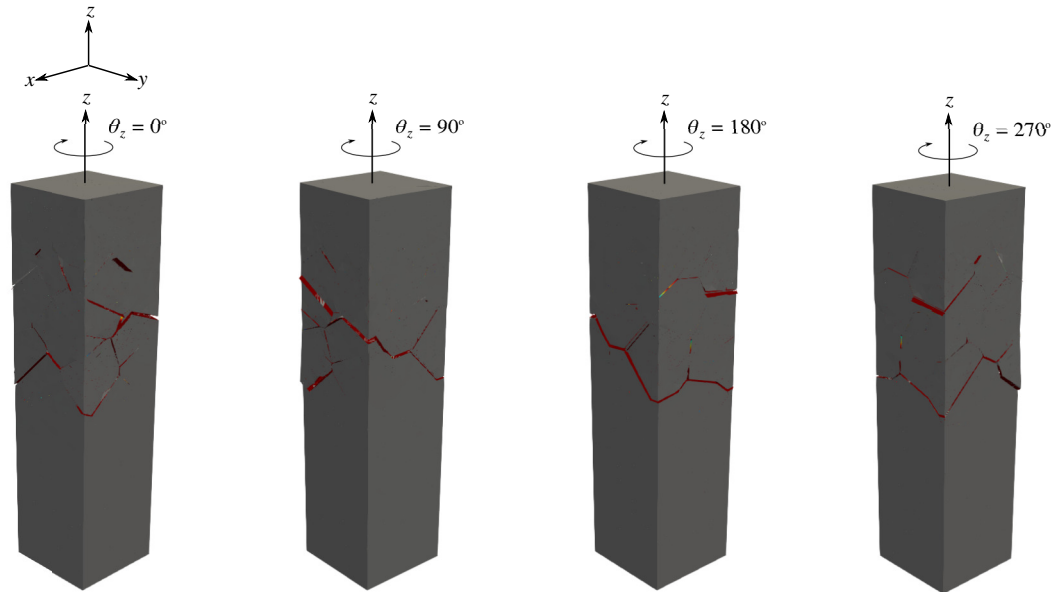


Figure 6.17: Different views of failure at 185 ns.

In terms of implementation, the coupling of the failure criterion to the mesoscale does not represent any additional computational efforts, because the incidence matrices remain constant along the simulations. Furthermore, the general matrix assembly after each pair separation does not require a considerable processing time, even being a serial section of the general BEM algorithm.

7 Conclusions

The analysis of polycrystalline materials with different lattice structures was developed. The constitutive behavior of aggregates was modeled considering random crystalline orientations. Using the elastostatic BEM formulation with the fundamental solution based on double Fourier series and the multidomain algorithm, numerical solutions of displacement and traction fields were calculated. The morphology accuracy in the discretization process was adequate to avoid singular responses from the numerical method applied. In addition, regular grain volumes, surfaces and triangular elements were imposed. A database of materials to be analysed was generated for a set of aggregates in this work.

The effective elastic properties of aggregates were assessed. While the number of grains increases, the constitutive macroscopic response proved to become more isotropic. Specimens from 18 to 210 grains were evaluated, leading to a considerable reduction in the deviation and mean values of the elastic properties, reflecting the increment of isotropy level. As validation, comparisons with analytical, numerical and experimental data previously published in the literature were carried out, in which results showed good agreement and small error values from 0.02% to 9.88%. In addition, results were obtained as expected according to the new anisotropy factor used (KUBE, 2016).

The dynamic transient behavior of polycrystalline materials with different lattice structures was analyzed. In this work, a framework was proposed to validate heterogeneous 3D anisotropic elastic materials under high-rate dynamic loads. The effective macroscopic elastic properties were used to achieve this validation framework. Numerical results showed deviations when the time increased, especially for boundary conditions that produced gradient discontinuities at instants of time in the response. This dynamic analysis is a general application that provides an initial scheme for future analyses of anisotropic microscopic heterogeneous materials, which can be validated using the homogenized scheme presented here. Several dynamic boundary conditions can produce critical behavior of a solid, such as shown in Figure 4.9 for the harmonic load. This analysis paves the way for future studies of dynamic failure of elastic materials under collapse conditions with different heterogeneous microstructures.

Intergranular failure at the mesoscale was assessed under dynamic boundary conditions. The failure criterion based on the energy densities was generated considering a sample of 101 GBs using a nanoscale MD model. It evidenced the influence of the crystalline orientation on the cri-

tical energy densities for shear and tensile modes. Moreover, different brittle and ductile failure levels could be analyzed from the GB energy concept, because the GBs with higher energies are directly related to the more ductile nanoscopic specimens. From these results, it was found that in the GB plane, the shear slip condition is more critical than cleavage causing a more rapid failure with less stored energy density. The nanoscale mechanical behavior could not be directly coupled to the microscale model. Then, an asymptotic analysis was employed from models proposed in the literature. It was assumed that all GB results in the nanoscale can compose an heterogeneous random material, constituted as the average of the size length and yield strength of each GB. Therefore, the yield strength was scaled between similar material structures from nano to microscale. This strategy helped to maintain the scattered character of the GBs to be used in the polycrystal aggregate. The last stage was the incorporation of the complete failure criterion on the mesoscale to finally simulate the intergranular failure. Some basic implementations were required and added to the BEM numerical model. The intergranular failure was predominantly caused by the shear fields at the interfaces. From these results, it can be concluded that, the inertia effects provoke a non-linear elastic behavior.

The proposed multiscale approach using BEM and MD demonstrated the capability to evaluate intergranular failure taking into account the limits between the elastic and plastic regimes. If an adequate MD model is implemented, the interface material properties can be found allowing to include additional physical phenomena in the overall multiscale model. Therefore, this model serves to pave the way for further research. In order to improve the overall approach some aspects are essential, such as:

- The inclusion of crystal plasticity and contact analyses in the BEM model. It will be able to work with high deformations and the evaluation of shear and compressive impact tests in the mesoscale. In addition, the implementation of thermoelastic BEM analysis, owing to the strong dependence of the mechanical and anisotropic elastic properties on the temperature. These material properties need to be computed via the MD model.
- The generation of a proper set of functions to scale the mechanical strength from nano to micro scales. These functions must depend on the GB crystalline orientation. In order to perform this scaling approach, nanospecimens up to millions of atoms have to be considered. This model could require a huge amount of computational sources. An alternative option can be considered if an intermediate scale is analyzed between nano and micro using the dislocation dynamics method.

References

- Ackland, G. J., Bacon, D. J., Calder, A. F., and Harry, T. (1997). Computer simulation of point defect properties in dilute Fe-Cu alloy using a many-body interatomic potential. *Philosophical Magazine A*, 75(3):713–732.
- Albuquerque, E. L., Sollero, P., and Aliabadi, M. H. (2002). The boundary element method applied to time dependent problems in anisotropic materials. *International Journal of Solids and Structures*, 39:1405–1422.
- Albuquerque, E. L., Sollero, P., and Aliabadi, M. H. (2004). Dual boundary element method for anisotropic dynamic fracture mechanics. *International Journal for Numerical Methods in Engineering*, 59:1187–1205.
- Amestoy, P. R., Duff, I. S., Koster, J., and L'Excellent, J.-Y. (2001). A fully asynchronous multi-frontal solver using distributed dynamic scheduling. *SIAM Journal on Matrix Analysis and Applications*, 23(1):15–41.
- Amestoy, P. R., Guermouche, A., L'Excellent, J.-Y., and Pralet, S. (2006). Hybrid scheduling for the parallel solution of linear systems. *Parallel Computing*, 32(2):136–156.
- Ballo, P. (2001). Grain boundary sliding and migration: Effect of temperature and vacancies. *Physical Review B*, 64:024104–7.
- Barnett, D. M. (1972). The precise evaluation of derivatives of the anisotropic elastic Green's functions. *Physics State Solid*, 49:741–748.
- Barrows, W., Dingreville, R., and Spearot, D. (2016). Traction–separation relationships for hydro-

gen induced grain boundary embrittlement in nickel via molecular dynamics simulations. *Materials Science and Engineering: A*, 650:354–364.

Baskes, M. F. H. M. I. and Plimpton, S. J. (2001). Length scale and time scale effects on the plastic flow of FCC metals. *Acta Materialia*, 49:4363–4374.

Bazant, Z. P. (1993). Scaling laws in mechanics of failure. *Journal of Engineering Mechanics*, 119(9):1828–1844.

Bazant, Z. P. (2002). Scaling of dislocation-based strain-gradient plasticity. *Journal of the Mechanics and Physics of Solids*, 50:435–448.

Beckmann, C. and Hohe, J. (2017). Modeling transgranular crack growth in random 3D grain structures under cyclic loading. *Probabilistic Engineering Mechanics*, 50:45–52.

Benedetti, I. and Aliabadi, M. (2013a). A three-dimensional cohesive-frictional grain-boundary micromechanical model for intergranular degradation and failure in polycrystalline materials. *Computer Methods in Applied Mechanics and Engineering*, 265:36–62.

Benedetti, I. and Aliabadi, M. (2015). Multiscale modeling of polycrystalline materials: A boundary element approach to material degradation and fracture. *Computer Methods in Applied Mechanics and Engineering*, 289:429–453.

Benedetti, I. and Aliabadi, M. H. (2013b). A three-dimensional grain boundary formulation for microstructural modeling of polycrystalline materials. *Computational Materials Science*, 67:249–260.

Benedetti, I., Gulizzi, V., and Milazzo, A. (2018). Grain-boundary modelling of hydrogen assisted intergranular stress corrosion cracking. *Mechanics of Materials*, 117:137–151.

Beran, M. J., Masin, T. A., Adams, B. L., and Olsen, T. (1996). Bounding elastic constants of an orthotropic polycrystal using measurements of the microstructure. *Journal of the Mechanics and*

Physics of Solids, 44(9):1543–1563.

Biersack, J. P. and Ziegler, J. F. (1982). Refined universal potentials in atomic collisions. *Nuclear Instruments and Methods*, 194:93–100.

Bitzek, E., Koskinen, P., Gähler, F., Moseler, M., and Gumbsch, P. (2006). Structural relaxation made simple. *Physical Review Letters*, 97:170201–4.

Briant, C. L. (2001). Grain boundary structure, chemistry, and failure. *Materials Science and Technology*, 17(11):1317–1323.

Brommesson, R., Ekh, M., and Joseph, C. (2016). 3D grain structure modelling of intergranular fracture in forged Haynes 282. *Engineering Fracture Mechanics*, 154:57–71.

Cabané-Brouty, F. and Bernardini, J. (1982). Segregation and diffusion. *Journal de Physique Colloques*, 43(C6):163–176.

Chen, Z., Gan, Y., and Shen, L. M. (2007). *Multiscale in Molecular and Continuum Mechanics: Interaction of Time and Size from Macro to Nano*, chapter Combined loading rate and specimen size effects on the material properties, pages 67–84. Springer.

Chen, Z., Shen, L., and Fang, H. E. (2005). Hypersurface for the combined loading rate and specimen size effects on material properties. *International Journal for Multiscale Computational Engineering*, 3(4):451–461.

Chung, D. H. and Buessem, W. R. (1967). The elastic anisotropy of crystals. *Journal of Applied Physics*, 38:2010–2012.

Clough, R. and Penzien, J. (2003). *Dynamic of Structures*. Computers & Structures, Inc, Berkeley, Third edition.

- Daw, M. S. and Baskes, M. I. (1983). Semiempirical, quantum mechanical calculation of hydrogen embrittlement in metals. *Physical Review Letters*, 50(17):1285–1288.
- Dingreville, R., Aksoy, D., and Spearot, D. E. (2017). A primer on selecting grain boundary sets for comparison of interfacial fracture properties in molecular dynamics simulations. *nature: Scientific Reports*, 7:8332–12.
- Djan, E. K. (2016). *Development of generic grain refiner alloys for cast and wrought Al-alloys containing silicon and zirconium*. PhD thesis, Brunel University London.
- Dominguez, J. (1993). *Boundary Elements in Dynamics*. Computational Mechanics Publications, Southampton.
- Fedorov, F. I. (1968). *Theory of Elastic Waves in Crystals*. Plenum, New York.
- Finnis, M. W. and Sinclair, J. E. (1984). A simple empirical N -body potential for transition metals. *Philosophical Magazine A*, 50(1):45–55.
- Fletcher, N. H. (1971). *Advances in Materials Research*, chapter Crystal interface models – a critical survey, page 281–314. Wiley, New York.
- Fritzen, F., Ilke, T., and Schnack, E. (2009). Periodic three-dimensional mesh generation for crystalline aggregates based on Voronoi tessellation. *Computational Mechanics*, 43:701–713.
- Galvis, A. F., Rodriguez, R. Q., and Sollero, P. (2018a). Analysis of three-dimensional hexagonal and cubic polycrystals using the boundary element method. *Mechanics of Materials*, 117:58–72.
- Galvis, A. F., Rodriguez, R. Q., and Sollero, P. (2018b). Dynamic analysis of three-dimensional polycrystalline materials using the boundary element method. *Computers & Structures*, 200:11–20.
- Gao, H., Huang, Y., Nix, W. D., and Hutchinson, J. W. (1999). Mechanism-based strain gradient

- plasticity-I. Theory. *Journal of the Mechanics and Physics of Solids*, 47:1239–1263.
- Gao, X. W. (2002). The radial integration method for evaluation of domain integrals with boundary-only discretization. *Engineering Analysis with Boundary Elements*, 26:905–916.
- Gao, Y. and Jin, Z. (2017). Interaction between lattice dislocations and low-angle grain boundaries in Ni via molecular dynamics simulations. *Molecular Simulation*, 43:1172–1178.
- Gaul, L., Kögl, M., and Wagner, M. (2003). *Boundary Element Method for Engineers and Scientists*. Springer, Berlin.
- Gitman, I. M., Askes, H., and Sluys, L. J. (2007). Representative volume: existence and size determination. *Engineering Fracture Mechanics*, 74:2518–2534.
- Goldstein, H., Poole, C., and Safko, J. (2002). *Classical Mechanics*. Addison Wesley, New York, Third edition.
- Griebel, M., Knapek, S., and Zumbush, G. (2010). *Numerical Simulation in Molecular Dynamics*. Springer, Berlin.
- Gross, D. and Seelig, T. (2006). *Fracture Mechanics With an Introduction to Micromechanics*. Springer-Verlag, Berlin.
- Gulizzi, V., Milazzo, A., and Benedetti, I. (2015). An enhanced grain-boundary framework for computational homogenization and micro-cracking simulations of polycrystalline materials. *Computational Mechanics*, 56:631–651.
- Gulizzi, V., Rycroft, C. H., and Benedetti, I. (2018). Modelling intergranular and transgranular micro-cracking in polycrystalline materials. *Computer Methods in Applied Mechanics and Engineering*, 329:168–194.

Guo, Y., Zhuang, Z., Li, X. Y., and Chen, Z. (2007). An investigation of the combined size and rate effects on the mechanical responses of FCC metals. *International Journal of Solids and Structures*, 44:1180–1195.

Gurav, S., Sasmile, N., and Dharia, S. (2015). A case study on use of polycrystalline materials in manufacturing processes. *International Journal of Science and Engineering*, 3:48–56.

Hammami, F. and Kulkarni, Y. (2017). Rate dependence of grain boundary sliding via time-scaling atomistic simulations. *Journal of Applied Physics*, 121:085303–5.

Hill, R. (1952). The elastic behavior of crystalline aggregate. *Proceedings of the Physical Society, Section A*, 65(5):349–354.

Hill, R. (1963). Elastic properties of reinforced solids: Some theoretical principles. *Journal of the Mechanics and Physics of Solids*, 11:357–372.

Hockney, R. W. (1970). The potential calculation and some applications. *Methods in Computational Physics*, 9:136–21.

Horstemeyer, M. F. and Baskes, M. I. (1999). Atomistic finite deformation simulations: A discussion on length scale effects in relation to mechanical stresses. *Journal of Engineering Materials and Technology*, 121(2):114–119.

Houbolt, J. C. (1950). A recurrence matrix solution for the dynamic response of elastic aircraft. *Journal of Aeronautical and Science*, 17 (9):540–550.

Hummer, G. and Gronbech-Jensen, N. (1998). Pressure calculation in polar and charged systems using Ewald summation: Results for the extended simple point charge model of water. *The Journal of Chemical Physics*, 109(7):2791–2797.

Humphreys, D. D., Friesner, R. A., and Berne, B. J. (1994). A multiple-time-step molecular dynamics algorithm for macromolecules. *The Journal of Physical Chemistry*, 98:6885–6892.

Hünenberger, P. H. (2002). Calculation of the group-based pressure in molecular simulations. I. A general formulation including Ewald and particle-particle–particle-mesh electrostatics. *The Journal of Chemical Physics*, 116(16):6880–6897.

Huntington, H. B. (1958). *The Elastic Constants of Crystals*. Academic Press Inc, New York.

Jang, D. and Atzmon, M. (2003). Grain-size dependence of plastic deformation in nanocrystalline Fe. *Journal of Applied Physics*, 93(11):9282–9286.

Kane, J. H. (1994). *Boundary Element Analysis In Engineering Continuum Mechanics*. Prentice-Hall, New Jersey.

Katsikadelis, J. T. (2002). *Boundary Elements: Theory and Applications*. Elsevier, Oxford.

Kiewel, H., Bunje, H. J., and Fritsche, L. (1996). Effect of the grain shape on the elastic constants of polycrystalline materials. *Textures and Microstructures*, 28:17–33.

Kögl, M. and Gaul, L. (2000a). A 3-D boundary element method for dynamic analysis of anisotropic elastic solids. *CMES: Computer Modeling in Engineering & Science*, 1 no 4:27–43.

Kögl, M. and Gaul, L. (2000b). A boundary element method for transient piezoelectric analysis. *Engineering Analysis with Boundary Elements*, 24:591–598.

Kögl, M. and Gaul, L. (2003). Free vibration analysis of anisotropic solids with the boundary element method. *Engineering Analysis with Boundary Elements*, 27:107–114.

Kowalczyk-Gajewska, K. and Ostrowska-Maciejewska, J. (2009). Review on spectral decomposition of Hooke's tensor for all symmetric groups of linear elastic material. *Engineering Transactions*, 57:145–183.

Kröner, E. (1977). Bounds for effective elastic moduli of disordered materials. *Journal of the*

Mechanics and Physics of Solids, 25:137–155.

Kube, C. M. (2016). Elastic anisotropy of crystals. *AIP Advances*, 6:095209–6.

Leimkuhler, B. and Matthews, C. (2015). *Molecular Dynamics With Deterministic and Stochastic Numerical Methods*. Springer Cham Heidelberg, New York.

Lejcek, P. (2010). *Grain Boundary Segregation in Metals*, chapter Grain Boundaries: Description, Structure and Thermodynamics, pages 5–24. Springer Heidelberg, London.

Li, B. Q. and Reynolds, A. P. (1998). Correlation of grain-boundary precipitates parameters with fracture toughness in an Al–Cu–Mg–Ag alloy subjected to long-term thermal exposure. *Journal of Materials Science*, 33:5849–5853.

Li, Q. M. (2001). Strain energy density failure criterion. *International Journal of Solids and Structures*, 38:6997–7013.

Lifshitz, I. M. and Rozenzweig, L. N. (1947). Construction of the green tensor for the fundamental equation of elasticity theory in the case of unbounded elastic anisotropic medium. *Zhurnal Éksperimental'noi i Teoreticheskoi Fiziki*, 17:783–791.

Liu, C. (2005). On the minimum size of representative volume element: an experimental investigation. *Experimental Mechanics*, 45(3):238–243.

Luther, T. and Könke, C. (2011). Coupled cohesive zone representations from 3D quasicontinuum simulation on brittle grain boundaries. *Journal for Multiscale Computational Engineering*, 9(4):481–501.

Martyna, G. J., Tobias, D. J., and Klein, M. L. (1994). Constant pressure molecular dynamics algorithms. *The Journal of Chemical Physics*, 101(1):4177–4189.

Mendelev, M. I., Han, S., and Srolovitz, D. J. (2003). Development of new interatomic potentials appropriate for crystalline and liquid iron. *Philosophical Magazine*, 83(35):3977–3994.

Meyers, M. A. (1994). *Dynamic Behavior of Materials*. John Wiley & Sons, Inc, New York.

Nguyen, T. T., Réthoré, J., Yvonnet, J., and Baietto, M. C. (2017). Multi-phase-field modeling of anisotropic crack propagation for polycrystalline materials. *Computational Mechanics*, 60:289–314.

Nosé, S. (1984). A molecular dynamics method for simulations in the canonical ensemble. *Molecular Physics*, 52(2):255–268.

Ogawa, H. (2006). GBstudio: A Builder software on periodic models of CSL boundaries for molecular simulation. *Materials Transactions*, 47(11):2706–2710.

Oliva, B. and Hünenberger, P. H. (2002). Calculation of the group-based pressure in molecular simulations. II. Numerical tests and application to liquid water. *The Journal of Chemical Physics*, 116(16):6898–6909.

Ostoja-Starzewski, M. (2006). Material spatial randomness: From statistical to representative volume element. *Probabilistic Engineering Mechanics*, 21:112–132.

Paliwal, B. and Cherkaoui, M. (2013). An improved atomistic simulation based mixed-mode cohesive zone law considering non-planar crack growth. *International Journal of Solids and Structures*, 50:3346–3360.

Parrinello, M. and Rahman, A. (1981). Polymorphic transitions in single crystals: A new molecular dynamics method. *Journal of Applied Physics*, 52(12):7182–7190.

Plimpton, S. (1995). Fast parallel algorithms for short-range molecular dynamics. *Journal of Computational Physics*, 117:1–19.

Polak, E. and Ribière, G. (1969). Note sur la convergence de méthodes de directions conjuguées. *Revue française d'informatique et de recherche opérationnelle, série rouge*, 3(1):35–43.

Prakash, C., Lee, H., Alucozai, M., and Tomar, V. (2016). An analysis of the influence of grain boundary strength on microstructure dependent fracture in polycrystalline tungsten. *International Journal of Fracture*, 199:1–20.

Press, W. H., Teukolsky, S. A., Vetterling, W. T., and Flannery, B. P. (1992). *Numerical Recipes in C: The Art of Scientific Computing*. University of Cambridge Press, Cambridge, Second edition.

Qu, R. T., Zhang, Z. J., Zhang, P., Liu, Z. Q., and Zhang, Z. F. (2016). Generalized energy failure criterion. *nature : Scientific Reports*, 6:23359–8.

Quey, R. and Renversade, L. (2018). Optimal polyhedral description of 3D polycrystals: Method and application to statistical and synchrotron X-ray diffraction data. *Computer Methods in Applied Mechanics and Engineering*, 330:308–333.

Ranganathan, S. I. and Ostoja-Starzewski, M. (2008). Universal elastic anisotropy index. *Physical Review Letters*, 101:055504.

Ren, B. and Li, S. (2013). A three-dimensional atomistic-based process zone model simulation of fragmentation in polycrystalline solids. *International Journal for Numerical Methods in Engineering*, 93:989–1014.

Ren, Z. Y. and Zheng, Q. S. (2002). A Quantitative study of minimum sizes of representative volume elements of cubic polycrystals—numerical experiments. *Journal of the Mechanics and Physics of Solids*, 50:881–893.

Ren, Z. Y. and Zheng, Q. S. (2004). Effects of grain sizes, shapes, and distribution on minimum sizes of representative volume elements of cubic polycrystals. *Mechanics of Materials*, 36:1217–1229.

Reuss, A. (1929). Berechnung der fließgrenze von mischkristallen auf grund der plastizitätsbedingung für einkristalle. *Zeitschrift für Angewandte Mathematik und Mechanik*, 9:49–58.

Rittner, J. D. and Seidman, D. N. (1996). $\langle 110 \rangle$ symmetric tilt grain-boundary structures in fcc metals with low stacking-fault energies. *Physical Review B*, 54(10):6999–7015.

Rodríguez, R. (2016). *Multiscale failure analysis of laminated composites using the boundary element method*. PhD thesis, University of Campinas.

Rodríguez, R., Galvis, A. F., Sollero, P., Tan, C. L., and Albuquerque, E. L. (2018). Transient dynamic analysis of generally anisotropic materials using the boundary element method. *Acta Mechanica*, 229:1893–1910.

Rodríguez, R. Q., Galvis, A. F., Sollero, P., Tan, C. L., and Albuquerque, E. L. (2017). Fast BEM multi-domain approach for the elastostatic analysis of short fibre composites. *European Journal of Computational Mechanics*, 26(5-6):525–540.

Rouvierea, J. L., Rousseau, K., Fournel, F., and Moriceau, H. (2000). Huge differences between low- and high-angle twist grain boundaries: The case of ultrathin (001) Si films bonded to (001) Si wafers. *Applied Physics Letters*, 77(8):1135–1137.

Runnels, B., Beyerlein, I. J., and Ortiz, S. C. M. (2016). A relaxation method for the energy and morphology of grain boundaries and interfaces. *Journal of the Mechanics and Physics of Solids*, 94:338–408.

Rycroft, C. H. (2007). *Multiscale Modeling in Granular Flow*. PhD thesis, Massachusetts Institute of Technology.

Rycroft, C. H. (2009). Voro++: A three-dimensional Voronoi cell library in C++. *Chaos*, 19:041111–1.

Rycroft, C. H., Grest, G. S., Landry, J. W., and Bazant, M. Z. (2006). Analysis of granular flow in

a pebble-bed nuclear reactor. *Physical Review*, 74:021306–16.

Sakui, S. and Sakai, T. (1972). The effect of strain rate, temperature and grain size on the lower yield stress and flow stress of polycrystalline pure iron. *J-STAGE*, 58(10):1438–1455.

Salahouelhadj, A. and Haddadi, H. (2010). Estimation of the size of the RVE for isotropic copper polycrystals by using elastic–plastic finite element homogenisation. *Computational Materials Science*, 48:447–455.

Sangid, M. D., Sehitoglu, H., Maier, H. J., and Niendorf, T. (2010). Grain boundary characterization and energetics of superalloys. *Materials Science and Engineering A*, 527:7115–7125.

Schneider, T. and Stoll, E. (1978). Molecular-dynamics study of a three-dimensional one-component model for distortive phase transitions. *Physical Review B*, 17(3):1302–1322.

Sheppard, D., Terrell, R., and Henkelman, G. (2008). Optimization methods for finding minimum energy paths. *The Journal of Chemical Physics*, 128:134106–10.

Shewchuk, J. R. (1996). *Applied Computational Geometry Towards Geometric Engineering*, chapter Triangle: Engineering a 2D Quality Mesh Generator and Delaunay Triangulator, pages 203–222. Springer, Philadelphia.

Shi, A. C., Rottman, C., and He, Y. (1989). Calculation of energy of low-angle grain boundaries. *Philosophical Magazine A*, 55(4):499–511.

Shiah, Y. C. and Tan, C. L. (2011). Higher-order Green’s function derivatives and BEM evaluation of stress at interior points in a 3D generally anisotropic solids. *CMES: Computer Modeling in Engineering & Science*, 78(2):95–108.

Shiah, Y. C., Tan, C. L., and Lee, V. G. (2008). Evaluation of explicit-form fundamental solutions for displacements and stresses in 3D anisotropic elastic solids. *CMES: Computer Modeling in Engineering & Science*, 34(3):205–226.

Shiah, Y. C., Tan, C. L., and Wang, C. Y. (2012). Efficient computation of the Green's function and its derivatives for three-dimensional anisotropic elasticity in BEM analysis. *Engineering Analysis with Boundary Elements*, 36:1746–1755.

Shinoda, W., Shiga, M., and Mikami, M. (2004). Rapid estimation of elastic constants by molecular dynamics simulation under constant stress. *Physical Review B*, 69:134103–8.

Steele, D., Evans, D., Nolan, P., and Lloyd, D. J. (2007). Quantification of grain boundary precipitation and the influence of quench rate in 6XXX aluminum alloys. *Materials Characterization*, 58:40–45.

Sundararaghavan, V. and Zabarav, N. (2008). A statistical learning approach for the design of polycrystalline materials. *Statistical Analysis and Data Mining*, 1no. 5:306–321.

Swope, W. C., Andersen, H. C., Berens, P. H., and Wilson, K. R. (1982). A computer simulation method for the calculation of equilibrium constants for the formation of physical clusters of molecules: Application to small water clusters. *The Journal of Chemical Physics*, 76:637–649.

Synge, J. L. (1957). *The Hypercircle in Mathematical Physics*. Cambridge University Press, Cambridge.

Talebi, H., Silani, M., and Rabczuk, T. (2015). Concurrent multiscale modeling of three dimensional crack and dislocation propagation. *Advances in Engineering Software*, 80:82–92.

Tan, C. L., Shiah, Y. C., and Wang, C. Y. (2013). Boundary element elastic stress analysis of 3D generally anisotropic solids using fundamental solutions based on Fourier series. *International Journal of Solids and Structures*, 50:2701–2711.

Thompson, A. P., Plimpton, S. J., and Mattson, W. (2009). General formulation of pressure and stress tensor for arbitrary many-body interaction potentials under periodic boundary conditions. *The Journal of Chemical Physics*, 131:154107–6.

Ting, T. C. T. and Lee, V. G. (1997). The three-dimensional elastostatic Green's function for general anisotropic linear elastic solids. *The Quarterly Journal of Mechanics & Applied Mathematics*, 50:407–426.

Tong, X., Zhang, H., and Li, D. Y. (2015). Effect of annealing treatment on mechanical properties of nanocrystalline α -iron: an atomistic study. *nature: Scientific Reports*, 5:8459–7.

Toxvaerd, S., Heilmann, O. J., and j. C. Dyre (2012). Energy conservation in molecular dynamics simulations of classical systems. *The Journal of Chemical Physics*, 136:224106–8.

Tromans, D. (2011). Elastic anisotropic of HCP metal crystals and polycrystals. *International Journal of Research and Reviews in Applied Sciences*, 6(4):462–483.

Tschopp, M. A., Coleman, S. P., and McDowell, D. L. (2015). Symmetric and asymmetric tilt grain boundary structure and energy in Cu and Al (and transferability to other fcc metals). *Integrating Materials and Manufacturing Innovation*, 4(11):1–14.

Tschopp, M. A. and McDowell, D. L. (2007a). Asymmetric tilt grain boundary structure and energy in copper and aluminium. *Philosophical Magazine*, 87(25):3871–3892.

Tschopp, M. A. and McDowell, D. L. (2007b). Structures and energies of $\Sigma 3$ asymmetric tilt grain boundaries in copper and aluminium. *Philosophical Magazine*, 87(22):3147–3173.

Tschopp, M. A., Solanki, K. N., Gao, F., Sun, X., Khaleel, M. A., and Horstemeyer, M. F. (2012). Probing grain boundary sink strength at the nanoscale: Energetics and length scales of vacancy and interstitial absorption by grain boundaries in α -Fe. *Physical Review B*, 85:064108–21.

Tuckerman, M. and Berne, B. J. (1992). Reversible multiple time scale molecular dynamics. *The Journal of Chemical Physics*, 97(3):1990–2001.

Tuckerman, M. E., Alejandre, J., López-Rendón, R., Jochim, A. L., and Martyna, G. J. (2006). A liouville-operator derived measure-preserving integrator for molecular dynamics simulations in the

- isothermal–isobaric ensemble. *Journal of Physics A: Mathematical and General*, 39:5629–5651.
- van Beers, P., Kouznetsova, V., Geers, M., Tschopp, M., and McDowell, D. (2015). A multiscale model of grain boundary structure and energy: From atomistics to a continuum description. *Acta Materialia*, 82:513–529.
- Verlet, L. (1967). Computer "experiments" on classical fluids. I. Thermodynamical properties of Lennard-Jones molecules. *Physical Review*, 159(1):98–103.
- Voigt, W. (1889). Ueber die beziehung zwischen den beiden elasticitätsconstanten isotroper körper. *annalen der physik*, 38:573–587.
- Watanabe, T., Arai, K. I., and Yoshimi, K. (1989). Texture and grain boundary character distribution (GBCD) in rapidly solidified and annealed Fe-6.5mass%Si ribbons. *Philosophical Magazine Letters*, 59(2):47–52.
- Williams, J. and Starke, E. (2003). Progress in structural materials for aerospace systems. *Acta Materialia*, 51:5775–5799.
- Wilson, R. B. and Cruse, T. A. (1978). Efficient implementation of anisotropic three dimensional boundary integral equation stress analysis. *International Journal for Numerical Methods in Engineering*, 12:1383–1397.
- Wolf, D. (1991). Structure and energy of general grain boundaries in bcc metals. *Journal of Applied Physics*, 69(1):185–196.
- Xu, X. F. and Chen, X. (2009). Stochastic homogenization of random elastic multi-phase composites and size quantification of representative volume element. *Mechanics of Materials*, 41:174–186.
- Yamakov, V., Saether, E., and Glaessgen, E. H. (2008). Molecular modeling of intergranular fracture in aluminum: constitutive relation for interface debonding. *Journal of Materials Science*, 43:7488–7494.

Yazyev, O. and Chen, Y. (2014). Polycrystalline graphene and other two-dimensional materials. *nature nanotechnology*, 9:755–767.

Youssef, K. M., Scattergood, R. O., Murty, K. L., Horton, J. A., and Koch, C. C. (2005). Ultrahigh strength and high ductility of bulk nanocrystalline copper. *Applied Physics Letters*, 87:091904–3.

Zener, C. M. (1948). *Elasticity and Anelasticity of Metals*. Univeristy of Chicago Press, Chicago.

Zhang, Y., Gokhman, A., Wang, W., and Zhang, Z. (2018). Effects of annealing on grain-boundary character distribution and texture evolution in hot-rolled Fe-6.5 wt% Si steel. *Journal of Magnetism and Magnetic Materials*, 451:187–192.

Zhang, Z. W., Wang, W. H., Zou, Y., Baker, I., Cheng, D., and Liang, Y. F. (2015). Control of grain boundary character distribution and its effects on the deformation of Fe–6.5 wt.% Si. *Journal of Alloys and Compounds*, 639:40–44.

Ziegenhain, G., Hartmaier, A., and Urbassek, H. M. (2009). Pair vs many-body potentials: Influence on elastic and plastic behavior in nanoindentation of fcc metals. *Journal of the Mechanics and Physics of Solids*, 57:1514–1526.

Zohdi, T. I. and Wriggers, P. (2005). *An Introduction to Computational Micromechanics*, volume 2. Springer, Berlin.

Appendix A – Anisotropic fundamental solution

A.1 Barnett–Lothe in terms of Stroh's eigenvalues

The Barnett-Lothe tensor, $\mathbf{H}(\theta, \phi)$ in terms of Stroh's eigenvalues p_i , are given by

$$\mathbf{H}(\theta, \phi) = \frac{1}{|\boldsymbol{\kappa}|} \sum_{n=0}^4 q_n \hat{\Gamma}^{(n)} \quad , \quad (\text{A.1.1})$$

where q_n is defined by

$$q_n = \begin{cases} \frac{-1}{2\beta_1\beta_2\beta_3} \left[\Re \left\{ \sum_{t=0}^3 \frac{p_t^n}{(p_t - \bar{p}_{t+1})(p_t - \bar{p}_{t+2})} \right\} - \delta_{n2} \right] & \text{for } n = 0, 1, 2 \\ \frac{-1}{2\beta_1\beta_2\beta_3} \left[\Re \left\{ \sum_{t=0}^3 \frac{p_t^{n-2} \bar{p}_{t+1} \bar{p}_{t+2}}{(p_t - \bar{p}_{t+1})(p_t - \bar{p}_{t+2})} \right\} \right] & \text{for } n = 3, 4 \end{cases} \quad . \quad (\text{A.1.2})$$

The fourth-order tensor $\hat{\Gamma}^{(n)}$ is the adjoin of the matrix $\Gamma(p)$ defined as

$$\hat{\Gamma}_{ij}^{(n)} = \tilde{\Gamma}_{(i+1)(j+1)(i+2)(j+2)}^{(n)} - \tilde{\Gamma}_{(i+1)(j+2)(i+2)(j+1)}^{(n)}, \quad (i, j = 1, 2, 3) \quad , \quad (\text{A.1.3})$$

$$\Gamma(p) = \mathbf{Q} + p\mathbf{V} + p^2\boldsymbol{\kappa} \quad , \quad (\text{A.1.4})$$

where

$$\mathbf{V} = (\mathbf{R} + \mathbf{R}^T) \quad , \quad (\text{A.1.5})$$

and

$$\mathbf{Q} \equiv Q_{ik} = C_{ijks} n_j n_s, \quad \mathbf{R} \equiv R_{ik} = C_{ijks} n_j m_s \quad . \quad (\text{A.1.6})$$

The remaining term of Equation (A.1.1), $\boldsymbol{\kappa}$ is given by

$$\boldsymbol{\kappa} \equiv \kappa_{ik} = C_{ijks} m_j m_s \quad . \quad (\text{A.1.7})$$

In Equation (A.1.2), the Stroh's eigenvalues are the roots of the sextic equation obtained by the determinant $|\boldsymbol{\Gamma}(p)| = 0$, composed by three pairs of complex conjugates, written as

$$p_u = \alpha_v + \mathbf{i}\beta_v, \quad \beta_v > 0, \quad (v = 1,2,3) \quad . \quad (\text{A.1.8})$$

Finally, The tensor $\hat{\boldsymbol{\Gamma}}^{(n)}$ is expressed in a reduced form after some algebraic manipulation (SHIAH ET AL., 2008) as

$$\begin{aligned} \tilde{\Gamma}_{pqrs}^{(4)} &= \kappa_{pq} \kappa_{rs} \quad , \\ \tilde{\Gamma}_{pqrs}^{(3)} &= V_{pq} \kappa_{rs} + \kappa_{pq} V_{rs} \quad , \\ \tilde{\Gamma}_{pqrs}^{(2)} &= \kappa_{pq} Q_{rs} + \kappa_{rs} Q_{pq} + V_{pq} V_{rs} \quad , \\ \tilde{\Gamma}_{pqrs}^{(1)} &= \kappa_{pq} Q_{rs} + \kappa_{rs} Q_{pq} \quad , \\ \tilde{\Gamma}_{pqrs}^{(0)} &= Q_{pq} Q_{rs} \quad . \end{aligned} \quad (\text{A.1.9})$$

A.2 Displacement fundamental solution and its derivatives

The Barnett-Lothe tensor, $\mathbf{H}(\theta, \phi)$ can be expressed in terms of double Fourier series in the spherical coordinate system, it is given by

$$H_{uv}(\theta, \phi) = \sum_{m=-\alpha}^{\alpha} \sum_{n=-\alpha}^{\alpha} \lambda_{uv}^{(m,n)} e^{i(m\theta+n\phi)} \quad (u, v = 1, 2, 3) \quad , \quad (\text{A.2.1})$$

where, α must be large appropriately for the convergence of the series. The unknown Fourier coefficients $\lambda_{uv}^{(m,n)}$ are evaluated by

$$\lambda_{uv}^{(m,n)} = \frac{1}{4\pi^2} \int_{-\pi}^{\pi} \int_{-\pi}^{\pi} H_{uv}(\theta, \phi) e^{-i(m\theta+n\phi)} d\theta d\phi \quad . \quad (\text{A.2.2})$$

In Equation (A.2.2) using the Euler's formula, $\lambda_{uv}^{(m,n)}$ and $\lambda_{uv}^{(-m,-n)}$ are complex conjugates, thus

$$\lambda_{uv}^{(m,n)} = \bar{\lambda}_{uv}^{(-m,-n)} \quad . \quad (\text{A.2.3})$$

The Fourier coefficients $\lambda_{uv}^{(m,n)}$ can be separated into the real part $R_{uv}^{(m,n)}$ and the imaginary part $I_{uv}^{(m,n)}$ as

$$\lambda_{uv}^{(m,n)} = R_{uv}^{(m,n)} + \mathbf{i}I_{uv}^{(m,n)} \quad . \quad (\text{A.2.4})$$

Substituting Equation (A.2.3) into Equation (A.2.1) and using the Euler's formula, gives

$$H_{uv}(\theta, \phi) = \sum_{m=-\alpha}^{\alpha} \sum_{n=-\alpha}^{\alpha} h_{uv}^{(m,n)}(\theta, \phi) \quad (u, v = 1, 2, 3) \quad , \quad (\text{A.2.5})$$

where

$$h_{uv}^{(m,n)}(\theta, \phi) = R_{uv}^{(m,n)} \cos(m\theta + n\phi) - I_{uv}^{(m,n)} \sin(m\theta + n\phi) \quad . \quad (\text{A.2.6})$$

Using the condition in Equation (A.2.3), the Equation (A.2.5) can be simplified as

$$H_{uv}(\theta, \phi) = 2 \sum_{m=1}^{\alpha} \left\{ \sum_{n=1}^{\alpha} h_{uv}^{(m,n)}(\theta, \phi) + \sum_{m=-\alpha}^{-1} h_{uv}^{(m,n)}(\theta, \phi) \right\} + 2 \sum_{n=1}^{\alpha} h_{uv}^{(0,n)}(\theta, \phi) + 2 \sum_{m=1}^{\alpha} h_{uv}^{(m,0)}(\theta, \phi) + R_{uv}^{(0,0)} . \quad (\text{A.2.7})$$

Substituting Equation (A.2.6) into Equation (A.2.7) and finally into Equation (2.4), the fundamental solution U is expressed by

$$U_{uv}(r, \theta, \phi) = \frac{1}{2\pi r} \left\{ \sum_{m=1}^{\alpha} \sum_{n=1}^{\alpha} \left[\begin{array}{l} (\tilde{R}_{uv}^{(m,n)} \cos m\theta - \tilde{I}_{uv}^{(m,n)} \sin m\theta) \cos n\phi \\ -(\hat{R}_{uv}^{(m,n)} \sin m\theta - \hat{I}_{uv}^{(m,n)} \cos m\theta) \sin n\phi \end{array} \right] + \sum_{m=1}^{\alpha} \left(\begin{array}{l} R_{uv}^{(0,m)} \cos m\phi - I_{uv}^{(0,m)} \sin m\phi \\ +R_{uv}^{(m,0)} \cos m\theta - I_{uv}^{(m,0)} \sin m\theta \end{array} \right) + \frac{R_{uv}^{(0,0)}}{2} \right\} . \quad (\text{A.2.8})$$

The components $\tilde{R}_{uv}^{(m,n)}$, $\hat{R}_{uv}^{(m,n)}$, $\tilde{I}_{uv}^{(m,n)}$ and $\hat{I}_{uv}^{(m,n)}$ are

$$\begin{aligned} \tilde{R}_{uv}^{(m,n)} &= R_{uv}^{(m,n)} + R_{uv}^{(m,-n)}, & \hat{R}_{uv}^{(m,n)} &= R_{uv}^{(m,n)} - R_{uv}^{(m,-n)}, \\ \tilde{I}_{uv}^{(m,n)} &= I_{uv}^{(m,n)} + I_{uv}^{(m,-n)}, & \hat{I}_{uv}^{(m,n)} &= I_{uv}^{(m,n)} - I_{uv}^{(m,-n)} . \end{aligned} \quad (\text{A.2.9})$$

The first order derivative of the displacement fundamental solution U' is evaluated using the chain rule

$$U' \equiv U_{uv,l} = \frac{\partial U_{uv}}{\partial r} \frac{\partial r}{\partial x_l} + \frac{\partial U_{uv}}{\partial \theta} \frac{\partial \theta}{\partial x_l} + \frac{\partial U_{uv}}{\partial \phi} \frac{\partial \phi}{\partial x_l} . \quad (\text{A.2.10})$$

Applying direct partial differentiation of Equation (A.2.1) with respect to the spherical coordinates using the Equation (A.2.10), gives

$$U_{uv,l}(r,\theta,\phi) = \frac{1}{4\pi r^2} \left\{ \begin{array}{l} \sum_{m=-\alpha}^{\alpha} \sum_{n=-\alpha}^{\alpha} \lambda_{uv}^{(m,n)} e^{\mathbf{i}(m\theta+n\phi)} \begin{bmatrix} -\cos\theta(\sin\phi - \mathbf{i}n\cos\phi) \\ -\mathbf{i}m\sin\theta/\sin\phi \end{bmatrix} \\ \sum_{m=-\alpha}^{\alpha} \sum_{n=-\alpha}^{\alpha} \lambda_{uv}^{(m,n)} e^{\mathbf{i}(m\theta+n\phi)} \begin{bmatrix} -\sin\theta(\sin\phi - \mathbf{i}n\cos\phi) \\ +\mathbf{i}m\cos\theta/\sin\phi \end{bmatrix} \\ \sum_{m=-\alpha}^{\alpha} \sum_{n=-\alpha}^{\alpha} \lambda_{uv}^{(m,n)} e^{\mathbf{i}(m\theta+n\phi)} [-(\cos\phi + \mathbf{i}n\sin\phi)] \end{array} \right\}. \quad (\text{A.2.11})$$

Following a similar procedure used to obtain the Equation (A.2.8), the expression for the derivative of the displacement fundamental solution is

$$U_{uv,l} = \frac{1}{2\pi r^2} \left\{ \begin{array}{l} -\omega_l(\theta,\phi) \left[\begin{array}{l} \sum_{m=1}^{\alpha} \sum_{n=1}^{\alpha} \left(\widehat{\Gamma}_{uv}^{(m,n)}(\theta) \cos n\phi - \widetilde{\Gamma}_{uv}^{(m,n)}(\theta) \sin n\phi \right) \\ \sum_{m=1}^{\alpha} \left(\widehat{\gamma}_{uv}^{(m,n)}(\theta) + \widetilde{\gamma}_{uv}^{(m,n)}(\phi) \right) + \frac{R_{uv}^{(0,0)}}{2} \end{array} \right] \\ -\omega'_l(\theta,\phi) \left[\begin{array}{l} \sum_{m=1}^{\alpha} \sum_{n=1}^{\alpha} m \left(\widetilde{\Gamma}_{uv}^{(m,n)}(\theta) \cos n\phi - \widehat{\Gamma}_{uv}^{(m,n)}(\theta) \sin n\phi \right) \\ \sum_{m=1}^{\alpha} m \widetilde{\gamma}_{uv}^m(\theta) \end{array} \right] \\ -\omega''_l(\theta,\phi) \left[\begin{array}{l} \sum_{m=1}^{\alpha} \sum_{n=1}^{\alpha} n \left(\widehat{\Gamma}_{uv}^{(m,n)}(\theta) \sin n\phi - \widetilde{\Gamma}_{uv}^{(m,n)}(\theta) \cos n\phi \right) \\ \sum_{m=1}^{\alpha} m \widehat{\gamma}_{uv}^m(\phi) \end{array} \right] \end{array} \right\}, \quad (\text{A.2.12})$$

where $\omega_l(\theta,\phi)$, $\omega'_l(\theta,\phi)$ and $\omega''_l(\theta,\phi)$ represent the following spatial differentiations

$$\omega_l(\theta,\phi) = r \frac{\partial r}{\partial x_l} = \begin{cases} \sin\phi \cos\theta, & (\text{for } l = 1) \\ \sin\phi \sin\theta, & (\text{for } l = 2) \\ \cos\phi, & (\text{for } l = 3) \end{cases}, \quad (\text{A.2.13})$$

$$\omega'_i(\theta, \phi) = r \frac{\partial \theta}{\partial x_l} = \begin{cases} -\sin \theta / \sin \phi, & (\text{for } l = 1) \\ \cos \theta / \sin \phi, & (\text{for } l = 2) \\ 0, & (\text{for } l = 3) \end{cases}, \quad (\text{A.2.14})$$

$$\omega''_i(\theta, \phi) = r \frac{\partial \phi}{\partial x_l} = \begin{cases} \cos \phi \cos \theta, & (\text{for } l = 1) \\ \cos \phi \sin \theta, & (\text{for } l = 2) \\ -\sin \phi, & (\text{for } l = 3) \end{cases}, \quad (\text{A.2.15})$$

and

$$\begin{aligned} \widehat{\Gamma}_{uv}^{(m,n)}(\theta) &= \widetilde{R}_{uv}^{(m,n)} \cos m\theta - \widetilde{I}_{uv}^{(m,n)} \sin m\theta, \\ \widetilde{\Gamma}_{uv}^{(m,n)}(\theta) &= \widehat{R}_{uv}^{(m,n)} \sin m\theta + \widehat{I}_{uv}^{(m,n)} \cos m\theta, \\ \widetilde{\Gamma}_{uv}^{(m,n)}(\theta) &= \widetilde{R}_{uv}^{(m,n)} \sin m\theta + \widetilde{I}_{uv}^{(m,n)} \cos m\theta, \\ \widehat{\Gamma}_{uv}^{(m,n)}(\theta) &= \widehat{R}_{uv}^{(m,n)} \cos m\theta - \widehat{I}_{uv}^{(m,n)} \sin m\theta, \\ \widehat{\gamma}_{uv}^m(\theta) &= R_{uv}^{(m,0)} \cos m\theta - I_{uv}^{(m,0)} \sin m\theta, \\ \widetilde{\gamma}_{uv}^m(\phi) &= R_{uv}^{(0,m)} \cos m\phi - I_{uv}^{(0,m)} \sin m\phi, \\ \widetilde{\gamma}_{uv}^m(\theta) &= R_{uv}^{(m,0)} \sin m\theta + I_{uv}^{(m,0)} \cos m\theta, \\ \widehat{\gamma}_{uv}^{(m,n)}(\theta) &= R_{uv}^{(0,m)} \sin m\phi + I_{uv}^{(0,m)} \cos m\phi. \end{aligned} \quad (\text{A.2.16})$$

A numerical singularity occurs in the formulation of this fundamental solution in the evaluation of its derivative \mathbf{U}' . In the special case when the field and source point are both over the x_3 -axis at $\phi = 0$ or $\phi = \pi$ for $l = 1$ and $l = 2$. This condition occurs because the spherical angle θ becomes ill-conditioned at these locations. Tan et al. (2013) suggest a scheme to remove this singularity, imposing a small perturbation for ϕ , such as $\phi = 10^{-6}$ and $\theta = 0$ for $l = 1$. In case of $l = 2$, it is selected $\theta = \pi/2$.

Appendix B – Triangular boundary elements

B.1 Shape functions and its derivatives

The shape functions of the three-node discontinuous elements are evaluated numerically following the procedure shown in (KANE, 1994), where these shape functions are obtained from the known shape functions of the continuous three-node triangular element Figure B.1.1

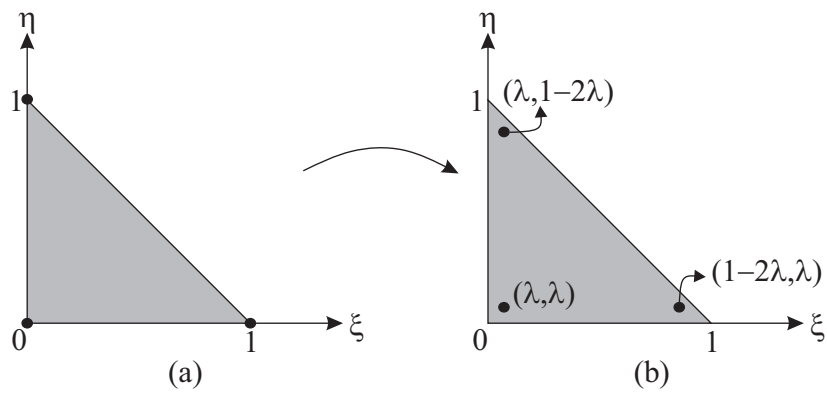


Figure B.1.1: Linear three-node elements: (a) continuous and (b) discontinuous.

The known shape functions of the continuous three-node triangular element expressed by

$$\begin{aligned} N^{(1)} &= \xi \quad , \\ N^{(2)} &= \eta \quad , \\ N^{(3)} &= 1 - \xi - \eta \quad . \end{aligned} \tag{B.1.1}$$

The interpolated field X expressed in terms of the known node values $X^{(k)}$ are

$$X(\xi, \eta) = \sum_{k=1}^3 N^{(k)}(\xi, \eta) X^{(k)} \quad . \tag{B.1.2}$$

Now, assuming w_j as the interpolated values of the new discontinuous element and forcing

the Equation (B.1.2)

$$w_j = \sum_{k=1}^3 N^{(k)}(\xi, \eta) X^{(k)} \quad , \quad (\text{B.1.3})$$

expanding the matrix form

$$\begin{Bmatrix} w_1 \\ w_2 \\ w_3 \end{Bmatrix} = \begin{bmatrix} N^{(1)}(1-2\lambda, \lambda) & N^{(2)}(1-2\lambda, \lambda) & N^{(3)}(1-2\lambda, \lambda) \\ N^{(1)}(\lambda, 1-2\lambda) & N^{(2)}(\lambda, 1-2\lambda) & N^{(3)}(\lambda, 1-2\lambda) \\ N^{(1)}(\lambda, \lambda) & N^{(2)}(\lambda, \lambda) & N^{(3)}(\lambda, \lambda) \end{bmatrix} = \begin{Bmatrix} X^{(1)} \\ X^{(2)} \\ X^{(3)} \end{Bmatrix} \quad , \quad (\text{B.1.4})$$

or

$$\{w\} = [L]\{X\} \quad . \quad (\text{B.1.5})$$

The Equation (3.12) can be solved for the values X as

$$\{X\} = [L]^{-1}\{w\} = [G]\{w\} \quad . \quad (\text{B.1.6})$$

Substituting Equation (B.1.6) into Equation (B.1.2) the formula for the matrix interpolation functions for the discontinuous element is obtained

$$X(\xi, \eta) = \sum_{k=1}^3 N^{(k)}(\xi, \eta) X^{(k)} = [N]\{X\} = [N][G]\{w\} = [H]\{w\} \quad , \quad (\text{B.1.7})$$

where $[H] = [h^{(1)} h^{(2)} h^{(3)}]$. The derivative of the shape functions respect to the intrinsic coordinates ξ and η need to be expressed as

$$\begin{aligned}
\frac{\partial x_j(\xi, \eta)}{\partial \xi} &= \sum_{k=1}^3 \frac{\partial N^{(k)}(\xi, \eta)}{\partial \xi} x_j^{(k)} = [N]_{,\xi} [G] \{w_j\} = [H]_{,\xi} \{w_j\} \quad , \\
\frac{\partial x_j(\xi, \eta)}{\partial \eta} &= \sum_{k=1}^3 \frac{\partial N^{(k)}(\xi, \eta)}{\partial \eta} x_j^{(k)} = [N]_{,\eta} [G] \{w_j\} = [H]_{,\eta} \{w_j\} \quad .
\end{aligned}
\tag{B.1.8}$$

The Jacobian and the normal vectors are given by Equation (B.1.9).

$$J = 0.5 (J_1^2 + J_2^2 + J_3^2)^{0.5} = 0.5 (J_k J_k)^{0.5} \quad , \tag{B.1.9}$$

where

$$\begin{aligned}
J_1 &= \frac{\partial x_2}{\partial \xi} \frac{\partial x_3}{\partial \eta} - \frac{\partial x_3}{\partial \xi} \frac{\partial x_2}{\partial \eta} \quad , \\
J_2 &= \frac{\partial x_3}{\partial \xi} \frac{\partial x_1}{\partial \eta} - \frac{\partial x_1}{\partial \xi} \frac{\partial x_3}{\partial \eta} \quad , \\
J_3 &= \frac{\partial x_1}{\partial \xi} \frac{\partial x_2}{\partial \eta} - \frac{\partial x_2}{\partial \xi} \frac{\partial x_1}{\partial \eta} \quad .
\end{aligned}
\tag{B.1.10}$$

The terms x_k represents the coordinates of the actual element, and the normal vector is expressed as

$$n_k = J_k J^{-1} \quad . \tag{B.1.11}$$

From the Equation (B.1.2) to Equation (B.1.8) the terms w_j contain the three coordinates of the nodes of the discontinuous elements, the matrix $[G]$ is the same in Equations (B.1.7) and (B.1.8). Finally the matrix $[L]$ can be evaluated numerically.

Appendix C – Atomistic modeling

C.1 EAM potential parameters

In this appendix, all the parameters of the EAM (MENDELEV ET AL., 2003) potential used in this work are presented in Table C.1.1. The parameters a_k and A_k are expressed in $\text{eV}/\text{\AA}^k$, when the r_k and R_k coefficients are given in \AA units.

Parameter	Fe
$a_1(r_1)$	195.92322853994 (2.1)
$a_2(r_2)$	17.516698453315 (2.2)
$a_3(r_3)$	1.4926525164290 (2.3)
$a_4(r_4)$	6.4129476125197 (2.4)
$a_5(r_5)$	-6.8157461860553 (2.5)
$a_6(r_6)$	9.6582581963600 (2.6)
$a_7(r_7)$	-5.3419002764419 (2.7)
$a_8(r_8)$	1.7996558048346 (2.8)
$a_9(r_9)$	-1.4788966636288 (3.0)
$a_{10}(r_{10})$	1.8530435283665 (3.3)
$a_{11}(r_{11})$	-0.64164344859316 (3.7)
$a_{12}(r_{12})$	0.24463630025168 (4.2)
$a_{13}(r_{13})$	-0.057721650527383 (4.7)
$a_{14}(r_{14})$	0.023358616514826 (5.3)
$a_{15}(r_{15})$	-0.0097064921265079 (6.0)
$A_1(R_1)$	11.686859407970 (2.4)
$A_2(R_2)$	-0.014710740098830 (3.2)
$A_3(R_3)$	0.47193527075943 (4.2)

Table C.1.1: Parameters for the EAM potential energy functions.

The remaining coefficients of the EAM potential are given in Table C.1.2. Here the B_k terms are in \AA^{-k} units, while the parameter a^* is given in \AA units.

Parameter	Fe
B_0	6.4265260576348
B_1	1.7900488524286
B_2	-4.5108316729807
B_3	1.0866199373306
a^*	-0.00035387096579929

Table C.1.2: The remaining coefficients of the EAM potential.

C.2 Thermal process and energy minimization

In this section, it is presented the LAMMPS script to evaluate the GB energy. The value of the following variables `dt`, `temp_i`, `overlap`, `datfile`, `Potential`, `Struc` and `E_c` must be defined according to the material used in the simulations. In this script, the final minimized structure is exported in a `restart.struct` file.

```
# LAMMPS script File to calculate the Grain Boundary energy of Fe
```

```
# ----- Initialize Simulation -----
units metal
dimension 3
boundary p p p
atom_style atomic
atom_modify map array

# ----- General Variables -----
variable dt      equal dt
variable tstart equal 800
variable tseed   equal temp_i
variable tfinal  equal 10
variable tdamp   equal 0.2
variable pdamp   equal 2
variable seed    equal 1234546
variable overl   equal overlap

# ----- Atomistic Structure -----
read_data datfile
```

```

variable xlen equal lx
variable ylen equal ly
variable zlen equal lz
variable zlen2 equal ${zlen}/2

print "lx: ${xlen}"
print "ly: ${ylen}"
print "lz: ${zlen}"

region upper block 0.000000 ${xlen} 0.000000 ${ylen} &
                    ${zlen2} ${zlen} units box
region lower block 0.000000 ${xlen} 0.000000 ${ylen} &
                    0.000000 ${zlen2} units box

group upper type 1
group lower type 2

# ----- Interatomic Potential -----
pair_style eam/fs
pair_coeff * * Potential
neighbor 2.0 bin
neigh_modify delay 10 check yes page 100000000 one 1000000

# ----- Overlapping Atoms -----
displace_atoms upper move 0 0 0 units lattice
delete_atoms overlap ${overl} lower upper

# ----- Initial State -----
compute csym all centro/atom Struc
compute eng all pe/atom
compute eatoms all reduce sum c_eng
compute T all temp/com

# ----- Initial Temperature -----
reset_timestep 0
timestep $dt
thermo 100
thermo_style custom step temp pe lx ly lz press pxx pyy pzz c_eatoms

velocity all create ${tseed} ${seed} dist gaussian
fix      NVE all nve
fix      4 all temp/rescale 1 ${tseed} ${tseed} 0.1 1.0

```

```

run      1000
unfix   NVE
unfix    4

# ----- Thermal Process -----
reset_timestep 0
# ----- Now Temperature Ramp to desired value, Steady pressure
fix     1 all npt temp ${tseed} $tstart ${tdamp} x 0.0 0.0 ${pdamp} &
      y 0.0 0.0 ${pdamp} z 0.0 0.0 ${pdamp}
run     10000
unfix   1
# ----- Then steady temperature, steady pressure
fix     1 all npt temp ${tstart} ${tstart} ${tdamp} x 0.0 0.0 ${pdamp} &
      y 0.0 0.0 ${pdamp} z 0.0 0.0 ${pdamp}
run     10000
unfix   1
# ----- Then temperature ramp to 10, steady pressure
fix     1 all npt temp ${tstart} ${tfinal} ${tdamp} x 0.0 0.0 ${pdamp} &
      y 0.0 0.0 ${pdamp} z 0.0 0.0 ${pdamp}
run     10000
unfix   1
# ----- Then steady temperature, steady pressure
fix     1 all npt temp ${tfinal} ${tfinal} ${tdamp} x 0.0 0.0 ${pdamp} &
      y 0.0 0.0 ${pdamp} z 0.0 0.0 ${pdamp}
run     10000
unfix   1

# ----- Run the firts Minimization -----
min_style cg
minimize 1.0e-25 1.0e-25 100000 1000000

# ----- Run the second Minimization relaxing -----
reset_timestep 0
thermo 10
thermo_style custom step temp pe lx ly lz press pxx pyy pzz c_eatoms
fix 4 all box/relax z 0 vmax 0.001
min_style cg
minimize 1e-25 1e-25 100000 1000000

# ----- Calculate GB Energy -----
variable minimumenergy equal E_c

```

```

variable esum equal "v_minimumenergy * count(all)"
variable xseng equal "c_eatoms - (v_minimumenergy * count(all))"
variable gbarea equal "lx * ly * 2"
variable gbe equal "(c_eatoms - (v_minimumenergy * count(all)))/v_gbarea"
variable gbemJm2 equal "${gbe}*16021.7733"
variable gbernd equal round("${gbemJm2}")
print "GB energy is ${gbemJm2} mJ/m^2"

# ----- Run last minimization and write restart -----
reset_timestep 0
minimize 1e-25 1e-25 100000 1000000

print "All done"

```

C.3 GB structures for energy validation

A set of STGBs and STwGBs structures was built using the *GBstudio* software.

Tilt GBs $\langle 110 \rangle$			Twist GBs $\langle 111 \rangle$		
θ angle ($^\circ$)	Σ value	GB plane (\hat{n})	φ angle ($^\circ$)	Σ value	(\hat{c})
0.0	1	$\{0\ 0\ 1\}$	0.0	1	$\{1\ 1\ \bar{1}\}$
11.53	99	$\{1\ \bar{1}\ 14\}$	10.4	91	$\{10\ \bar{1}\ \bar{9}\}$
13.44	73	$\{1\ \bar{1}\ 12\}$	11.6	73	$\{9\ \bar{1}\ \bar{8}\}$
16.09	51	$\{1\ \bar{1}\ 10\}$	13.7	57	$\{8\ \bar{1}\ \bar{7}\}$
17.9	83	$\{1\ \bar{1}\ 9\}$	15.17	43	$\{7\ \bar{1}\ \bar{6}\}$
20.04	33	$\{1\ \bar{1}\ 8\}$	17.89	31	$\{6\ \bar{1}\ \bar{5}\}$
22.8	51	$\{1\ \bar{1}\ 7\}$	21.78	21	$\{5\ \bar{1}\ \bar{4}\}$
26.52	19	$\{1\ \bar{1}\ 6\}$	24.43	67	$\{9\ \bar{2}\ \bar{7}\}$
31.6	27	$\{1\ \bar{1}\ 5\}$	27.79	13	$\{4\ \bar{1}\ \bar{3}\}$
34.9	89	$\{2\ \bar{2}\ 9\}$	30.59	97	$\{11\ \bar{3}\ \bar{8}\}$
38.94	9	$\{1\ \bar{1}\ 4\}$	32.20	39	$\{7\ \bar{2}\ \bar{5}\}$
44.0	57	$\{2\ \bar{2}\ 7\}$	33.99	79	$\{10\ \bar{3}\ \bar{7}\}$
45.97	59	$\{3\ \bar{3}\ 10\}$	38.21	7	$\{3\ \bar{1}\ \bar{2}\}$
50.5	11	$\{1\ \bar{1}\ 3\}$	42.10	93	$\{11\ \bar{4}\ \bar{7}\}$

Table C.3.1: Grain boundaries: symmetric $\langle 110 \rangle$ tilt and $\langle 111 \rangle$ twist.

Tilt GBs $\langle 110 \rangle$			Twist GBs $\langle 111 \rangle$		
θ angle ($^\circ$)	Σ value	GB plane (\hat{n})	φ angle ($^\circ$)	Σ value	(\hat{c})
55.87	41	$\{3 \bar{3} 8\}$	43.57	49	$\{8 \bar{3} \bar{5}\}$
58.99	33	$\{2 \bar{2} 5\}$	46.82	19	$\{5 \bar{2} \bar{3}\}$
61.01	97	$\{5 \bar{5} 12\}$	50.56	37	$\{7 \bar{3} \bar{4}\}$
70.52	3	$\{1 \bar{1} 2\}$	52.65	61	$\{9 \bar{4} \bar{5}\}$
77.9	81	$\{7 \bar{4} \bar{4}\}$	53.99	91	$\{11 \bar{5} \bar{6}\}$
80.6	43	$\{5 \bar{3} \bar{3}\}$	60	3	$\{2 \bar{1} \bar{1}\}$
82.94	57	$\{5 \bar{5} 8\}$			
86.6	17	$\{3 \bar{2} \bar{2}\}$			
89.42	99	$\{7 \bar{7} 10\}$			
90.6	99	$\{7 5 5\}$			
93.37	17	$\{3 \bar{3} 4\}$			
97.1	57	$\{5 4 4\}$			
99.36	43	$\{5 \bar{5} 6\}$			
102.1	81	$\{7 \bar{7} 8\}$			
109.5	3	$\{1 1 1\}$			
117.5	67	$\{7 \bar{7} 6\}$			
121	33	$\{5 \bar{5} 4\}$			
129.5	11	$\{3 \bar{3} 2\}$			
134	59	$\{5 \bar{5} \bar{3}\}$			
135.9	57	$\{7 \bar{7} 4\}$			
141.1	9	$\{2 \bar{2} \bar{1}\}$			
145.1	89	$\{9 \bar{9} 4\}$			
148.4	27	$\{5 \bar{5} 2\}$			
153.5	19	$\{3 \bar{3} \bar{1}\}$			
157.1	51	$\{7 \bar{7} 2\}$			
162.1	83	$\{9 \bar{9} 2\}$			
166.6	73	$\{6 \bar{6} \bar{1}\}$			
168.5	99	$\{7 \bar{7} \bar{1}\}$			
180	1	$\{0 0 1\}$			

Table C.3.1: Grain boundaries, symmetric $\langle 110 \rangle$ tilt and $\langle 111 \rangle$ twist. (Continuation).

C.4 GB structures for failure analysis

A set of STGBs, ATGB, STwGB and ATwGBs structures was built using the *GBstudio* software. In this case, $\hat{\mathbf{n}}_A$ and $\hat{\mathbf{n}}_B$ represent the GB plane of grains *A* and *B* respectively.

Σ value	$(\hat{\mathbf{n}}_A)/(\hat{\mathbf{n}}_B)$	Σ value	$(\hat{\mathbf{n}}_A)/(\hat{\mathbf{n}}_B)$
3	(1 1 0)/(4 1 1)	17	(2 2 1)/(2 2 1)
3	(1 $\bar{1}$ 1)/($\bar{1}$ $\bar{1}$ 5)	19	(4 $\bar{4}$ 5)/(2 $\bar{2}$ 7)
5	(5 3 1)/(5 3 $\bar{1}$)	19	(7 $\bar{7}$ 4)/(5 $\bar{5}$ 8)
5	(5 $\bar{4}$ 2)/(5 $\bar{2}$ 4)	19	(7 $\bar{8}$ 1)/(1 $\bar{8}$ 7)
5	(5 6 2)/(5 6 $\bar{2}$)	19	(9 6 4)/(9 4 6)
5	(5 $\bar{6}$ 3)/(5 $\bar{3}$ 6)	19	(1 1 1)/(1 1 1)
5	(1 1 1)/(5 7 1)	21	(5 $\bar{4}$ $\bar{1}$)/(4 $\bar{5}$ 1)
7	(4 $\bar{5}$ 1)/(1 $\bar{5}$ 4)	21	(2 $\bar{3}$ 1)/(1 $\bar{3}$ 2)
7	(5 6 3)/(6 5 3)	19	(1 1 1)/(1 1 1)
9	(1 $\bar{1}$ 2)/(5 $\bar{5}$ $\bar{2}$)	21	(1 $\bar{1}$ 0)/(5 $\bar{8}$ 3)
9	(4 5 7)/(1 8 5)	21	(4 5 8)/(4 8 5)
9	(5 $\bar{5}$ $\bar{7}$)/(7 $\bar{7}$ $\bar{1}$)	21	(2 $\bar{1}$ $\bar{3}$)/(2 $\bar{3}$ $\bar{1}$)
9	(1 $\bar{1}$ 0)/(7 $\bar{7}$ 8)	21	(3 $\bar{5}$ $\bar{1}$)/(1 $\bar{5}$ 3)
11	(5 $\bar{5}$ $\bar{7}$)/(7 $\bar{7}$ 1)	25	(5 6 8)/(5 8 6)
13	(5 6 2)/(6 5 2)	25	(5 1 7)/(1 5 7)
13	(5 $\bar{7}$ 2)/(2 $\bar{7}$ 5)	25	(5 4 3)/(4 5 3)
13	(1 1 1)/(1 1 1)	25	(10 $\bar{7}$ 1)/(1 $\bar{1}$ 2)
13	(2 $\bar{2}$ 1)/(1 $\bar{2}$ 2)	27	(2 $\bar{2}$ 1)/(4 $\bar{4}$ 7)
13	(4 $\bar{3}$ $\bar{1}$)/(3 $\bar{4}$ 1)	27	(1 $\bar{2}$ $\bar{2}$)/(4 $\bar{8}$ $\bar{1}$)
15	(1 1 $\bar{1}$)/(7 1 $\bar{5}$)	27	(1 $\bar{1}$ 0)/(8 $\bar{7}$ 7)
15	(2 1 1)/(3 4 0)	27	(0 1 $\bar{1}$)/(1 1 $\bar{4}$)
15	(5 $\bar{4}$ $\bar{2}$)/(8 $\bar{6}$ 5)	29	(4 $\bar{3}$ $\bar{2}$)/(3 $\bar{4}$ 2)
15	(2 2 1)/(5 5 2)	29	(2 2 1)/(2 2 1)
17	(3 $\bar{2}$ $\bar{2}$)/(2 $\bar{3}$ 2)	29	(0 2 $\bar{3}$)/(2 0 $\bar{3}$)
17	(4 3 3)/(3 4 3)	31	(1 1 1)/(1 1 1)

Table C.4.1: Set of GB structures for failure analysis.

Σ value	$(\hat{n}_A)/(\hat{n}_B)$	Σ value	$(\hat{n}_A)/(\hat{n}_B)$
31	(2 1 1)/(2 1 1)	51	(2 $\bar{2}$ $\bar{3}$)/(8 $\bar{8}$ $\bar{5}$)
33	(1 $\bar{1}$ 3)/(5 $\bar{5}$ $\bar{7}$)	51	(4 $\bar{1}$ 1)/(1 0 1)
33	(2 1 2)/(7 6 6)	53	(1 $\bar{6}$ 4)/($\bar{1}$ $\bar{4}$ 6)
35	(1 2 3)/(1 3 2)	55	(1 0 1)/(4 3 5)
35	(9 $\bar{3}$ $\bar{8}$)/(9 $\bar{8}$ $\bar{3}$)	55	(5 5 7)/(5 7 5)
35	(4 5 7)/(4 7 5)	55	(8 $\bar{1}$ $\bar{5}$)/(8 $\bar{5}$ $\bar{1}$)
35	(7 5 6)/(7 6 5)	55	(6 7 0)/(7 6 0)
35	(2 1 1)/(2 1 1)	57	(1 1 0)/(1 1 0)
35	(4 $\bar{5}$ $\bar{7}$)/(5 $\bar{7}$ $\bar{1}$)	59	(1 1 2)/(1 2 1)
35	(6 $\bar{5}$ $\bar{3}$)/(5 $\bar{6}$ 3)	61	(8 $\bar{7}$ $\bar{3}$)/(7 $\bar{8}$ 3)
37	(2 $\bar{2}$ $\bar{1}$)/(2 $\bar{2}$ 1)	61	(6 $\bar{4}$ $\bar{3}$)/(4 $\bar{6}$ 3)
37	(1 1 1)/(1 1 1)	61	(1 1 1)/(1 1 1)
39	(7 $\bar{5}$ $\bar{2}$)/(5 $\bar{7}$ 2)	63	(1 1 2)/(2 5 5)
39	(3 $\bar{4}$ 1)/(1 $\bar{4}$ 3)	63	(5 $\bar{7}$ 4)/(4 $\bar{5}$ 7)
39	(1 1 1)/(1 1 1)	63	(5 4 7)/(5 7 4)
39	(2 $\bar{3}$ 0)/(2 $\bar{7}$ 8)	63	(7 5 $\bar{4}$)/(8 1 $\bar{5}$)
41	(2 $\bar{2}$ $\bar{1}$)/(2 $\bar{2}$ 1)	63	(4 2 5)/(2 5 4)
43	(1 1 1)/(1 1 1)	65	(6 $\bar{5}$ $\bar{2}$)/(5 $\bar{6}$ 2)
43	(6 5 5)/(5 6 5)	65	(2 1 1)/(2 2 1)
45	(7 4 5)/(7 5 4)	67	(9 $\bar{7}$ 2)/(7 $\bar{9}$ 2)
45	(2 $\bar{1}$ 1)/(5 $\bar{2}$ 5)	67	(1 1 1)/(1 1 1)
45	(5 $\bar{7}$ 4)/(1 $\bar{5}$ 8)	67	(7 6 7)/(7 7 6)
45	(1 $\bar{2}$ $\bar{1}$)/(2 $\bar{7}$ 1)	75	(1 $\bar{1}$ 2)/(2 $\bar{1}$ $\bar{7}$)
45	(7 5 6)/(5 7 6)	75	(1 2 $\bar{1}$)/(5 2 $\bar{5}$)
49	(5 $\bar{3}$ $\bar{8}$)/(5 $\bar{8}$ $\bar{3}$)	81	(8 $\bar{4}$ $\bar{1}$)/(7 $\bar{4}$ 4)
49	(3 5 8)/(3 8 5)		

Table C.4.1: Set of GB structures for failure analysis. (Continuation).

C.5 GB failure scripts

In this section, it is presented the LAMMPS scripts to evaluate the normal and shear failure tests. The value of the following variables `dt`, `temp`, `erate`, `Potential` and `struct` must be defined according to the material used in the simulations. The GB structure is read from a database and new files must be generated, containing the stress and strain values at every time step. Furthermore, a `.dump` file for visualization is also exported.

o *Tensile failure:*

```
# =====
# LAMMPS script for tensile failure on a Grain Boundarie of Fe

# ----- General Variables -----
variable dt      equal dt      # timestep in ps
variable erate   equal erate   # deform erate each unit time
variable tdump   equal 5000     # dump each tdump steps
variable tprint  equal 1000     # print each tprint steps
variable thermo  equal 100      # compute and print thermodynamic info
variable tinitial equal 10      # final temperature
variable tfinal  equal temp    # final temperature
variable tdamp   equal 0.2
variable pdamp   equal 2
variable seed    equal round(random(0,999999,$RANDOM))
variable c       equal 0.30 # crack size l=c*Ly

# ----- Structure -----

read_restart ../restart.struct # read structure from a directory

variable xlen equal lx
variable ylen equal ly
variable zlen equal lz
variable zlen2 equal ${zlen}/2

print "lx: ${xlen}"
print "ly: ${ylen}"
print "lz: ${zlen}"
```

```

# Crack
region      crack block 0.000000 $xlen $yleni $ylenf $zleni $zlenf
group       crack region crack
delete_atoms group crack

# Upper and lower crystals
region up   block 0.000000 ${xlen} 0.000000 ${ylen} &
           ${zlen2} ${zlen} units box
region low  block 0.000000 ${xlen} 0.000000 ${ylen} &
           0.000000 ${zlen2} units box

group up   type 1
group low  type 2

# ----- Interatomic Potential -----
pair_style eam/fs
pair_coeff * * Potential
neighbor 2.0 bin
neigh_modify delay 10 check yes page 100000000 one 1000000

# ----- Define Settings -----
compute T      all temp/com
compute stress all stress/atom NULL virial

reset_timestep 0
timestep $dt

variable pxx equal pxx
variable pyy equal pyy
variable pzz equal pzz
variable xcm equal xcm(all,x)
variable ycm equal xcm(all,y)
variable zcm equal xcm(all,z)

thermo          $thermo
thermo_style    custom step temp pe ke etotal lx ly lz press pxx pyy pzz
thermo_modify   lost warn norm yes

# ----- To allow the sample to contract during deformation -----
fix    nph      all nph x 0.0 0.0 ${pdamp} y 0.0 0.0 ${pdamp} &

```

```
z 0.0 0.0 ${pdamp} fixedpoint ${xcm} ${ycm} ${zcm}
fix langevin all langevin ${tinitial} ${tfinal} ${tdamp} &
    ${seed} zero yes
run 10000

unfix npb

reset_timestep 0

variable step equal step
variable strain equal v_step*${erate}*${dt}

fix npb all npb x 0.0 0.0 ${pdamp} y 0.0 0.0 ${pdamp} &
    fixedpoint ${xcm} ${ycm} $zcm

# ----- Apply loading -----

fix DEFORM_FIX all deform 1 z erate ${erate}

run 370000 # total strain of 37%
print "All done"
# =====
```

o *Shear failure:*

```
# =====
# LAMMPS script for shear failure on a Grain Boundarie of Fe

# ----- General Variables -----
variable dt          equal dt      # timestep in ps
variable erate       equal erate    # deform erate each unit time
variable tdump       equal 5000     # dump each tdump steps
variable tprint      equal 1000     # print each tprint steps
variable thermo      equal 100      # compute and print thermodynamic info
variable tinitial    equal 10       # final temperature
variable tfinal      equal temp    # final temperature
variable tdamp       equal 0.2
variable pdamp       equal 2
variable seed        equal round(random(0,999999,$RANDOM))
variable c           equal 0.30 # crack size l = c*Ly

# ----- Structure -----

read_restart ../restart.struct # read structure from a directory

variable xlen equal lx
variable ylen equal ly
variable zlen equal lz
variable zlen2 equal ${zlen}/2
variable zlo equal zlo
variable zhi equal zhi

print "lx: ${xlen}"
print "ly: ${ylen}"
print "lz: ${zlen}"

# Crack
region          crack block 0.000000 $xlen $yleni $ylenf $zleni $zlenf
group          crack region crack
delete_atoms group crack

# Upper and lower crystals
region up block 0.000000 ${xlen} 0.000000 ${ylen} &
```

```

                                ${zlen2} ${zlen} units box
region low block 0.000000 ${xlen} 0.000000 ${ylen} &
                                0.000000 ${zlen2} units box

group up  type 1
group low type 2

# ----- Interatomic Potential -----
pair_style eam/fs
pair_coeff * * Potential
neighbor 2.0 bin
neigh_modify delay 10 check yes page 100000000 one 1000000

# ----- Define Settings -----
compute temp3d all temp/com
compute temp2d all temp/partial 1 0 1

reset_timestep 0
timestep $dt

variable pxx equal pxx
variable pyy equal pyy
variable pzz equal pzz
variable xcm equal xcm(all,x)
variable ycm equal xcm(all,y)
variable zcm equal xcm(all,z)

thermo          $thermo
thermo_style    custom step temp pe ke etotal lx ly lz press pxx pyy pzz
thermo_modify   lost warn norm yes

# ----- To allow the sample to contract during deformation -----

fix  npb      all npb x 0.0 0.0 ${pdamp} y 0.0 0.0 ${pdamp} &
                                z 0.0 0.0 ${pdamp} fixedpoint ${xcm} ${ycm} ${zcm}
fix  langevin all langevin ${tinitial} ${tfinal} ${tdamp} &
                                ${seed} zero yes
fix_modify langevin temp temp3d
run 10000
unfix langevin
unfix npb

```

```

reset_timestep      0

variable step      equal step
variable vel       equal $ylen*${erate}
variable strain    equal v_step*${vel}*${dt}/${ylen}
variable trun     equal 0.5*${ylen}/(${vel}*${dt}) # total strain of 50%

fix nph all nph x 0.0 0.0 ${pdamp} y 0.0 0.0 ${pdamp} &
                                fixedpoint ${xcm} ${ycm} $zcm

# ----- Apply loading -----

velocity all ramp vy -${vel} ${vel} z ${zlo} ${zhi} sum yes units box

fix          langevin all langevin ${tfinal} ${tfinal} ${tdamp} &
                                ${seed} zero yes
fix_modify   langevin temp temp2d
thermo_modify temp temp2d

run ${trun}
print "All done"
# =====

```